Modeling soot formation in turbulent flames using a virtual chemistry approach

Hernando Maldonado Colman

université
PARIS-SACLAY

Modeling soot formation in turbulent flames using a virtual chemistry approach

Thèse de doctorat de l'Université Paris-Saclay

École doctorale n° 579, Sciences mécaniques et énergétiques, matériaux et géosciences (SMEMAG)
Spécialité de doctorat: Combustion
Unité de recherche: Université Paris-Saclay, CNRS, CentraleSupélec, Laboratoire EM2C, 91190, Gif-sur-Yvette, France
Référent: CentraleSupélec

Thèse présentée et soutenue à Gif-sur-Yvette, le 27 mai 2021, par

Hernando MALDONADO COLMAN

Composition du jury:

Guillaume Legros Professeur, Université d'Orléans	Rapporteur & Président
Christian Hasse Professeur, TU Darmstadt	Rapporteur & Examinateur
Olivier Colin Docteur, IFP Energies nouvelles	Examinateur
Daniel Haworth Professeur, Pennsylvania State University	Examinateur
Eléonore Riber Docteur, CERFACS	Examinatrice
Benoît Fiorina Professeur, CentraleSupélec, Université Paris-Saclay	Directeur de thèse
Nasser Darabiha Professeur émérite, CentraleSupélec, Université Paris-Saclay	Co-encadrant
Alberto Cuoci Professeur, Politecnico di Milano	Co-encadrant

Thèse de doctorat

NNT: 2021UPAST060

Remerciements

Avant tout, je tiens à remercier les membres du jury d'avoir accepté ce travail. Malgré le contexte sanitaire, la soutenance et tous les processus derrière s'est déroulée de manière impeccable. Je remercie les Prof. Christian Hasse et Guillaume Legros d'avoir accepté le rôle de rapporteurs de mon manuscrit. Encore merci au Prof. Legros pour avoir présidé le jury le jour de ma soutenance.
Je remercie mon directeur de thèse Benoît et co-encadrant Nasser pour la suivie continue, les conseils et avoir contribué énormément dans la réalisation de ma thèse. Merci pour les remarques, la patience et les longues heures de travails ensemble (surtout dans la dernière partie de la thèse et l'écriture des papiers). J'apprécie beaucoup la transmission de vos expériences et connaissances, le soutien dans les moments difficiles et le support pour mon développement professionnel.
Je remercie les collaborateurs que j'ai rencontré pendant la période de thèse aussi. Je commence pour remercier Alberto Cuoci pour les discussions fructueuses et des conseilles sur la modélisation des suies, pour m'avoir aidé à mettre en place les simulations sur laminarSmoke et la visite collaboratif au CRECK Modeling Lab, une très bonne expérience. Je remercie Ulrich Maas pour permettre la visite I'ITT à Karlsruhe, aussi une très bonne expérience qui a permis d'explorer des nouvelles approches mathématiques pour améliorer la méthode virtuelle, ainsi que pour les rencontres et discussions dans des conférences et workshop (avec son équipe). Du labo, je suis reconnaissant à Denis Veynante, qu'avec ses remarques et son aide on a pu developper un modèle dans le dernier chapitre, ainsi que pour les échanges enrichissantes et des histoires amusantes. Je suis également à Ronan Vicquelin de m'avoir fourni des profils de vitesse de la flamme turbulente du dernier chapitre.
Brigitte, Nathalie et Noï pour tout le support administratif et les discussions amusantes dans les bureaux, les couloirs ou la caféte. Jean-Michel pour sa disponibilité et soutien au niveaux des calculateurs et debugging de compilation et également Sébastien Turgis dans le côté informatique. Merci le directeur Sébastien Ducruix pour les mots encourageants et le soutien pendant mon passage au laboratoire. Merci à Franck Richecoeur, Aymëric Vié, Laurent Soucasse et Sean McGuire qui m'ont tenu en compte pour participer dans les missions complémentaires d'enseignement, une très bonne expérience et enrichissante pour ma formation. Je remercie également Juan Carlos Rolón et Philippe

Scouflaire qui m'ont toujours encouragé dans ma formation depuis les époques d'étudiant.
L'équipiers du team Constantin, Giampaolo, Tan-Phong et Yacine pour les bons moments, les discussions intéressantes dans les meetings et dans les bureaux, les heures de codage et des blagues. Merci encore Yacine pour les heures d'étude et boulot pendant le master, le soutien dans la thèse, les discussions dans le bus, les conférences et plus; on a beaucoup bossé (et voyagé) ensemble et je t'en suis toujours reconnaissant.
Je remercie mes co-bureaux à Guillaume, Livia, Giunio, Victorien, Enrico; les amis de la rentrée 2017-2018, Mr Karl, Kevin et Mateo; et des autres bureaux Thomas, Junghwa, Arthur, Nicolas, Milan, Robin, Pierre, Victor, Guilhem, Roxanne, Augustin, Pedro, Lorella, Amanda, Abi et plusieurs d'autres qui ont passé pour le labo, pour les bons moments ensemble dans les pauses café, les repas, les conférences ou formations, les sorties, les discussions intéressantes et les rigolades. J'ai bien aimé mon passage au laboratoire aussi grâce à vous et j'espère pouvoir vous rencontrer dans le futur.
Gracias a mis amigos Juan Pablo, Arturo, Fahd, Alexia, Irma, Agus, Sonia, Diego Z, Diego B, Caro, Guille, Pats y muchos más por acompañarme en este viaje y experiencia en Europa o desde donde fuese, los quiero mucho.
Me toca agradecer a mi familia. A mis papás Teresa y Hugo, y mis hermanas Eliana y Sofía, enormes gracias por el apoyo y la comprensión a lo largo de la tesis (desde el master incluso), siempre atentos y deseando lo mejor. Mucho amor para ellos. Este trabajo va dedicado a papá.

Abstract

Modeling soot particles formation is a very difficult task because of interactions of several complex physical phenomena. Numerical simulation of turbulent sooting flames implies development of elaborate soot models often too computationally demanding. Also, simplified soot models are limited to a small range of operating conditions of interest. Here, an innovative optimized global approach called virtual chemistry is proposed. It consists of a mathematical formalism including virtual species and virtual reactions, whose thermochemical parameters are optimized by a genetic algorithm using a learning database made of reference flame elements. This makes possible to reproduce the structure of hydrocarbon-air flames, as well as predicting specific user-defined pollutants, here soot volume fraction, for multiple combustion regimes and operating conditions. The final reduced chemistry consists of 12 virtual species and 6 virtual reactions, which considerably decreases the computational time compared to detailed chemistry models. As the radiative heat losses are important in sooting flames, a new radiative virtual model is also developed to account for them. Simulations of 1-D and 2-D laminar ethylene-air sooting flames are performed to evaluate the virtual soot and radiative models. Temperature, soot volume fraction and radiative heat losses are well predicted and are in good agreement with the reference data. Then, the developed virtual models are challenged in Large Eddy Simulations (LES) of turbulent sooting flames. As the turbulent combustion characteristic times are very small compared to those of soot particles production, a new subgrid-scale model is proposed here to manage the filtered soot source terms in a virtual chemistry framework. The new virtual chemistry, radiative and subgrid-scale models are challenged in a 3-D sooting turbulent non-premixed ethylene-air flame. Results are validated with experimental data and detailed chemistry computations.

Résumé

La modélisation de la formation de particules de suies est une tâche très difficile en raison des interactions multiples de plusieurs phénomènes physiques complexes. Les simulations numériques des flammes turbulentes produisant des suies impliquent le développement de modèles de suies élaborés souvent trop exigeants en termes de calcul. D'autre part, les modèles simplifiés de suies sont limités à une petite gamme de conditions de fonctionnement d'intérêt. Une approche globale optimisée et innovante, appelée chimie virtuelle, est proposée ici. Elle consiste en un formalisme mathématique comprenant des espèces virtuelles et des réactions virtuelles, dont les paramètres thermochimiques sont optimisés par un algorithme génétique, en utilisant une base de données d'apprentissage constituée d'éléments de flammes de référence. Elle permet alors de reproduire la structure des flammes hydrocarbures-air, ainsi que la prédiction d'espèces polluantes spécifiques définies par l'utilisateur, ici la fraction volumique de suies, pour de multiples régimes de combustion et conditions de fonctionnement. La chimie réduite finale consiste en 12 espèces virtuelles et 6 réactions virtuelles, ce qui réduit considérablement le temps de calcul par rapport aux modèles chimiques détaillés. Comme les pertes de chaleur radiative sont importantes dans les flammes de suies, un nouveau modèle virtuel radiatif est également développé pour en tenir compte. Des simulations de flammes éthylène-air laminaires 1-D et 2-D sont réalisées pour évaluer les modèles virtuels de suies et radiatifs. La température, la fraction volumique de suies et les pertes thermiques radiatives sont en bon accord avec les données de référence. Ensuite, les modèles virtuels développés sont mis à l'épreuve dans les simulations à grands échelles d'air (LES) de flammes turbulentes. Les temps caractéristiques liés à la combustion turbulente étant très courts comparés ceux de la formation des particules de suies, un nouveau modèle à l'échelle de la sous-maille est proposé ici pour gérer les termes filtrés de la source de suies dans un cadre de chimie virtuelle. Les nouveaux modèles de chimie virtuelle, radiatif et de sous-maille sont mis à l'épreuve dans une flamme turbulente 3-D éthylène-air non prémélangée. Les résultats sont validés avec des données expérimentales et des calculs de chimie détaillée.

Contents

List of Tables

List of Figures

Introduction

General context

Data analyses reveal significant growing in the Total Energy Supply (TES) from fossil-fuels in the last 30 years. Figure 1 shows the global evolution of the TES in ktoe (1 ktoe ≈ 42 GJ) by source of energy from 1990 to 2018, published by the International Energy Agency (IEA, IEA (2020a)). The contribution of

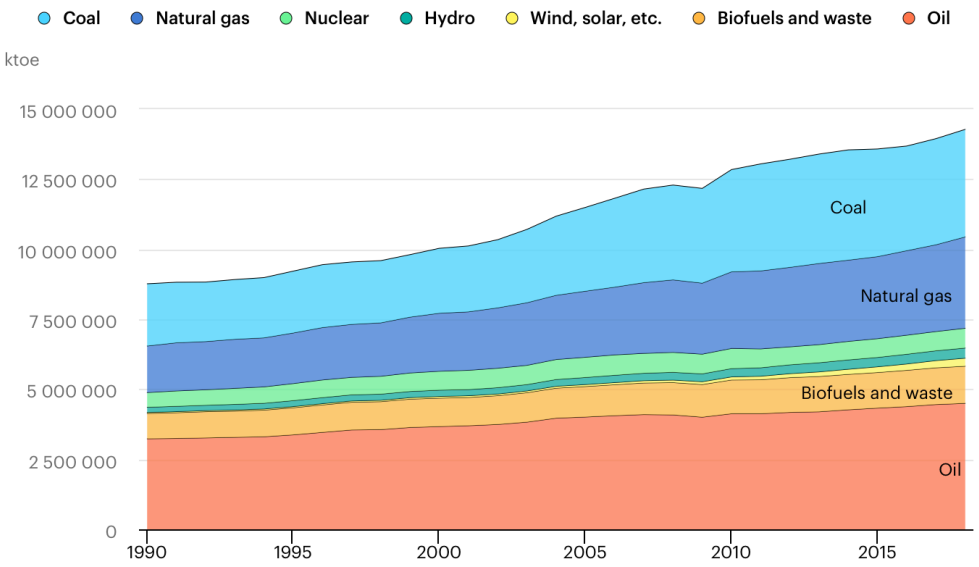

Figure 1: *Evolution of the worldwide Total Energy Supply (TES) by source, years 1990 to 2018 (IEA (2020a)). Data and statistics from IEA website (https://www.iea.org)*

non-renewable fuel sources to the TES has clearly increased throughout the years. Their growth for each primary energy source are estimated as:

- oil: about 39%,
- coal: about 73%,
- natural gas: about 96%.

This means that about 81% of the TES in 2018 ended up with the com-

bustion of fossil fuels. Considering biofuels and waste primary (renewable) sources, combustion processes represent 90.5% of the total share. Renewable non-combustible energy sources still constitute a relatively small portion of the TES, in which wind and solar technologies have experienced an impressive leap of 683% in recent data since 1990 (IEA (2020a)).
Statistical trends of the primary energy demand are developed for a broad range of energy possibilities in the future years, considering different factors: such as energy market data, energy technologies, public health, etc. For this purpose, the IEA proposed different energy scenarios in its Energy Outlook 2020 (IEA (2020b)):

- *Stated Policies Scenario* (STEPS): indicates current announced policy intentions and targets.
- *Delayed Recovery Scenario* (DRS): similar to STEPS but includes an enduring damage on economic prospects due to the current pandemics.
- *Sustainable Development Scenario* (SDS): designates an integrated approach in order to accomplish sustainable energy goals, including the Paris Agreement (2015), energy access and air quality.

Figure 2 shows the tendencies of global primary energy demand growth for different scenarios, from 2019 to 2030. The original projection indicated an increase of 12% of the global primary energy demand by 2030. However, new projections decrease due to the energy crisis, recovering the 2019 level between 2022 (STEPS) and 2025 (DRS). By 2030, the energy demand growth is expected between 5% to 9%.
In SDS projections (IEA (2020b)), the combustion processes of coal and oil are expected to be respectively reduced by 64% and 34% of the current global demands by 2040, and will be substituted by natural gas. However, STEPS projections indicate 10% reduction in coal global demand and 3% increase in oil global demand (IEA (2020b)). These prospects stipulate the introduction of more efficient conversion devices and low-carbon technologies in the different combustion processes.
Combustion processes are expected to last for a long period of time in the future, until the energy transition to efficient green technologies is achieved. During this period, the main concern of hydrocarbon fuels burning processes is the big impact of the combustion products (pollutants) on human health and the environment. Therefore, for the conception of efficient and clean combustion devices, it is important to control the pollutant formation.
The research topic of this thesis focuses on pollutant emissions from combustion processes in industrial applications.

Pollutant formation in combustion processes

Combustion processes in industrial applications lead to the generation of pollutants. Regulation policies exist to limit pollutant concentration in the exhaust

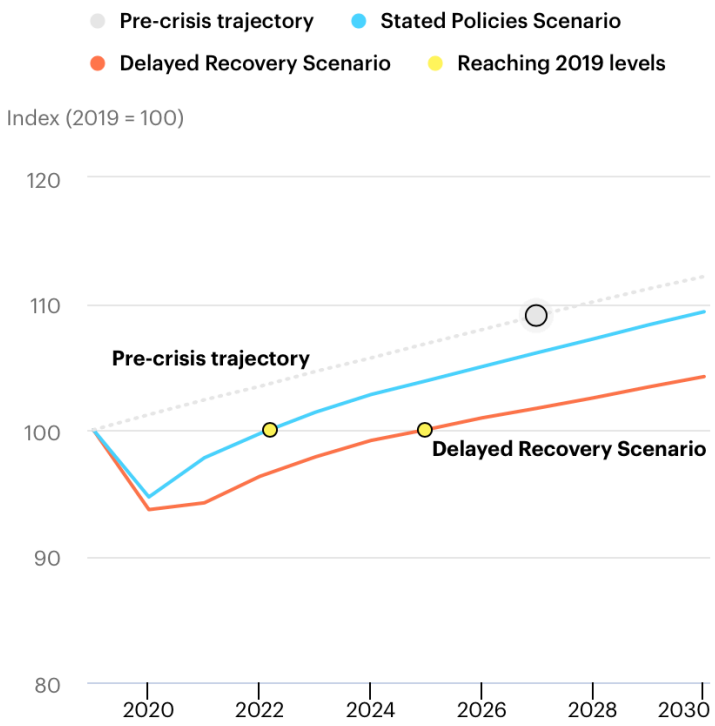

Figure 2: *IEA estimations of the global primary energy demand growth by scenario, 2019 to 2030 (IEA (2020b)). Data and statistics from IEA website (https://www.iea.org)*

gases of combustion processes, such as CO_2, CO, NOx, soot, etc. Concentration margins are imposed to the industrial manufacturers, based on the effects on the air quality, global climate, human health, etc. Thus, scientific research is made on this topic, which eventually results in the development of technical specification sheets for the conception of combustion devices.

An example of pollutant formation from combustion processes in a conventional aircraft engine is presented in Fig. 3 (Masiol and Harrison (2014)). Figure 3(top) shows the fuel burning process in the combustion chamber and the combustion products at the exit nozzle. In actual aircraft combustors, due to incomplete combustion both gas and solid pollutants are encountered in the exhaust gaseous mixture. The diagram of Fig. 3(bottom) shows the complex reactive pathways for each pollutant and their negative effects on the environment and on humans. Several physico-chemical processes take place at the atmospheric level. Greenhouse gases, such as CO_2, are not the only source of global warming: NOx, HCs (hydrocarbons), V-PM (volatile particulate matter), SO_2 and soot particles are also contributing. Examples of the various effects on humans are also listed for each pollutant species. Studies of all these phenomena are therefore very important to understand the different channels of pollutant formation and how to mitigate or control them.

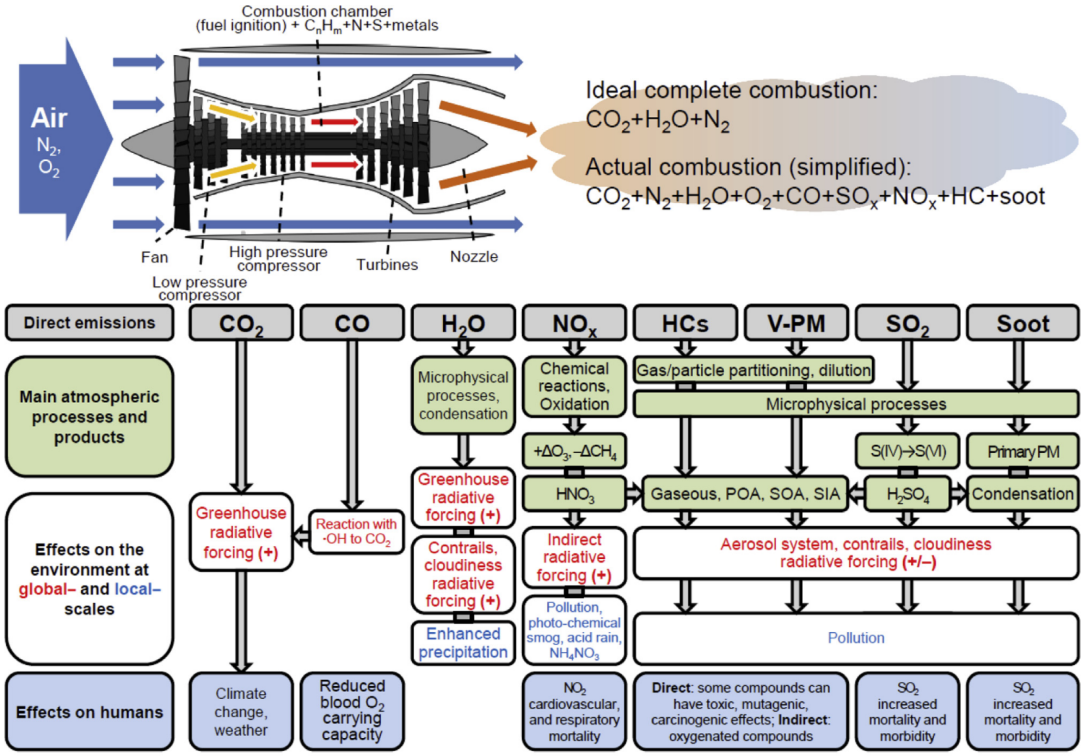

Figure 3: *Top: Diagram of pollutant formation in combustion processes in a conventional aircraft combustor. Bottom: Chart flow describing the main physico-chemical processes of different pollutants from combustion and their effects on the environment and humans. Extracted from Masiol and Harrison (2014).*

It is known in gas turbines combustion chambers that temperature has an important influence on pollutant formation. Figure 4 shows the influence of primary-zone temperature on CO and NOx formation (Lefebvre and Ballal (2010)). The range of operating temperatures in a typical combustion chamber varies between 1000 K to 2500 K (Lefebvre and Ballal (2010)). CO production increases at temperatures lower than 1670 K, while overproduction of NOx is triggered at temperatures higher than 1900 K (Lefebvre and Ballal (2010)). The region for low CO and NOx emissions is therefore limited between these two temperatures. Thus, the aim is to find the optimal operating range(s) of temperatures in which the gas turbine must operate to ensure both high efficiency and low emissions at the same time.

Another example of pollutant formation from combustion processes is given in diesel internal combustion engines. Here, fuel ignites in a highly-compressed control volume. Non-premixed combustion takes place in the engine cylinder which leads to NOx and soot production. In this case, the local mixture composition plays also an important role. Figure 5 shows a diagram of high NOx and soot formation regions influenced by the local equivalence ratio and local

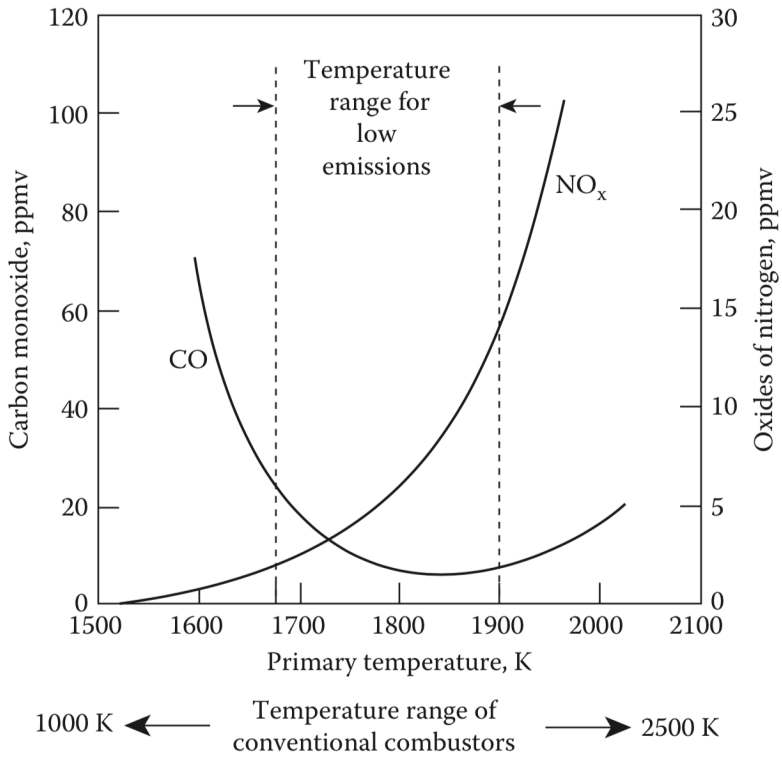

Figure 4: *Influence of primary-zone temperature on CO and NOx formation in gas turbine combustors. Extracted from Lefebvre and Ballal (2010).*

temperature (Dempsey et al. (2016)), including a representation of the diesel combustion process. NOx is likely to form in regions of high local temperatures ($T > 2200$ K) and lean to moderately rich mixtures ($\Phi < 2$). Soot is produced at very rich regions ($\Phi > 2$) but at lower temperatures than NOx (1400 K $< T <$ 2500 K). To reduce both NOx and soot formation, the diesel combustion process should ideally take place closer to the low temperature combustion (LTC) zone (Kitamura et al. (2002); Dempsey et al. (2016)), as indicated by the green region in Fig. 5, without compromising the efficiency of the engine.

Numerical simulations in CFD

The conception of efficient combustion devices with low pollutant emissions is a very challenging task in engineering. Experimental procedures remains costly and numerical simulations seems to be a right answer in this regard. The main advantage of numerical studies compared to experimental ones is the broad access to the flame physico-chemical characteristics and at multiple scales. In this matter, the reliability of the mathematical model is very important to well describe the physical phenomena. Mathematical models for combustion

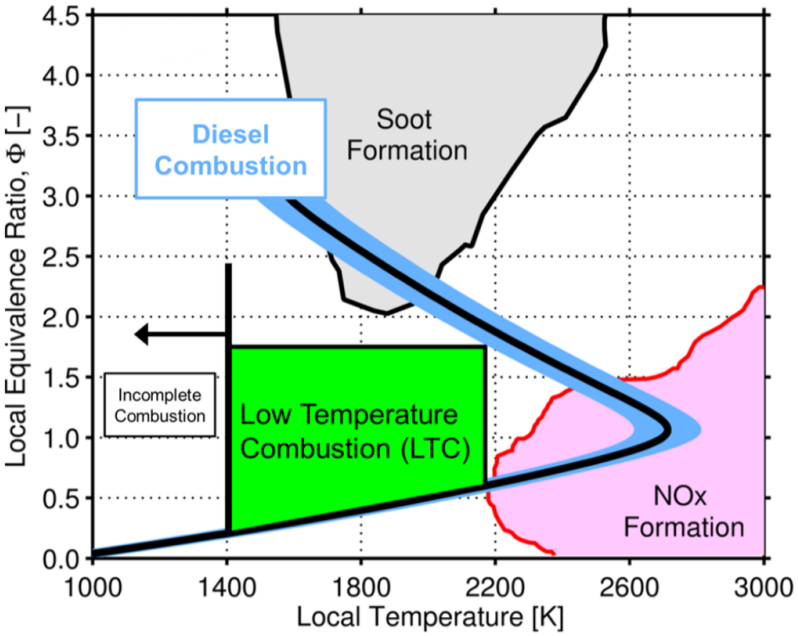

Figure 5: *Soot and NOx formation regions in a local equivalence ratio Φ vs. local temperature T space. Extracted from Dempsey et al. (2016).*

phenomena are known to be very complex, which entail the use of massively-parallel computing systems, especially for industrial combustor simulations. Eventually, numerical methods are necessary to overcome with this issue. In this thesis, the Large-Eddy Simulation (LES) approach is chosen for turbulent combustion simulations.

Nowadays, Computational Fluid Dynamics (CFD) programs are employed to simulate both laboratory- and industrial-scale combustion devices. Using LES formalism, these numerical tools manage to solve turbulent reactive flows. One major challenge in numerical combustion is to predict pollutant formation properly in unsteady turbulent reactive flows in CFD simulations. Numerous examples of turbulent flame configurations exist where pollutant formation models were tested: CO (Franzelli et al. (2013); Jaravel et al. (2017); Maio et al. (2019)), NOx (Ihme and Pitsch (2008); Pecquery et al. (2014); Jaravel et al. (2018)), soot (Mueller and Pitsch (2012a); Rodrigues et al. (2018); Franzelli et al. (2019); Gallen et al. (2019)), etc. The quality of pollutant prediction results depends essentially on the kinetic model used in the simulations.

Numerical soot modeling in CFD

Hydrocarbon/air combustion occurring in rich and incomplete conditions in practical industrial applications causes the formation of undesirable soot particles. Soot formation results from both highly complex gas phase chemistry and

particles dynamics including nucleation, condensation, coalescence, and surface reactions such as surface growth and oxidation. Because of the complexity of these physico-chemical phenomena, numerical computations of gas chemistry together with particles dynamics request high amounts of CPU time, which quickly become an issue for the simulation of practical combustion chambers.
The gaseous chemical kinetics including soot precursors needs a high number of species and reactions (Saggese et al. (2015)) so that detailed schemes generally cannot be directly employed in CFD of sooting flames. Three main routes for kinetics reduction techniques are in principle possible (Fiorina et al. (2015); Fiorina (2019)):

- Direct Chemistry Reduction (Lu and Law (2008); Pepiot (2008)),
- Tabulated Chemistry (Peters (1984); Maas and Pope (1992a)),
- Optimized Global Chemistry (Westbrook and Dryer (1981); Franzelli et al. (2010)).

Thanks to recent progresses in computational resources and in the automation of chemistry reduction techniques (Pepiot (2008)), analytically-reduced schemes have been recently used for LES of turbulent sooting flames (Felden et al. (2018); Gallen et al. (2019)). Despite impressive results, the remaining high number of species and the numerical stiffness of the system make difficult the systematic use of analytic schemes in a practical combustion chamber design process. Application of tabulated chemistry to soot formation is more frequent. It consists in storing complex chemistry up to polycyclic aromatic hydrocarbons (PAHs) in look-up tables, parametrized by a reduced set of thermochemical variables (Mueller and Pitsch (2012b); Rodrigues et al. (2018)). Despite its very low CPU cost, the tabulated chemistry approach is not able to well predict multi-regime combustion (Fiorina et al. (2015)). Finally, literature presents a few attempts to optimize global mechanisms to predict soot precursor formation (Said et al. (1997); Kollmann et al. (1994); Franzelli et al. (2015)). In these studies, a global mechanism is adopted to describe the gas chemistry and soot formation is described using a simplified chemistry.
The complexity of solid particles dynamics has motivated the development of a wide variety of models such as (sorted from high to low computational demand): Lagrangian models (Celnik et al. (2007); Gallen et al. (2019)), Chemical Discrete Sectional Model (Pope and Howard (1997); Saggese et al. (2015); Pejpichestakul et al. (2019)), Aerosol Discrete Sectional model (Smooke et al. (1999); Rodrigues et al. (2018); Blacha et al. (2012); Eberle et al. (2017)), or Method of moments (Frenklach and Harris (1987); Mueller et al. (2009b); Salenbauch et al. (2019)). Finally, empirical and semi-empirical methods (Tesner et al. (1971); Moss et al. (1989); Said et al. (1997); Leung et al. (1991)) have been developed to track the soot volume fraction and particle number density, and eventually the particle size distribution (Franzelli et al. (2019)). Such approaches are attractive because of their very low CPU cost, but in contrast, they are limited to a small range of operating conditions. In most cases, the parameters are a function of the adopted fuel. Typically, semi-empirical models,

together with their parameters, are strictly connected with the reduced scheme on which they were developed. Indeed, if the reduced chemistry is changed, or replaced with a more accurate/complex one, the soot prediction can completely fail. It should be underlined that whatever is the complexity of the soot particles model, its accuracy obviously depends on the accuracy of the reduced chemical scheme designed to model the soot precursor formation.
A new methodology called Virtual Chemistry was proposed in Cailler (2018) thesis. It consists in a global optimized chemistry able to reproduce the flame characteristics, such as mixture properties at equilibrium, laminar flame speed, and flame temperature. The approach has been extended in order to predict pollutant formation, such as CO (Cailler et al. (2020)) and NOx (Maio et al. (2020)). The virtual chemistry method constitutes an alternative reduced model to perform LES of turbulent flames in multiple combustion regimes and at low CPU cost (Cailler et al. (2017); Maio et al. (2019); Maio et al. (2020)). The present work aims at extending this technique to predict soot formation in laminar and turbulent flames.

Thesis contributions and scope

This work aims at developing a reduced kinetic mechanism for soot formation prediction in hydrocarbon-air combustion at low CPU cost, based on the virtual chemistry approach (Cailler (2018)). Sooting flames are known to present significant radiative heat losses. Therefore, a new virtual model for gas and soot radiation is also developed.
Throughout this thesis work, numerous new features are implemented to the virtual approach in REGATH package (Darabiha and Candel (1992)) as well as the optimization algorithm from Cailler (2018):

- An original optimization strategy is implemented, which differs from works of Cailler (2018) and Maio (2020). Here, 1-D premixed flames cover the extinction limits. However, such target flames are unable to capture the soot produced in 1-D non-premixed flames at positions beyond the rich extinction limit. To overcome this issue, a set of 1-D non-premixed flames at different strain rates is considered in the optimization learning database.
- Lewis number of soot virtual species greater than one is considered. This differs from the original formulation of the virtual approach in which all virtual species diffuse with the same unity Lewis number assumption.
- The optimization algorithm is extended in order to include 0-D (auto-ignition and perfectly-stirred reactor) and 1-D combustion simulations in REGATH using the virtual approach. Now it is possible to perform both calculations and optimization in different combustion configurations (in time and space) simultaneously.

The virtual models for chemistry and radiation are first validated in 1-D laminar

ethylene-air flames in premixed and non-premixed canonical configurations. The virtual models are then challenged into 1-D burner-stabilized premixed flames, which are included in the International Sooting Flame (ISF) workshop target flames (ISF5 (2021)).
Next, the virtual models are applied to CFD simulations: 2-D premixed slot burner and 2-D non-premixed coflow burner from Santoro et al. (1983). The second one is included in the ISF target flames. The virtual models for chemistry and radiation are then validated in the 2-D premixed and non-premixed configurations.
Finally, a new subgrid-scale model to capture turbulence-soot interactions is proposed for 3-D turbulent flame simulations, based on observations of laminar flame time and length scales analyses. The turbulent sooting flame from Zhang et al. (2011) is considered, which is also included in the ISF target flames. The new virtual models for chemistry, radiation and subgrid-scale turbulence-soot interactions are implemented in the CFD code YALES2 (Moureau et al. (2011)) and simulation results are validated against numerical and experimental data.

Thesis outline

This manuscript is divided in five chapters:

- **Chapter 1**: Complex physico-chemical phenomena of soot formation are first described. Then, numerical modeling of the gas and solid phases are shown. A small review of soot modeling in LES is then presented. This leads to the formulation of the objectives and methodology of this thesis.
- **Chapter 2**: The virtual chemistry methodology in presented. First, the virtual main mechanism is tackled. Then, the state of the art of pollutant prediction using the virtual approach is presented. The transport equations of reactive flows are finally described in the virtual chemistry framework.
- **Chapter 3**: After a review of the virtual chemistry principle in laminar flames, the virtual soot sub-mechanism is developed and an optimization strategy is deduced. Next, the virtual model for radiative heat transfer is described. The new virtual models for chemistry and radiation in ethylene-air combustion are then validated in 1-D laminar flames and challenged to 2-D laminar flames. Results are eventually compared to numerical and experimental data
- **Chapter 4**: The fundamentals of turbulent combustion modeling and briefly presented. The LES approach is introduced and LES closures are presented. A brief description of the turbulent combustion models for LES is reported. The TFLES approach is then presented.
- **Chapter 5**: The new virtual soot mechanism and radiative models are here applied to turbulent sooting flames. The virtual model is coupled to the LES framework. Then, time and length scales analyses of laminar

flames lead to the development of a new subgrid-scale (SGS) model for turbulence-soot interactions using the virtual approach. Next, the experimental and numerical setup are presented. Finally, the virtual models for chemistry, radiation and SGS turbulence-soot interactions are challenged to a 3-D turbulent sooting flame. Results are compared to numerical and experimental data.

Chapter 1

Soot formation modeling in combustion systems

Contents

In this chapter the fundamentals of soot phenomena theory and modeling for numerical combustion are examined. First, the physico-chemical description and mathematical representation of soot formation in combustion are introduced. The numerical modeling of soot evolution is separated in two parts. In a first step, gas-phase kinetics models are presented. In the second step, solid-phase modeling of soot particles interactions is discussed. Next, an analysis of previous works on soot modeling in turbulent sooting flames is done, including a few words about the idea of using virtual chemistry in them. Concluding this chapter, a reference detailed mechanism will be chosen and a strategy will be adopted for soot modeling using the virtual chemistry approach.

1.1 Physico-chemical description of soot formation

Combustion of hydrocarbon fuels under ideal stoichiometry conditions leads to a maximum heat release. In reality, practical applications show that incomplete combustion is sometimes possible, at least locally, causing the formation of soot particles. Convert molecules of fuel hydrocarbons containing few carbon atoms into a carbonaceous agglomerate carrying millions of other carbon atoms is an extremely complicated process and presents a gaseous-solid transition where the solid exhibits no unique chemical and physical structure Frenklach and Wang (1994).
The schematics in Fig. 1.1 displays the general pathways of soot formation (Wang and Chung (2019)).

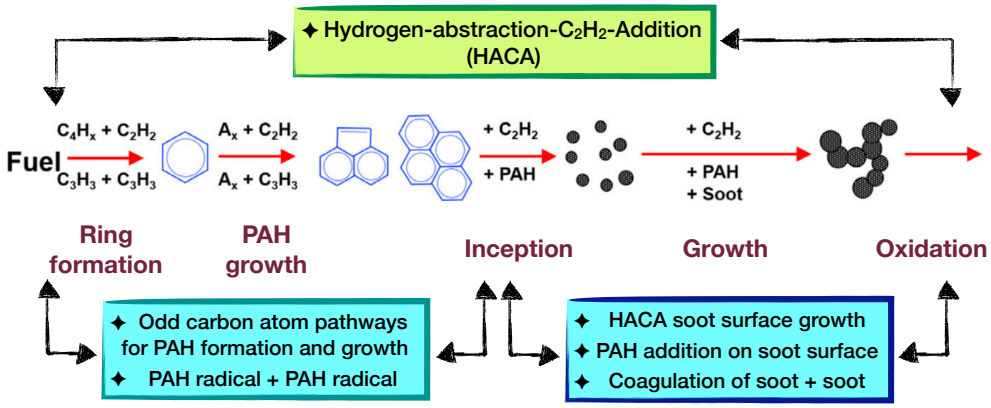

Figure 1.1: *Schematics of soot formation phenomena. Extract from Wang and Chung (2019)*

Soot formation begins with the formation of gas-phase molecular species from fuel pyrolysis, followed by incipient ring formation, PAH growth, particle nucleation, heterogeneous surface reaction, and particle-particle interactions (Wang and Chung (2019)).
Soot formation is largely determined by the chemistry that forms and converts small hydrocarbons radicals, soot precursors and its derivates (Frenklach and Wang (1994)). Curran (2019) stated that, for instance, it requires around 30 species to describe the oxidation of methane; but it requires numerous more if pyrolysis conditions are involved, *i.e.* including the addition of poly-aromatic species. Indeed, soot precursors are formed without oxidation in very rich fuel pyrolysis regions and are hence more likely to occur in non-premixed flames than in premixed flames.
High Resolution Transmission Electron Microscopy (HRTEM) unveils that soot particles are predominantly constituted of PAHs, which are then taken as the preponderant class of precursors (Vander Wal et al. (2007)). Formation of PAHs is now widely accepted to be the answer filling the gap between the gas phase and solid soot particles, but detailed reaction pathways are still needed

to validate this hypothesis against measurements (Wang and Chung (2019)).
The Hydrogen-Abstraction-C_2H_2-Addition (HACA) mechanism is the most recognized pathway for PAH growth and was developed by Frenklach and Wang (1994). Essentially, it consists of two repetitive chemical steps: the first corresponds to the abstraction of hydrogen atom forming an active radical, and the second to the addition of acetylene on the radical site.
In Fig. 1.2 the HACA mechanism for benzene (C_6H_6) is represented. In step (i) the acetylene meets a benzene radical in the addition process. A new active radical is created in step (ii), when hydrogen atom goes out of the carbon molecule, caused by the influence of another atom of hydrogen in the surroundings. Similar behavior happens to the benzene when it becomes a radical, which appears in step (i). In step (iii) a new C_2H_2-addition occurs and a new ring is formed. A new cycle is then given in step (iv), which is repeated indefinitely giving place to larger PAHs.

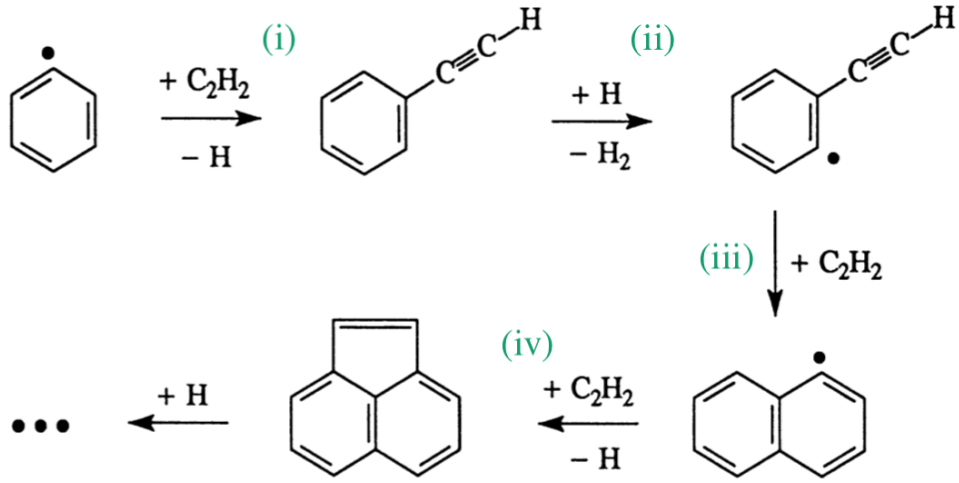

Figure 1.2: *HACA reaction pathway of PAH growth. From Frenklach and Wang (1994)*

Let A_i and A_i^* represent respectively the aromatic species and its radical with i-number of rings. The minimal reaction set for HACA mechanism is (Frenklach and Wang (1994)):

$$A_i + \mathrm{H} \Leftrightarrow A_i^* + \mathrm{H}_2; \qquad (R_1^{\mathrm{HACA}})$$

$$A_i^* + \mathrm{C_2H_2} \Leftrightarrow A_i\mathrm{C_2H_2}*; \qquad (R_2^{\mathrm{HACA}})$$

$$A_i\mathrm{C_2H_2} * + \mathrm{C_2H_2} \Rightarrow A_{i+1} + \mathrm{H}. \qquad (R_3^{\mathrm{HACA}})$$

Introducing the oxidation produced by the environment:

$$A_i^* + O_2 \Rightarrow products; \qquad (R_5^{\mathrm{HACA}})$$

PAH removal by oxidation occurs predominantly via molecular oxygen attack on aromatic radicals. Similar reactions could be written for OH and O (Frenklach and Wang (1994)). Presence of oxygen molecules also promotes PAH formation by strengthen fuel pyrolysis and thereby production of hydrogen atoms and critical intermediates species (Frenklach and Wang (1994)).
Although in pyrolysis of hydrocarbon fuels, reactions of aromatic rings with species other than acetylene may be important initially, as the pyrolysis progresses, the aromatic growth becomes dominated by the HACA reaction sequence (Frenklach and Wang (1994)) and a few stable aromatic molecules are formed (naphtalene, pyrene, coronene, etc.). In these reactions, the change of Gibb's free energy is large enough to be considered irreversible and therefore to drive the sequence towards larger PAH molecules formation (Frenklach and Wang (1994)). Also, the formation of a large PAH species can be obtained through several pathways. While the HACA mechanism is likely to be the backbone in models of PAH formation, other pathways and their varying sensitivity to the fuel composition raise the question whether there can be a quantitative closure to this problem (Wang (2011)).
The diagram in Fig. 1.3 illustrates a typical transition from the gaseous phase to the solid phase in soot formation, and the nature of all interaction in each step. PAHs molecules grow until they reach a characteristic size, and after collision between two of them (*cf.* (I) in Fig. 1.3), they are considered to be in an intermediate phase between gas and solid called dimer (Schuetz and Frenklach (2002); Frenklach and Wang (1991)). Investigations (Dobbins (2007); Cain et al. (2010)) have shown that nascent soot particles present a liquid-like phase and are not fully carbonized. Soot Inception is typically modeled as the collision of two dimers (Blanquart and Pitsch (2007); Mueller et al. (2009b)), where the solid phase is finally reached (*cf.* (II) in Fig. 1.3), and hence a gain in the mass and number of total soot particles is implicated. According to Frenklach (2002b), this transition is probably the least known process of soot formation.
Wang (2011) declared that there are three conceptual reaction channels proposed in the literature for soot nucleation. The first of them is described by the growth of "two-dimensional" PAHs into curved, fullerene-like structures (Homann (1998)). The other two propositions involve the physical coalescence of moderate-sized PAHs into stacked clusters (Frenklach and Wang (1994); Miller (1991); Herdman and Miller (2008)) and the reaction or chemical coalescence of PAHs into cross-linked three-dimensional structures (Richter et al. (2000); Ciajolo et al. (2001); Allouis et al. (2003); Violi et al. (2002); Violi et al. (2004); D'Anna (2007)), respectively.
Particles collisional phenomena for soot is initiated with soot nucleation ((II) in Fig. 1.3). In addition, two other collisional interactions of soot particles

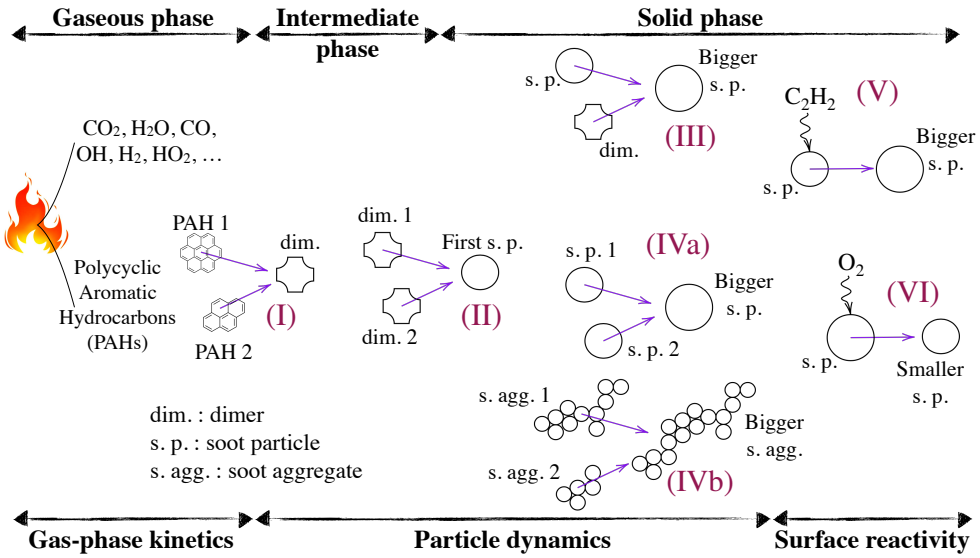

Figure 1.3: *Diagram of the physico-chemical phenomena of soot formation: transformation from the gaseous phase to the solid phase and the nature of each interaction throughout it.*

are found: soot condensation and soot coalescence ((III) and (IV) in Fig. 1.3, respectively); and both promoting soot growth. The condensation is defined as the collision of soot particles with PAHs or dimers, increasing their size but without changing the soot particles number density.

Soot coalescence is classified in two categories: coagulation and agglomeration. Coagulation is given when two spherical soot particles collide ((IVa) in Fig. 1.3). Agglomeration refers to the formation of a soot aggregate by collision of two smaller aggregates, if no sphericity of the particles is assumed ((IVb) in Fig. 1.3). In these processes, the soot particles number density decreases while the size grows.

Surface growth describes the chemical reactivity on the surface of a soot particle with other species in the medium ((V) in Fig. 1.3), *i.e.* gaseous species attach to the surface of pre-existing soot particles (Haynes and Wagner (1982)). Thus, it increases the total mass of soot particles but not their total number. It is generally assumed that the majority of soot mass comes from surface growth (Haynes and Wagner (1982)). Indeed, Kennedy (1987) showed that in counter-flow diffusion flames 90% of the final soot volume comes from surface growth. Although surface growth accounts for the majority of soot mass, ultimate particle size and morphology are largely influenced by particle-particle interactions (Wang and Chung (2019)).

Oxidation of soot particles impedes soot growth and is also the primary mechanism for their removal from combustion exhausts ((VI) in Fig. 1.3). Thus, oxidation induces a reduction of total soot particles mass but does not have

impact on the total number of soot particles. Most important soot oxidants are molecular O_2 and OH radical, with contributions also from O atom, H_2O, CO_2 and NO_2 (Stanmore et al. (2001); Cavaliere et al. (1994)).
To handle each phenomenon mentioned above in numerical simulations mathematical models are required. A recurrent technique is to split the problem into modeling the kinetics of the gas phase and the interactions of the solid particles, as well as convenient assumption for the transition state that links the two phenomena. Re-examining the Fig. 1.3, the first step is to adequately achieve PAHs formation with the kinetic model of the gas phase, which should cover all collision combinations for the dimerization process in (I). Dimers will collide in step (II) and form soot particles from different joints: shape and size are two characteristics that describe soot particles evolution from now on and a hypothesis for this transition should be made. Soot particle dynamics need a model that deals with phase, size and shape of the particles (or aggregates) that are colliding, as in (III), (IVa) and (IVb). Finally, the reactive gas-solid interactions that occur at the surface of soot particles must also be modeled, as in (V) for soot surface growth and in (VI) for soot oxidation. In the following sections gas-phase kinetics and solid-phase modelings are presented.

1.2 Gas-phase kinetics modeling

Soot modeling implicates to have a good description of the gas phase, especially to take care of soot precursors (*e.g.* PAHs) and other species that participate in the soot surface reactivity, as mentioned in section 1.1. In this circumstances, the kinetic knowledge needed is very different from that utilized to predict basic flame properties, such as the laminar flame speed or ignition delay, which are usually governed by a small number of elementary reactions common to all hydrocarbon fuels (Wang (2011)). It is currently not well known whether the number of pathways for PAHs and soot in real fuels combustion can be assumed to be limited, given the large variability in fuel composition (Wang (2011)). This suggests to continue the effort of well characterizing the kinetics that leads to soot formation. In the following subsections, the gas-phase kinetics will be described taking into account the level of details included in the kinetic scheme.

1.2.1 Detailed kinetics

Detailed thermo-chemistry databases aim to include all species and elementary reactions involved in the oxidation process of hydrocarbon fuels (Curran (2019)).
Detailed kinetic schemes are conceived to have access to an adequate description of the flame chemical reactive region in a wide variety of operating condition: temperature, pressure, mixture composition, and flame regimes (Mehl et al. (2011)). The effort made by the combustion kinetic research community allows

today to have access to detailed kinetic databases, valid for a large variety of hydrocarbon fuels and wide operating conditions (Curran (2019)). Many experimental reactive systems could be recreated by using these kind of mechanisms: perfectly-stirred reactors (PSR), plug flow reactors (PFR), shock tube reactors (STR), auto-ignition and extinction phenomena, premixed and non-premixed flames, etc.

Detailed kinetic mechanisms, including PAHs for soot modeling, succeeded in characterizing soot formation in hydrocarbon flames very recently, taking care of the repercussion of different fuel compositions (Chernov et al. (2014); Wang et al. (2015)). Some PAHs growth pathways proposed for different hydrocarbon fuels are particularly dependent on their molecular structure, the pressure and the temperature (Richter and Howard (2000); Wang and Chung (2019)). The kinetic chemistry of the flame and the gas temperature can also have a big impact on the rate of formation of PAHs, resulting complicated to model and may need more understanding on the subject (Wang (2011)).

Curran (2019) updated the works of Lu and Law (2009) and Egolfopoulos et al. (2014) and illustrated the size of detailed kinetic mechanisms found in the literature for several hydrocarbon fuels, and is schematically represented in Fig. 1.4 in terms of number of reactions versus the number of species present in detailed mechanisms. A quick analysis of this figure suggests that the number of species and reactions present in a kinetic scheme grows linearly in the log-log diagram when the complexity of the hydrocarbon fuel is increased, *e.g.* going from methane to diesel or biofuels. However, it is noticeable that the kinetic mechanism jumps out of the log-log line if it incorporates prediction of soot and its precursors; *e.g.* CRECK soot mechanism Saggese et al. (2015), in which the number of species sharply surpasses 15000 reactions and reaches 300 species (referred as "Soot (CRECK), ver 1509" and shown by a circle in Fig. 1.4). This soot kinetic mechanism was validated for an extensive range of operating conditions (pressure, temperature and composition) and several applications such as PFR, STR, PSR, burner-stabilized flames, etc. (Saggese et al. (2013); Saggese et al. (2014); Saggese et al. (2015); Saggese et al. (2016)). Nevertheless, an accurate prediction of PAH and soot formation may require more precise knowledge of flame chemistry than is currently available (Wang (2011)). This fact becomes particularly relevant if models with detailed chemical kinetics and particle dynamics are to be employed for the simulation of these flames.

The more species and reactions are included in the gas kinetics, the more computational power will be necessary to solve a combustion problem. Therefore, the main drawback is that the CPU resources needed will evidently increase when the simulation includes both detailed mechanism and soot formation. An example published by Wang and Chung (2019) for a recent computational simulation (Eaves et al. (2016)) on an ethylene-air coflow flame. The numerical domain has about 60000 cells. A semi-detailed chemical reaction mechanism, with 105 species and 831 reactions (Slavinskaya and Frank (2009); Chernov

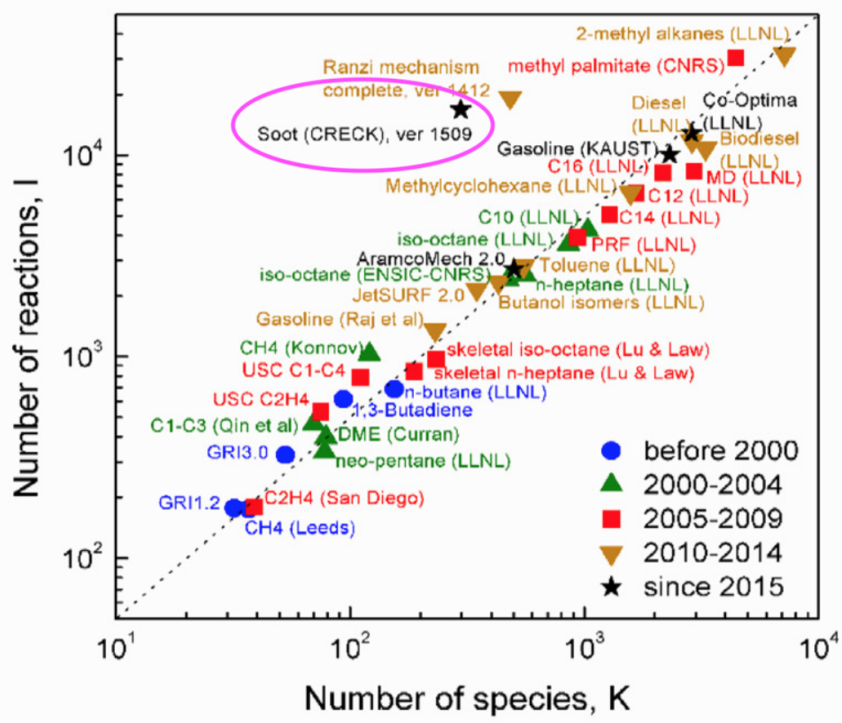

Figure 1.4: *Size of selected detailed mechanisms for several typical hydrocarbon fuels. A schematics taking their number of reactions versus their number of species . From Curran (2019). CRECK soot kinetics from Saggese et al. (2015) is located outside the log-log line trend.*

et al. (2014)), is chosen for the gas kinetics. A sectional soot model is selected, with 35 sections. It was reported to take a computing time of more than 60000 CPU hours for convergence. However, similar simulations of one-dimensional counterflow flames usually does not take more than a few hours on a personal computer (Wang and Chung (2019)).

Another limitation with detailed mechanisms is that they usually involve highly reacting radicals that have a life-span of the order of 10^{-9} s and are associated with very small length scales as well (Lu et al. (2009)), making the system of equations very stiff; whereas for a LES low Mach solver the typical flow time step is of the order of 10^{-6} s. As a result, it leads to a very expensive implicit temporal integration of the stiff source terms and for an accurate prediction of the phenomena it is necessary a very high mesh resolution (Lu et al. (2009)). The best alternative in such cases is to reduce the size of the detailed mechanism. Reduction techniques for kinetic mechanisms are then presented in the following subsection.

1.2.2 Reduced kinetics and their application to soot chemistry

A reduced mechanism is preferred to solve turbulent combustion problems of industrial applications at a low CPU cost. Strategies were reviewed not very long ago for large scale combustors Fiorina et al. (2015) and updated in Fiorina (2019). In the latter, three major routes for chemistry reduction in LES has been identified and are shown in Fig. 1.5, named:

- Direct Chemistry Reduction,
- Tabulated Chemistry,
- Optimized Global Chemistry.

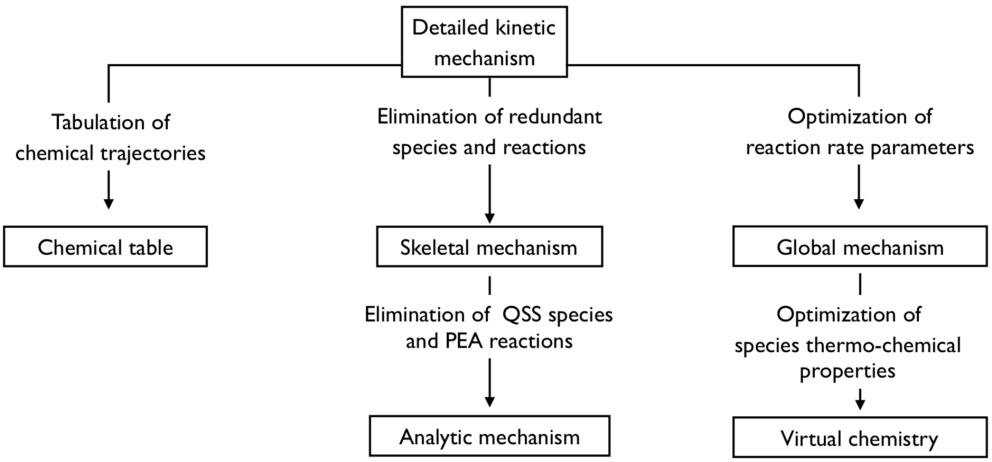

Figure 1.5: *The three major reduced chemistry routes. From Fiorina (2019).*

A brief overview of the three paths is presented in the sub-sections below, organized according to the level of reduction of each methodology. At this point, the intentions are to introduce the techniques used to recover a final reduced kinetic scheme that is reasonably small to be used in LES of combustion system in general, and to make some comments on the application to the gas kinetics employed in soot modeling.

1.2.2.1 Skeletal mechanisms

In the central branch in Fig. 1.5, the kinetic reduction is done systematically. In a first reduction step, the reduced kinetic schemes are derived from the reference detailed kinetic schemes with the intention of decreasing the complexity related to the chemistry solution; *i.e.* the goal is to maintain the main reaction pathways in the detailed scheme, lowering the number of species and reactions and leading to less stiff problems without affecting the reproduction of combustion phenomena (Turányi (1990)). A Skeletal Mechanism (SM) is then obtained after this process. Examples of skeletal reduction techniques comprise:

- Sensitivity Analysis methods: here, a Jacobian matrix analyisis or a sensitivity analysis are used to measure the interaction between species and

identify the redundant species (Tomlin et al. (1992); Turányi and Bérces (1990); Vlachos (1996); Brown et al. (1997)).

- Directed Relation Graph (DRG) methods: in this category the degree of coupling and dependency between species is mapped, where non-essential species detected presents a weak link to the relevant ones (Lu and Law (2005); Pepiot and Pitsch (2005); Pepiot-Desjardins and Pitsch (2008); Pepiot (2008); Jaravel et al. (2017))
- Optimization-Based Skeletal Reduction: this time the reduced mechanism correspond to the set of species and reactions that best reproduce some target flame properties, by using an optimization algorithm (Sikalo et al. (2014); Chang et al. (2018)).

Skeletal mechanisms are still too large to be used in LES of practical simulations, limited only to laminar flames calculations.

1.2.2.2 Analytically reduced chemistry

An Analytically Reduced Chemistry (ARC) is conceived by dissociating the fast species and reactions and controlling the slow ones in a Skeletal Mechanism (SM); decreasing even more the number of species and stiffness of the chemical system.
Two strategies based on time scale analysis predominate in the literature for the supplemental reduction: Partial-Equilibrium Approximation (PEA) and, the most preferred, Quasi Steady State Approximation (QSSA) (Goussis and Maas (2011); Lu and Law (2006); Goussis (2012)) . Quasi Steady State (QSS) species identification could be performed automatically by analysis of species production rates (Lepage (2000); Chen (1997); Montgomery et al. (2006)), by looking the time-scale involved in reactive mixtures (Lam and Goussis (1994); Lu and Law (2008); Felden et al. (2018)) or through optimization algorithms (Montgomery et al. (2006)). Consequently, ARCs present a significant reduction in the number of species and reactions and the stiffness of reaction rates.
Examples of automated tools to generate ARCs found in the literature include:

- YARC tool; where methods such as DRG with error propagation (or DRGEP, Pepiot (2008)) and Level of Importance (LOI, Løvås et al. (2002)) are applied (Felden et al. (2018); Felden et al. (2018); Gallen (2020)). In DRGEP the error is damped as it propagates along the graph. The LOI method combines lifetime and species sensitivity.
- Optimized Reduced Chemistry (ORCh); where identification of chemical trajectories in the target configurations along with the traditional techniques of SM and ARC and optimization of reaction rates are performed (Jaouen et al. (2017)).

The pros of using an ARC are that it reproduces very well the flame properties at a considerably low cost, particularly in laminar flames. LES in turbulent configurations is still limited since the automatization of the method and the technology capable to run such mechanism are available just recently, but at

the end, with a favorable outcome (Jaravel et al. (2017); Felden et al. (2018); Felden et al. (2018); Gallen et al. (2019)). The reduction process shows some limitations in the reproduction of chemical trajectories after the removal (or QSS assumptions) of certain species and reactions. In this regard, the ORCh method has the advantage to retrieve the missing characteristics through the optimization process, leading to a better prediction of chemical species, auto-ignition or quenching points, etc., compared to the detailed mechanism solutions.
The cons of using ARC or ORCh in LES reside primarily in the size of the resulting kinetic scheme, which is still large compared to other reduction techniques, which are presented later. This ultimately leads to having short chemical time scales to solve for in the combustion system, especially for minor species (pollutants), which introduces the need of additional modeling hypotheses for the turbulence-chemistry interactions.
An example of ARC for soot precursors prediction (naphthalene and pyrene) was proposed by Gallen (2020). This model was validated using 1-D unstretched premixed flames, showing excellent agreement with results using the reference detailed mechanism. Discrepancies were observed, however, in a burner-stabilized flame configuration (Gallen (2020)). These reveal the existence of missing chemical trajectories during the reduction process, which are rather activated in the second configuration.

1.2.2.3 Tabulated chemistry

The second branch in Fig. 1.5 concerns Tabulated Chemistry. Traditionally, solutions to canonical combustion configurations are established *a priori* using a detailed mechanism and are stored in a discretized look-up table. These solutions contain a wide range of thermochemical states representative of a target combustion system. The table is parametrized by a reduced set of thermochemical variables that have access to the state space (or thermochemical trajectories) previously defined. The system of equations for the CFD computation are then translated in terms of the reduced set of variables and goes from N_s species in the original detailed mechanism to normally $n \ll N_s$ variables (or state coordinates) in the new system.
A well known method is the Intrinsic Low-Dimensional Manifold (or ILDM for short). ILDM is a mathematical technique developed by Maas and Pope (1992a) and Maas and Pope (1992b), where the so-called low-dimensional manifold which attracts all chemistry trajectories is identified by analyzing homogeneous adiabatic 0-D reactors. Time scales are determined through the Jacobian matrix associated to the system, and depending on the chosen criteria, the slow time scales determine the reduced chemistry (slow manifold). Having ILDM foundations established, Gicquel et al. (2000) with FPI (Flame Prolongation of ILDM) and Van Oijen et al. (2001) with FGM (Flamelet-Generated Manifold) have proposed to construct the manifolds from 1-D laminar premixed flames,

showing potential to recreate premixed and weakly stratified flame structures (Fiorina et al. (2015)).

The Flamelet Model includes a physical hypothesis throughout the chemical database design: it assumes that a turbulent flame front can be decomposed in a collection of 1-D flame elements (Poinsot and Veynante (2012)). In the Flamelet Model, developed by Peters (1984) and Bradley et al. (1988), the look-up table was parametrized by the mixture fraction and the scalar dissipation rate of the mixture fraction. In turbulent non-premixed flames, the chemical structure is well approximated by placing steady counterflow diffusion flames (or flamelets) in the look-up table. Additional examples of tabulated models can be found in Pierce and Moin (2004), Fiorina et al. (2005), Franzelli et al. (2013), Ihme and Pitsch (2008), Chatelier et al. (2019).

The tabulation technique developed by Ihme and Pitsch (2008), called Radiation Flamelet/Progress Variable model (RFPV), was applied to the gas-phase kinetics in sooting flames in numerous occasions. Here, enthalpy defect is taken into consideration because of radiation heat losses, a typical feature in sooting flames. Rodrigues (2018) applied this method in non-premixed ethylene-air sooting flames and the tabulation was parametrized by the mixture fraction, a non-dimensional progress variable, a segregation factor (for the turbulence model) and a non-dimensional enthalpy factor. An example of the RFPV model from Rodrigues work, showing the impact of the enthalpy defect in the temperature and progress variable for a given strain rate is shown in Fig. 1.6, where Z is the mixture fraction, Y_C the progress variable and Φ is the enthalpy parameter. In section 1.4 it will be shown that most of authors found in the literature use this method in LES of sooting flames.

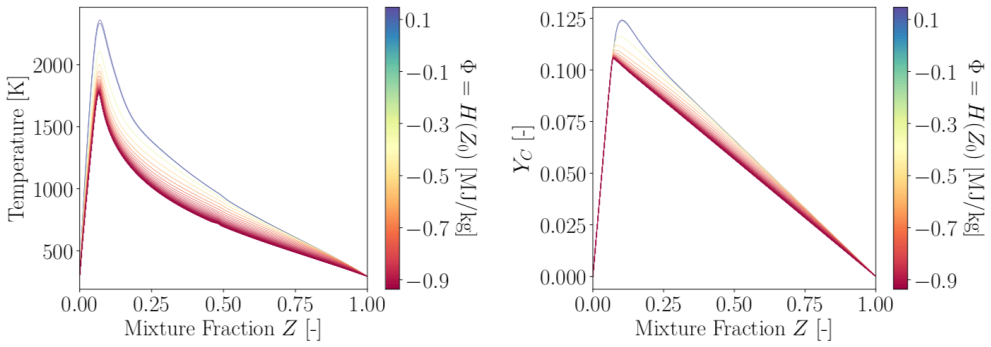

(a) Temperature T (b) Progress variable Y_C

Figure 1.6: *Impact of enthalpy defect on the profiles of (a) temperature and (b) progress variable for a given strain rate $a = 0.15s^{-1}$ variable. Extracted from Rodrigues (2018).*

The principal advantage of this method is a very low CPU cost, because just a few variables are transported and; computing the source terms of the species processing resource are saved, since every quantity is pre-calculated and saved

in the look-up table.
The limitations are related to situations where complex flame regimes are not identified, and combining multiple combustion regimes can make the look-up table generation an extremely difficult task, since several flame archetypes should be considered and it would require further modeling assumptions (Lamouroux et al. (2014); Chatelier et al. (2019)).

1.2.2.4 Optimized global chemistry

A reactive system can also be represented by using global mechanisms, the third branch in Fig. 1.5. An optimized global scheme is typically composed of two to four global reactions. It was firstly introduced in the work of Westbrook and Dryer (1981) and a few years later followed by Jones and Lindstedt (1988). In this classification, kinetic parameters are usually optimized to reach sufficiently accurate results in premixed flames. Primarily, flame characteristics such as fast fuel decomposition and slow oxidation of intermediate species are foreseen. Besides, adiabatic equilibrium condition is achieved by adding a sufficient number of species. Finally, the global system is able to reproduce laminar flame speed and thermodynamical equilibrium states for a very limited number of operating conditions, from lean to reasonably rich flames; and also diffusion flames.
Historically, the determination of reaction rate parameters were done either empirically or systematically. For example, Jones and Lindstedt (1988) employed arbitrary values of reaction rates; while Fernandez-Tarrazo et al. (2006), in a one-step global mechanism, and Franzelli et al. (2010), in a two-step global mechanism, have proposed innovative techniques of reaction rates determination in order to capture particular flame characteristics, *e.g.* by tabulating correction functions as a function of the composition. An advanced original methodology to obtain the kinetic parameters was introduced by Polifke et al. (1998), where a genetic algorithm is used to determine them automatically instead of identify them randomly or by instinct. In these global approaches, pollutant species and accurate inner flame structure description are generally out of reach (Franzelli et al. (2013)).
A more recent approach of global optimized chemistry is the so-called Virtual Chemistry and was introduced by Cailler et al. (2017). The virtual chemistry method considers a few optimized virtual species and virtual reactions that mimic a real combustion system in a wide range of operating conditions and configurations. First of all, the construction of the virtual scheme is made from scratch by adding to it some virtual species and virtual reactions, unlike typical reduction methods where species and reactions are dispensed with. And second, through a genetic algorithm an optimization is performed to get: *i*) the thermodynamic properties of the virtual species, and *ii*) the chemical reaction rates of the virtual reactions; in order to recover the flame characteristics of the targeted combustion system: temperature profiles, heat release rate, pollutant

formation, etc.
In conclusion, since the global optimized chemistry approach accounts for a small number of species and reactions, it constitutes a very attractive option to solve turbulent reactive flows in LES at a very low CPU cost. In practice, LES works using global mechanism include practical or academic configurations and different combustion regimes (Franzelli et al. (2012); Volpiani et al. (2017); Lancien et al. (2017); Maio et al. (2019)). However, global mechanisms for the gas phase in LES of sooting flames are very rare in the literature: soot precursors are minor species that do not contribute in the development of the flame structure, so these species are completely ignored during the construction of the global mechanism. In an effort to include them, Franzelli et al. (2015) used a hybrid combination of a global chemistry for the flame structure and a tabulated chemistry for soot precursors, a method previously developed in Lecocq et al. (2014). To overcome with these issues, an original approach using virtual chemistry is intended in this thesis and a preliminary discussion of this concept is made in subsection 1.6.

1.3 Solid-phase modeling

Once the gas-phase is determined in the reactive flow solver, the next step is to solve the solid phase. First of all, a transition model from the gas-phase to the solid-phase is needed, *i.e.* the coupling of the gas-phase solver to the solid-phase solver should be established. For this purpose, the relevant characteristics of the solid-phase must be defined, especially those involving a gas-solid retroaction. Then, the problem of the solid-phase is divided into two parts: the dynamics of the particles and the reactivity of the soot surface with the gas-phase. In this section, a detailed model is first introduced for each part, allowing the respective simplifications to be derived.
Soot particles are characterized by their total number N_{soot} and their total mass M_{soot}. Soot density will henceforth be considered constant with $\rho_s = 1.8 \cdot 10^3$ kg.m^{-3}. The relationship linking the total mass M_{soot} and the total volume of these particules V_{soot} is:

$$M_{soot} = \rho_s V_{soot}. \tag{1.1}$$

It is more suitable to work with the equivalent quantities of interest per unit volume. They are the particles number density N_s and the soot volume fraction f_v. Thus, considering a domain V:

$$\begin{cases} N_{soot} = \displaystyle\int_V N_s dV; \\ V_{soot} = \displaystyle\int_V f_v dV. \end{cases} \tag{1.2}$$

In order to have a good fidelity in soot evolution behavior, and since most phenomena are associated to the soot particle size, it is necessary to have

access to the soot particles size distribution (PSD). The complexity of soot particles structure requires many variables to describe it (*e.g.* volume, surface, diameter, etc.), but for the sake of simplicity only volume v will be considered (*i.e.* mono-variate description). The two following quantities are introduced for the purpose: *i*) the number density function (NDF), $n(v)$, or the number of soot particles over the volume space v depicted by soot particles; and *ii*) the soot volume fraction distribution $q(v)$ over the volume space v. So in that way, N_s and f_v are calculated by:

$$\begin{cases} N_s = \int_0^{+\infty} n(v)dv; \\ f_v = \int_0^{+\infty} q(v)dv; \end{cases} \tag{1.3}$$

where the relationship between $n(v)$ and $q(v)$ is:

$$n(v) = q(v)/v \tag{1.4}$$

A population of soot particles carried by the gas-phase is represented statistically by an NDF that depends on time, spatial position and one or several internal variables, *e.g.* the size of soot particles: volume, surface area, etc. (Ramkrishna and Singh (2014)). In particle dynamics, the NDF $n(v)$ follows the Population Balance Equation (PBE) governing its temporal and spatial evolution through the following transport equation:

$$\frac{\partial n}{\partial t} + \nabla \cdot ((\mathbf{u} + \mathbf{v_T})n) = \nabla \cdot (D_s \nabla n) + \dot{n}_s; \tag{1.5}$$

where:

- $\mathbf{u}$ is the particle velocity.
- $\mathbf{v_T}$ is the thermophoretic velocity and is expressed as:

  $$\mathbf{v_T} = -0.554\nu\frac{\nabla T}{T}. \tag{1.6}$$

  Here, ν is the gas kinematic viscosity and T the temperature. For soot, $\mathbf{v_T}$ is opposed to the temperature gradient and consequently particles are transported from hot regions towards low temperature ones (Waldmann and Schmitt (1966); Derjaguin et al. (1966)). This phenomenon is not negligible when a strong gradient of temperature takes place.
- D_s is the soot particles diffusion coefficient. For example in Epstein (1924), D_s is estimated by:

  $$D_s = \frac{3}{2\rho}\left(1 + \frac{\alpha_T \pi}{8}\right)^{-1} \frac{1}{d^2}\sqrt{\frac{W_{gas} k_b T}{2\pi N_A}}. \tag{1.7}$$

  Here, $\rho = NW_{gas}/N_A$; with N the gas number density, W_{gas} the gas molar weight and N_A the Avogadro's number. Also, $\alpha_T = 0.9$ (Waldmann

and Schmitt (1966); Blanquart and Pitsch (2009); Yapp et al. (2015)) is the thermal accomodation factor expressing the fraction of heat flux exchanged between the particle surface and the surrounding gas molecules; d the soot particle diameter and k_b the Boltzmann constant.

- $\dot{n_s}$ is the source term of number density function $n(v)$. It accounts for soot particles dynamics and soot surface reactivity with the gaseous phase.

The source term $\dot{n_s}$ of the PBE is decomposed as:

$$\dot{n_s} = \dot{n}_c(v) + \dot{n}_{sr}(v). \tag{1.8}$$

The first term $\dot{n}_c(v)$ is due to soot particle collisions and constitutes the effects of nucleation, condensation and coalescence. The second term $\dot{n}_{sr}(v)$ concerns the surface reactivity of soot particles with the gas-phase and describes the impact of surface growth and oxidation. The models for soot particles dynamics and soot surface reactivity are described mathematically in the following subsections.

1.3.1 Soot particles dynamics mathematical representation

Particle collision, in the ideal case of spherical particles before and after collision, can be described by the Smoluchowski equation (Smoluchowski (1916)). This expresses the gain $\dot{n}_c(v)$ of volume distribution of particles number density due to particle collisions, described by:

$$\dot{n}_c(v) = \frac{1}{2}\int_0^v \beta_{v-u,u} n(u) n(v-u) du - \int_0^\infty \beta_{v,u} n(u) n(v) du; \tag{1.9}$$

where $\beta_{v,u}$ represents the collision frequencies of the particles of size v with all other particles of any size u. Then, several types of particles have to be considered:

- both in the gaseous state (dimers) for nucleation,
- one in the gaseous state (dimer) and the other in the solid state for condensation,
- both in the solid state for coagulation.

The collision frequency depends on the Knudsen number Kn_u of the considered particles, which is:

$$\mathrm{Kn}_u = \frac{2\lambda_{gas}}{d_u}; \tag{1.10}$$

here, d_u is the diameter of the particle of size u and λ_{gas} is the gas mean free path, written as:

$$\lambda_{gas} = \frac{RT}{\pi\sqrt{2} d_{gas}^2 N_A P}; \tag{1.11}$$

where R is the perfect gas constant, T the temperature, N_A the Avogadro number, P the pressure and d_{gas} the diameter of a gas particle.
Three regimes exist according to the value of Kn_u (Kazakov and Frenklach (1998)). If the pressure is sufficiently low, the particles are small enough relative or thermal agitation is low (corresponding to $\mathrm{Kn}_u > 10$), the regime is considered as "molecular". Then:

$$\beta_{u,v} = \beta^{fm}_{u,v} = \epsilon_{u,v} \left(\frac{3}{4\pi}\right)^{1/6} \sqrt{\frac{6k_bT}{\rho_s}} \sqrt{\frac{1}{u} + \frac{1}{v}} \left(u^{1/3} + v^{1/3}\right)^2; \tag{1.12}$$

with:

- k_b the Boltzmann constant,
- ρ_s the soot particles mass density,
- T the temperature,
- u and v volumes of colliding particules,
- $\epsilon_{u,v}$ an amplification factor taking into account the interactions between particles (Van der Waals interactions). Its value depends on the considered soot particles collision phenomena (Alam (1987); Pailthorpe and Russel (1982)). According to the work of Marchal (2008), it is $\epsilon_{u,v} = 2.5$ for nucleation, $\epsilon_{u,v} = 1.3$ for condensation and $\epsilon_{u,v} = 2.2$ for coagulation.

If the pressure is sufficiently high, or the particles are large enough, or thermal agitation is important ($\mathrm{Kn}_u < 0.1$), the collision regime is "continuous". Hence:

$$\beta_{u,v} = \beta^{c}_{u,v} = \frac{2k_bT}{3\mu} \left(u^{1/3} + v^{1/3}\right) \left(\frac{\mathrm{Cu}_u}{u^{1/3}} + \frac{\mathrm{Cu}_v}{v^{1/3}}\right); \tag{1.13}$$

with $\mu = \frac{C_1 T^{3/2}}{T + C2}$ the dynamic gas viscosity and $\mathrm{Cu}_u = 1 + 1.257\mathrm{Kn}_u$ the corrective Cunningham coefficient for a particle of size u.
In the transition of previous cases ($0.1 < \mathrm{Kn}_u < 10$), the collisional regime is called "intermediate". Then, the collision frequency is calculated by the harmonic mean of the free molecular and continuous collision frequencies:

$$\beta_{u,v} = \beta^{tr}_{u,v} = \frac{\beta^{fm}_{u,v}\beta^{c}_{u,v}}{\beta^{fm}_{u,v} + \beta^{c}_{u,v}}. \tag{1.14}$$

Figure 1.7 shows an example of the evolution of collision frequencies $\beta/4K$ with the Knudsen number Kn (Kazakov and Frenklach (1998)) for the three collisional regimes of Eqs. 1.12 to 1.14. Equal-size soot particles are considered at a pressure of 10 bar and temperature of 1800 K. Also, $K = (2k_BT)/(3\mu)$. For further details, see Kazakov and Frenklach (1998).

1.3.2 Soot particle surface reactions

As previously mentioned, oxidation and surface growth are two major effects coming from gas-phase interaction with the surface of soot particles.

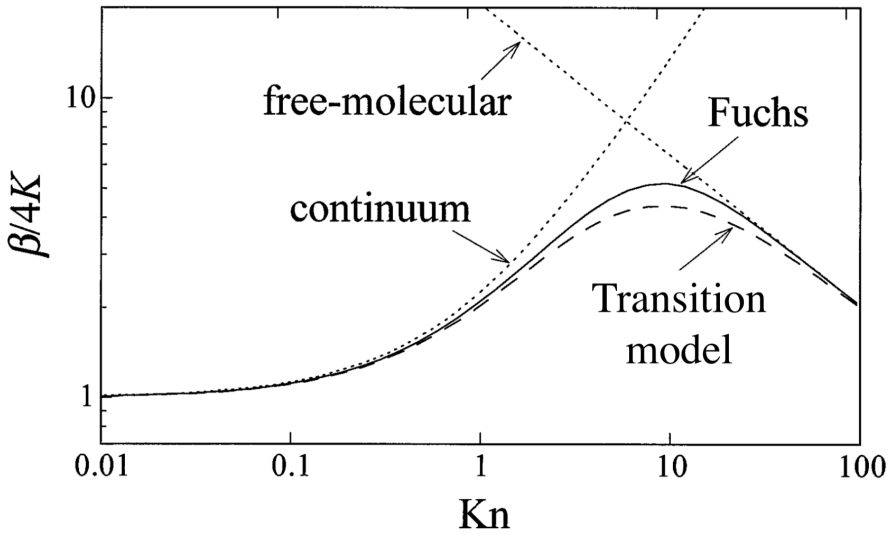

Figure 1.7: *Collision frequencies evolution with Knudsen number for equal-sized soot particles at 10 bar and at 1800 K. Extracted from Kazakov and Frenklach (1998).*

Both phenomena are typically modeled by using the *HACA-RC* (Hydrogen-Abstraction-C_2H_2-Addition - Ring-Closure) mechanism described in Mauss et al. (1994), which is a modification of the HACA mechanism developed by Frenklach and Wang (1994) and presented as well for PAHs in section 1.1. Frenklach and Wang (1994) basically proposed an analogy between chemical reactions taking place on PAHs and those occurring on the surface of soot particles. The chemical pathways involved in the mechanism of soot surface growth and oxidation are then supposed to be similar to the HACA mechanism used generally for the PAHs evolution modeling.

Table 1.1 presents the reactions and Arrhenius law parameters of the HACA-RC mechanism proposed by Mauss et al. (1994). Given the soot particle $C_{n_C}H$ with n_C carbon atoms and $C^*_{n_C}$ the associated radical, the latter is first created by the attraction of a hydrogen atom at the surface of the soot particle by another hydrogen atom (reaction **1**) or an OH radical (reaction **2**) and the radical consuming influence of H_2O. Reaction **3** is the associated reversible deactivation reaction, which accounts for limitation of surface growth at high temperatures.

Acetylene C_2H_2 is basically responsible for surface growth (same as for PAH species). It reacts at the surface of a soot particle radical $C^*_{n_C}$ via reactions **4** and **5**. Reactions **6** and **7** represent the oxidation of soot particle due to the presence of O_2 and OH molecules (Frenklach and Wang (1994); Wang et al. (1996); Siegla et al. (1981); El-Leathy et al. (2002); Xu et al. (2003)).

Kinetic parameters of the Arrenhius laws are from Mauss et al. (2006) and the oxidation reaction rate by OH molecules (reaction **7**) has been updated from Siegla et al. (1981); El-Leathy et al. (2002); Xu et al. (2003).

Num.	Reaction	k	A	β	E_a [kJ/mol]
1	$C_{n_C}H + H \underset{k_{1b}}{\overset{k_{1f}}{\longleftrightarrow}} C^*_{n_C} + H_2$	k_{1f}	$1.000 \cdot 10^{14}$	0.0	0.0
		k_{1b}	$1.439 \cdot 10^{13}$	0.0	−37.63
2	$C_{n_C}H + OH \underset{k_{2b}}{\overset{k_{2f}}{\longleftrightarrow}} C^*_{n_C} + H_2O$	k_{2f}	$1.630 \cdot 10^{8}$	1.4	6.10
		k_{2b}	$1.101 \cdot 10^{8}$	1.4	31.14
3	$C^*_{n_C} + H \underset{k_{3b}}{\overset{k_{3f}}{\longleftrightarrow}} C_{n_C}H$	k_{3f}	$1.000 \cdot 10^{13}$	0.0	0.0
		k_{3b}	0.000	0.0	0.0
4	$C^*_{n_C} + C_2H_2 \underset{k_{4b}}{\overset{k_{4f}}{\longleftrightarrow}} C^*_{n_C}C_2H_2$	k_{4f}	$3.500 \cdot 10^{13}$	0.0	0.0
		k_{4b}	$3.225 \cdot 10^{14}$	0.0	181.69
5	$C^*_{n_C}C_2H_2 \underset{k_{5b}}{\overset{k_{5f}}{\longleftrightarrow}} C_{n_C+2}H + H$	k_{5f}	$1.000 \cdot 10^{10}$	0.0	20.0
		k_{5b}	$8.770 \cdot 10^{11}$	0.0	74.44
6	$C^*_{n_C} + O_2 \xrightarrow{k_{6f}} C^*_{n_C-2} + 2CO$	k_{6f}	$1.000 \cdot 10^{12}$	0.0	8.4
6'	$C^*_{n_C}C_2H_2 + O_2 \xrightarrow{k_{6'f}} C^*_{n_C} + 2HCO$	$k_{6'f}$	$1.000 \cdot 10^{12}$	0.0	8.4
7	$C_{n_C}H + OH \xrightarrow{k_{7f}} C^*_{n_C-2} + CH + HCO$	k_{7f}	Efficiency: $\gamma_{OH} = 0.13$		

Table 1.1: *HACA-RC mechanism for soot surface reactivity.*

1.3.3 Soot evolution numerical models

In soot modeling for numerical combustion, challenges are to model both the contributions of the gas phase reactivity and the solid particle dynamics description. Because the number of fine particles is so large, a statistical approach is used to describe the fine-particle population (Raman and Fox (2016)). The complexity of the different soot formation phenomena suggests to develop simplified numerical models, in order to reduce the calculation cost.
In this subsection, sorted by the computational cost of the methodology, the numerical models to describe soot evolution that are found in literature will be presented: Lagrangian models, aerosol or chemical discrete sectional models, method of moments and empirical & semi-empirical models. Of these models, the general principle as well as the advantages and disadvantages are reported. An overview of all methodologies used in LES of turbulent flames found in the literature is made, followed by a discussion on the virtual chemistry concept in this subject. A final conclusion and the chosen soot model used for the detailed chemistry database (*cf.* chapter 3) is deliberated.

1.3.3.1 Lagrangian methods

In Lagrangian methods, soot particles are treated like droplets in a two-phase flow computations: soot particles are handled as fictitious point source Lagrangian particles and are monitored separately.
As a first detailed approach, Monte Carlo-based models provide accurate results by tracking the evolution of number density through an assemble of particles governed by stochastic processes (Balthasar and Kraft (2003)). Any assumption on the PSD shape can be overcome by applying Monte Carlo techniques to

obtain a solution of soot population balance (Mitchell and Frenklach (1998); Balthasar and Kraft (2003); Celnik et al. (2007); Bouaniche et al. (2020)). Soot particles are represented by a discrete list of particles and their evolution is solved by an explicit Monte Carlo approach. However, due to its very high cost and number of shots required for convergence, this methodology is not suitable for complex practical configurations and their applicability has been limited to simple configurations, such as 0-D reactors (Celnik et al. (2007)). Nonetheless, the Monte Carlo technique is usually adopted to validate the performance of other models for PSD prediction, such as Sectional Methods or Method of Moments in academic configurations. Solutions can be considered as reference in soot PBE modeling.
A way to decrease the CPU time is to consider the Langrangian Soot Tracking (LST) method (Gallen (2020)), where numerical particles are tracked similar to the two-phase Lagrangian methods. In LST method, however, one numerical particle mimics similar behavior of a group of physical particles (Gallen (2020)). Thus, the calculation time is reduced by computing a small number of numerical particles in a control volume, which are representative of a larger number of physical particles present in the same domain (Gallen et al. (2019)). This method has been used to investigate soot transport in many combustion applications (Mahmood et al. (2012); Zuber et al. (2015); Ong et al. (2018); Gallen et al. (2019); Dellinger et al. (2020)).
In general, the advantages of the lagrangian method include:

- No assumption in NDF or PSD shape is made;
- NDF or PSD with two variables are possible (usually volume and surface), *i.e.* a bi-variate description;
- Detailed physico-chemical description of soot processes can be taken into consideration;

Main drawbacks are:

- Coupling to the gas phase kinetics may require particular numerical methods and not easy to implement, *e.g.* splitting operators (Celnik et al. (2007));
- Parallelization of the Lagrangian solver is difficult;
- A large number of shots are needed to generate statistics and numerical convergence implicates very high CPU cost.

1.3.3.2 Aerosol discrete sectional models (ADSM)

The sectional model (SM) is an extensively utilized alternative to solve the soot PBE (Smooke et al. (1999); Zhang et al. (2009); Rodrigues et al. (2018); Yan et al. (2019); Blacha et al. (2012); Eberle et al. (2017)). This method relies on the discretization of the PSD or NDF into a finite number of classes or sections with adjacent size limits Gelbard and Seinfeld (1980). Netzell et al. (2007) have proposed a power law description of the volume space hold by the i^{th} section. For $N_{sections}$ sections and denoting v_{MIN} and v_{MIN} for the smallest

and biggest soot particles, respectively; the i^{th} section verifies that:

$$v_i^{max} = v_{\text{MIN}} \left(\frac{v_{\text{MAX}}}{v_{\text{MIN}}} \right)^{i/N_{sections}} \; ; \text{ for } i = 1 \text{ to } N_{sections} \tag{1.15}$$

where v_i^{max} is the size upper limit of the i^{th} section. This mono-variate formulation of the soot PSD is solved by using one or several moments for the i^{th} section. The transition from gas to solid phase could be described in the sectional method because gas-phase flow, gas-phase kinetics and soot sections are solved simultaneously (Eberle et al. (2017)).
The advantages of the sectional methods are:

- Detailed physico-chemical description of soot processes can be taken into consideration;
- Morphology features can be incorporated in the mono-variate NDF description, *e.g.* using a surface-volume relationship depending on size (as in Rodrigues et al. (2018)).

The drawbacks are:

- The method could be very cpu-consuming and considered mostly unaffordable if a bi-variate surface-volume description of the PSD or NDF is considered;
- The numerical accuracy depends on the number of sections considered and usually it demands a minimum of 20 sections to achieve it (in a mono-variate description), resulting very expensive simulations.

1.3.3.3 Chemical discrete sectional models (CDSM)

Pope and Howard (1997) introduced the aerosol dynamics of the discrete sectional approach modeled as a reaction with Arrhenius-like reaction rate closure. Following their size distribution, soot particles are then gathered into classes or sections of lumped pseudo-species called BINs. Then, BINs are considered as gaseous chemical species and their evolution is solved together with other chemical species of the detailed kinetics mechanism. The soot formalism is based on a sectional method.
The most visible difference between CDSM and ADSM is that CDSM considers each soot section inside the gas-phase kinetic mechanism and to be part the of gas-phase equation system, *i.e.* the PBE is translated to a species transport equation, and therefore soot sections (BINs) contribute to mass conservation in the gas-phase. Each source term in the BINs transport equations has an Arrhenius closure and their values derived from reference reactions (usually reactions involving PAHs). For example, models of aggregation source term are usually derived from Smoluchowski's equation 1.9 using particle dynamics, but Saggese et al. (2015) proposed for this purpose the following reaction:

$$\text{BIN}_i + \text{BIN}_n \rightarrow products \; ; \; \text{with}: i, n \geq 13; \tag{1.16}$$

where the rate constants are set in the same way of PAH addition to soot surface, *i.e.* activation energy is set to zero while pre-exponential factor is multiplied by a correlated collision efficiency (Saggese et al. (2015)). For soot surface reactivity, *e.g.* oxidation, reactions are similar to those found in the HACA mechanism for PAHs, one of them considered by Saggese et al. (2015) is:

$$O_2 + \mathrm{BIN}_i^* \rightarrow products + CO + HCO^*; \text{ with: } 5 \leq i \leq 20; \tag{1.17}$$

where the reference reaction is:

$$O_2 + C_{10}H_7^* \rightarrow C_8H_6^* + CO + HCO^* \tag{1.18}$$

from Frenklach (2002b). So each BIN in the kinetic mechanism has a set of similar reactions accounting for all soot formation phenomena, leading to very large detailed mechanism.
Richter et al. (2005) proposed a kinetic scheme with 295 species and 6654 reactions, where 5552 reactions corresponded to soot growth of 20 BINs. Each BIN has only one single and decreasing H/C ratio from 0.5 in the first section to 0.125 in the last section. Later, D'Anna and Kent (2008) followed the same approach considering 26 BINs with a constant H/C ratio about 0.8. Further developments have been done to consider different H/C ratio ranges (Sirignano et al. (2010)) and an additional dimension to account different morphologies (Sirignano et al. (2013)).
CRECK Modeling Group at Politecnico di Milano is another research group that is constantly developing soot formation mechanisms. The CRECK mechanism from Saggese et al. (2015) consists of 16797 reactions and 297 species, including 20 BINs. BIN_1 through BIN_4 correspond to heavy PAHs with 20, 40, 80 and 160 carbon atoms respectively. The nascent soot particles are classified as BIN_5 and they grow from spherical shape (BIN_5 to BIN_{11}) until they take an aggregate form (BIN_{12} to BIN_{20}) (Saggese et al. (2015)). Recently, Pejpichestakul (2019) proposed an updated version of the detailed kinetic mechanism extending the H/C discretization and combining approaches from the previous mentioned studies reaching a total of 22290 reactions and 452 species, including 25 sections. The model was extensively validated in 1-D and 2-D laminar flames (Sirignano et al. (2013); Saggese et al. (2015); Pejpichestakul et al. (2019); Pejpichestakul et al. (2019)).
The main advantages are:

- Access to the PSD or NDF evolution is possible;
- Detailed description of the physico-chemical phenomena and interactions with the gaseous phase can easily be dealt with.

The main disadvantages are:

- The method is very expensive due too elevated number of species and reactions involved in the kinetic mechanism;
- The PSD is generally mono-variate with volume as internal variable. However, morphology could be taken care by establishing a volume-surface

relationship depending on the soot particle size (Sirignano et al. (2013); Saggese et al. (2015); Pejpichestakul et al. (2019); Pejpichestakul et al. (2019)) or using a post-processing tool to predict primary soot particle size (Bodor et al. (2019)).

1.3.3.4 Method of moments

The statistics of a population of soot particles are incorporated in the NDF. The Method of Moments (MOM) solves a set of moments transport equations associated to the PBE (*cf.* equation 1.5) and continuously reconstructs the NDF evolution (Frenklach and Harris (1987); Marchisio and Fox (2005); Blanquart and Pitsch (2007); Mueller et al. (2009b); Yuan et al. (2012); Madadi-Kandjani and Passalacqua (2015); Salenbauch et al. (2015); Nguyen et al. (2016); Selvaraj et al. (2016); Salenbauch et al. (2019)). A moment can be defined as mono-variate or multi-variate depending on the number of the internal variables considered in the NDF, which will describe the complexity of the structure of soot particles (morphology).
For a NDF $n(v)$, *i.e.* the soot particle volume v as the internal variable, the mono-variate definition of a moment of order k, is written as:

$$m_k = \int_{v=0}^{+\infty} v^k n(v) dv. \tag{1.19}$$

However, for a bi-variate NDF $n(v,s)$, the bi-variate moment of k^{th} order in volume v and l^{th} order in surface area s is:

$$m_{k,\,l} = \int_{v=0}^{+\infty} \int_{s=0}^{+\infty} v^k s^l n(v,s) dv ds. \tag{1.20}$$

The system of moment balance equations is then obtained by applying equations 1.19 or 1.20 to the PBE (*cf.* equation 1.5).
A few low-order moments in equation 1.20 correspond to known physical quantities: $m_{0,0}$ is the particle number density N_s (*cf.* equation 1.3); $m_{1,0}$ is the soot volume fraction f_v (combining equations 1.3 and 1.4); and $m_{0,1}$ represents a quantity of soot surface area per unit of volume.
Essentially, having all the moments for $(k,l) \in [0,+\infty[\times[0,+\infty[$ is equivalent to having the NDF (Frenklach (2002b)). In practice, however, only first orders of moments are solved to avoid modeling closure issues and to limit CPU cost (usually does not exceeds 10 moments).
As mentioned before, the transport equations are solved for the considered set of moments and each source term (*cf.* equation 1.8) depends on the gas parameters, moment weights and the closure selected for the moments. Types of numerical closures include: interpolative closure (MOMIC) (Frenklach and Harris (1987); Frenklach (2002a); Selvaraj et al. (2016)), quadrature methods (Marchisio and Fox (2005),Yuan et al. (2012); Madadi-Kandjani and Passalacqua (2015); Salenbauch et al. (2015); Nguyen et al. (2016); Salenbauch

et al. (2019)) or even combining both previous methods (hybrid) (Mueller et al. (2009b)). It is expected then to achieve low computational cost compared to stochastic or sectional methods.
One could select a MOM since it is based on a detailed description of the different physical and chemical phenomena and it permits to describe soot particle complex structure (morphology) by considering one or more internal variables; all at a low computational cost comparing to other methods. Nevertheless, the drawbacks include the complexity of mathematical requirements to model the closures of moment source terms; normally the number of moments needed are higher than the number of moment source terms to close. Also, it does not provide direct access to the PSD and its reconstruction could be expensive or have other numerical difficulties, or even not being possible.

1.3.3.5 Empirical & semi-empirical models

Methods in this classification are in general based on empirical or ad-hoc formulation of soot formation processes and simple transport equations (Tesner et al. (1971); Moss et al. (1989); Kennedy et al. (1990); Said et al. (1997); Zhubrin (2009); Leung et al. (1991); Brookes and Moss (1999)). Typically, two transport equations are considered in order to describe soot particles evolution in terms of mass and/or number density.
For instance, the method of Tesner et al. (1971) was developed from soot particles measurements in laminar hydrocarbon/hydrogen flames and considered the following system of two equations:

$$\begin{cases} \dfrac{d\gamma}{dt} = \gamma_0 + (f-g)\gamma - g_0 N_s \gamma; \\ \dfrac{dN_s}{dt} = (a - bN_s)\gamma; \end{cases} \tag{1.21}$$

where, the concentration of actives sites γ associated with soot particles formation process and the concentration of soot particles N_s are transported. Also, a, b, $f-g$, g_0 are empirical coefficients and $\gamma_0 = \Gamma_0 . \exp(E_a/RT)$ is the spontaneous production rate of active particles which depends on temperature through an Arrhenius law. It was shown that by fixing values of the empirical constants and adjusting the value of Γ_0 and activation energy E_a, the model was able to retrieve the soot evolution in laminar coflow diffusion flames. This model was eventually extended to consider for the C/H ratio of the burning hydrocarbon (Magnussen (1989)) and also adjusted for turbulent flame applications (Lopez-Parra and Turan (2007)), where a reasonable agreement with experimental data was obtained using a single-step kinetic mechanism, but still only valid for the very specific case.
A semi-empirical method was introduced by Leung et al. (1991), and then improved by Lindstedt (1994) and Lindstedt and Louloudi (2005), where the particles number density N_s and the soot mass fraction Y_s are transported in

the following system:

$$\begin{aligned}
&\frac{\partial \rho N_s}{\partial t} + \nabla \cdot \left(\rho \left(\mathbf{u} + \mathbf{v_T}\right) N_s\right) = \underbrace{\frac{2}{C_{\min}} N_A k_1(T) \left[C_2H_2\right]}_{\text{nucleation}} \\
&\qquad \underbrace{- 2C_a \left(\frac{6M_C}{\pi \rho_s}\right)^{1/6} \left(\frac{6k_b T}{\rho_s}\right)^{1/2} (\rho N_s)^{11/6} \left(\frac{\rho Y_s}{\rho_s}\right)}_{\text{coagulation}} \\
&\frac{\partial \rho Y_s}{\partial t} + \nabla \cdot \left(\rho \left(\mathbf{u} + \mathbf{v_T}\right) Y_s\right) = \underbrace{k_1(T) \left[C_2H_2\right] W_C}_{\text{nucleation}} \\
&\qquad + \underbrace{k_2(T) W_{C_2H_2} f(S_s) W_C}_{\text{surf. growth}} - \underbrace{\left(k_3(T) \left[O_2\right] + k_4(T) X_{OH}\right) S W_C}_{\text{oxidation}}
\end{aligned} \tag{1.22}$$

where C_a and C_{min} are constants, W_C the molar weight of one carbon atom and $W_{C_2H_2}$ the molar weight of an acetylene molecule. The different k_i correspond to Arrhenius laws constants, where every kinetic parameter is adjusted to the studied case. It considers also the total soot surface area per unit volume S_s. It is assumed a spherical shape of soot particles $S_s = (\rho N_s)\pi d_p^2$; where $d_p = 6/\pi(Y_s/(\rho N_s))^{1/3}$ is the mean soot particle diameter. The function $f(S_s) = \sqrt{S_s}$ is proposed in order to integrate aging effects that can lead to a decay of soot surface reactivity (Leung et al. (1991)).

Evaluating the pros and cons, the principal advantage of these methods is that they imply very low CPU cost. However, the cons are numerous:

- They are not universal: source terms utilize case-depended parameters (adjusted to fit measurements) and for very limited range of operating conditions;
- No access is provided to the PSD or NDF evolution;
- Not capable of describing the morphology of soot particles (volume, surface area).
- Need of soot precursors concentrations, generally derived from a detailed chemistry.

A new semi-empirical three-equation model (SE3eq) was developed by Franzelli et al. (2019), and it can be considered as an upgrade of Leung et al. (1991) two-equation model (SE2eq). It accounts for soot morphology description and three soot global quantities: the soot number density N_s, the soot mass fraction $Y_s = \rho_s f_v/\rho$ and the total soot surface area per unit volume S_s (new feature regarding SE2eq); all three variables follow the transport equation (*cf.* equation 1.5):

$$\frac{\partial \Psi}{\partial t} + \nabla \cdot \left((\mathbf{u} + \mathbf{v_T})\Psi\right) = \dot{\omega}_\Psi; \tag{1.23}$$

which is similar to SE2eq. The source terms $\dot{\omega}_\Psi$ are derived from the sectional method of Rodrigues et al. (2018) considering a mono-disperse NDF $n(v, s) =$

$N_s \delta v_s \delta s_s$; where δ correspond to Dirac's delta function. Mean particle volume and surface are given respectively by $v_s = f_v N_s^{-1}$ and $s_s = S_s N_s^{-1}$. Surface equation is derived from Mueller et al. (2009b). Source terms closures are:

$$\begin{aligned}\frac{\dot{\omega}_{Y_S}}{\rho_s} = &\underbrace{v_{\text{dim}} \beta^{\text{fm}}_{v_{\text{dim}}} N^2_{\text{dim}}}_{\text{nucleation}} + \underbrace{v_{\text{dim}} \beta^{\text{fm}}_{v_{\text{dim}}, v_s} N_{\text{dim}} N_s}_{\text{condensation}} + \underbrace{v_{\text{C}_2} \lambda k_{\text{sg}} s_s N_s}_{\text{surface growth}} \\ &- \underbrace{v_{\text{C}_2} \lambda k_{\text{ox}} s_s N_s}_{\text{surface oxidation}} ;\end{aligned} \tag{1.24}$$

$$\dot{\omega}_{N_s} = \underbrace{\frac{\beta^{\text{fm}}_{v_{\text{dim}}} N^2_{\text{dim}}}{2}}_{\text{nucleation}} - \underbrace{\left(1 - \mathcal{H}\left[v_s - v_{\text{C}_2}\right]\right) \lambda k_{\text{ox}} s_s N_s}_{\text{surface oxidation}} - \underbrace{\frac{\beta_{v_s} N_s^2}{2}}_{\text{coagulation}} ; \tag{1.25}$$

$$\begin{aligned}\dot{\omega}_{S_s} = &\underbrace{(18\pi)^{1/3} \left(v_{\text{dim}}\right)^{2/3} \beta^{\text{fm}}_{v_{\text{dim}}} N^2_{\text{dim}}}_{\text{nucleation}} + \underbrace{\delta s^{\text{frac}}_{v_{\text{dim}}} \beta^{\text{fm}}_{v_{\text{dim}}, v_s} N_{\text{dim}} N_s}_{\text{condensation}} \\ &+ \underbrace{\delta s^{\text{frac}}_{v_{\text{C}_2}} \lambda k_{\text{sg}} s_s N_s}_{\text{surface growth}} - \underbrace{\delta s^{\text{spher}}_{v\text{C}2} \lambda k_{\text{ox}} s_s N_s}_{\text{surface oxidation}} .\end{aligned} \tag{1.26}$$

In these equations, v_{C_2} and v_{dim} are to volume of two carbon atom and a dimer, respectively. $\lambda = 1/s_{C_2}$ is the number of active sites per unit surface, with s_{C_2} the surface of two carbon atoms. Relationships for variations in surface $\delta s_v^{\text{spher}}$ (spherical particles) and δs_v^{frac} (fractal aggregates) come from Mueller et al. (2009b). $\mathcal{H}[v]$ is the Heaviside function. N_{dim} is the number density of nucleation (spherical dimers) using a QSSA from collisions of PAHs (Rodrigues et al. (2018)). Reaction constants k_{sg} and k_{ox} are calculated from HACA-RC mechanism (*cf.* table 1.1) and collision frequencies β_v are similar to those presented in subsection 1.3.1.

In one hand, some advantages are added when using this method:

- Physical and chemical phenomena are considered, adding better description and reliability to results;
- The additional surface equation, compared to other semi-empirical models, guarantees better description of surface reactions;
- Relatively easy to implement in CFD codes;
- PSD could be estimated at low computational cost.

On the other hand, the disadvantages of this method include the necessity of more validation cases on NDF reconstruction and also that the accuracy of the method in highly poly-dispersed NDFs is expected to decrease (Franzelli et al. (2019)).

1.4 Soot modeling in LES of turbulent flames

An overview of works present in the literature for LES of turbulent sooting flames is intended, where the different methodologies used to solve the kinetics

of the gas phase and the formation of soot in the solid phase are discussed. Details about the subgrid models to close filtered PAHs and soot source terms in LES will be debated later in Chapter 4.
The International Sooting Flame (ISF) Workshop proposes a set of laboratory-scale turbulent sooting flames to study soot modeling in LES (ISF5 (2021)). From the list of target flames, studies of LES of three turbulent sooting flame configurations are primarily found in the literature: two jet diffusion flames from Peeters et al. (1994) (Delft Flame III) and from Zhang et al. (2011) (Sandia's piloted non-premixed sooting flame), and a confined pressurized flame from Geigle et al. (2013) (DLR FIRST aircraft combustor); henceforth respectively referred as DF3, SANDIA and FIRST configurations.
Table 1.2 is an illustration of realized combinations of "gas-phase chemistry + soot numerical method" used for modeling turbulent sooting flames within a LES framework. It includes the reference, the models used for gas kinetics and soot formation, and the target configuration the model is applied. Hereinafter, works will be referred by their reference name "RF#" in the first column of table 1.2. Most relevant characteristics in modeling and effects of the combinations on results will be discussed below.

Ref. Name	Reference	Chemistry type	Kinetic model	Soot model	Target
RF1	Mueller and Pitsch (2012a)	Tabulated	RFPV	HMOM	DF3
RF2	Sewerin and Rigopoulos (2018)	Detailed	GRI-1.2	SE2eq	DF3
RF3	Han et al. (2019)	Tabulated/Detailed	RFPV/FTC	HMOM	DF3
RF4	Xuan and Blanquart (2015)	Tabulated	RFPV	DQMOM	SANDIA
RF5	Rodrigues et al. (2018)	Tabulated	RFPV	ADSM	SANDIA
RF6	Jain and Xuan (2019)	Tabulated	RFPV	DQMOM	SANDIA
RF7	Yang et al. (2019)	Tabulated	RFPV	HMOM	SANDIA
RF8	Franzelli et al. (2015)	Tab.+Semi-Emp.	Hybrid	SE2eq	FIRST
RF9	Wick et al. (2017)	Tabulated	RFPV	HMOM	FIRST
RF10	Chong et al. (2018)	Tabulated	RFPV	HMOM	FIRST
RF11	Felden et al. (2018)	Analytical Reduction	ARC	SE2eq	FIRST
RF12	Grader et al. (2018)	Semi-detailed	Slavinskaya	CDSM	FIRST
RF13	Rodrigues (2018)	Tabulated	RFPV	ADSM	FIRST
RF14	Franzelli et al. (2019)	Tabulated	RFPV	SE3eq	FIRST
RF15	Chong et al. (2019)	Tabulated	RFPV	MOMs/SE2eq	FIRST
RF16	Gallen (2020)	Analytical Reduction	ARC	LST	FIRST

Table 1.2: *Summary of methodologies used for gas-phase chemistry and soot numerical modeling in LES of turbulent sooting flames found in literature. Three turbulent flame configurations are considered: Delft Flame III (DF3, Peeters et al. (1994)), Sandia non-premixed jet flame (SANDIA, Zhang et al. (2011)), and DLR FIRST aircraft combustor (FIRST, Geigle et al. (2013).)*

By looking into the chosen kinetic models, it is noticeable that the majority of the authors opted for a tabulated chemistry technique based on the work of Ihme and Pitsch (2008), called Radiation Flamelet/Progress Variable model or RFPV for short; where the look-up table contains a set of counterflow diffusion

flamelets considering radiative effect. In the case of RF11 and RF16 works, the analytically reduced chemistries (ARCs) were constructed by employing the YARC tool (Pepiot (2008)). RF8 used a hybrid chemistry made of a two-step six-species mechanism (Franzelli et al. (2012)) for fuel oxidation, paired with a tabulated chemistry based on Lecocq et al. (2014) to predict acetylene. The difference in each work mentioned before lies in the reference detailed kinetic mechanism used for the construction of the database, when a reduction technique was applied. When a detailed chemistry was selected, as RF2 or RF3, a strategy to accelerate the calculations was necessary and will be mentioned later.

The key factor in deciding which detailed mechanism to use was the precision in predicting soot precursors that are essential for the soot model. Most authors chose kinetic mechanisms that accurately reproduced PAHs with the intention of well capturing the soot nucleation: RF1, RF4, RF7, RF9 and RF10 used a detailed chemistry mechanism by Narayanaswamy et al. (2010) extended from Blanquart et al. (2009), that goes up to C_{16} and C_{18} species. RF5, RF13 and RF14 used KM2 chemistry (Wang et al. (2013)) and it considers PAHs up to coronene. RF11 picked the detailed mechanism from Narayanaswamy et al. (2010), resulting an ARC of 18 transported species. RF16 combined kinetics: the base kinetics taken from Bisetti et al. (2012) (up to naphthalene) with an extension for larger PAHs (up to pyrene) from Pang et al. (2013), retaining two ARCs with a total of 28 and 32 transported species, respectively.

In terms of soot numerical models, the majority decided to pursue a low-cost one, such as semi-empirical methods or MOMs.

RF8, RF11 and RF14 settled on semi-empirical (SE) models; the first two works used two-equations SE models (SE2eq) and the third one a three-equation SE model (SE3eq), respectively. RF8 and RF11 reproduced qualitatively soot formation fairly. Only RF14 model was able to both reproduce global quantities and reconstruct the NDF (*cf.* subsubsection 1.3.3.5). Also, SE2eq parameters were ad-hoc tuned.

RF1, RF7, RF9 and RF10 opted for HMOM (Mueller et al. (2009a)), RF4 decided for DQMOM (Blanquart and Pitsch (2009)). The main difference of these MOMs lies on the moment closure: HMOM combines two methods (H stands for hybrid), MOMIC (Frenklach and Harris (1987)) and DQMOM, in an attempt to hold the simple numerical closure of the first and, at the same time, be able to well reproduce the bimodal shape of a PSD as the second does. Satisfactory predictions in global quantities were obtained with these methods. Nonetheless, inherent to some MOMs, the reconstruction of the NDF was not possible.

RF2, using a hard-coded GRI-1.2 detailed mechanism (Frenklach et al. (1995); Frenklach et al. (1995)) to accelerate calculations, has tested the SE2eq of Akridis and Rigopoulos (2017), a modified version of Lindstedt and Louloudi (2005) model to capture polydispersion; but it missed to well capture the right level of soot and the nucleation position in the DF3 configuration. RF3 ad-

dressed the same problem using its own gas-phase kinetics, which was boosted with the ISAT algorithm (Pope (1997)), and used HMOM for soot, getting better results than RF1 and RF2, and concluded that soot formation is sensitive to the gas-phase chemistry, which might explain RF2 mispredictions.
RF5 and RF13 opted for a more detailed sectional model with 25 sections, having very good results in soot characterization. Nevertheless, for industrial applications, to end up dealing with a system of equations with 33 variables is very computationally demanding to solve: it costs 3 times as much as SE3eq (Franzelli et al. (2019)). RF12 decided for a CDSM consisting in: Slavinskaya's semi-detailed chemistry (Slavinskaya and Frank (2009); Slavinskaya et al. (2012)), including 43 species and 403 reactions, and adding 6 sections for lumped PAHs and its radicals, and 30 sections for soot based on the model developed in Blacha et al. (2012) and Eberle et al. (2017); where a total of 79 species and sections were transported, making it 10% more expensive than RF13's work. RF13 results are better than RF12's comparing against experiments, giving the clue that detailed gas kinetics and detailed soot models are a significant factor for soot prediction.
RF16 chose the Lagrangian method LST. Although LST implies a lower cost, if it is combined with the transport of 28 or 32 species and the statistical convergence issues in Lagrangian methods, the simulations in overall turned very expensive as in RF13 work.
In the FIRST configuration, RF15 studied the influence of kinetic mechanisms selected for the construction of the RFPV table, using mechanisms from Narayanaswamy et al. (2010) (NRB) and Metcalfe et al. (2013) (KAM1.0); and the soot formation model applying SE2eq, HMOM and CQMOM (Yuan and Fox (2011); Sung et al. (2014)). A comparison of soot results in each numerical models against the experimental measurement is shown in Fig. 1.8 (Chong et al. (2019)). It reveals that soot prediction is very sensitive to the choice of both the gas kinetics and soot numerical model. For instance, for all given soot model, the KAM1.0 the soot mass production is always higher than using NRB, because of higher nucleation and condensation on the first one (Chong et al. (2019)). In another example, using a semi-empirical model the production on soot volume fraction is clearly overpredicted comparing to the other methods. Nevertheless, RF15 also determined that CQMOM produces much higher soot number density at lower size of particles compared to HMOM, attributed to a faster rate of coagulation in the latter.
Following RF4's study, RF6 investigated the influence of individual PAH to soot nucleation and quantified the impact from large aromatic species on soot yield. It was concluded that there are non-negligible differences between the soot inception and distribution when comparing simulations using one-PAH model for nucleation or multiple-PAHs model for nucleation. However, these differences in the numerical models are smaller than the differences between the numerical predictions and experimental measurements, which suggests that the sensitivity of other model components might be more important (Jain and

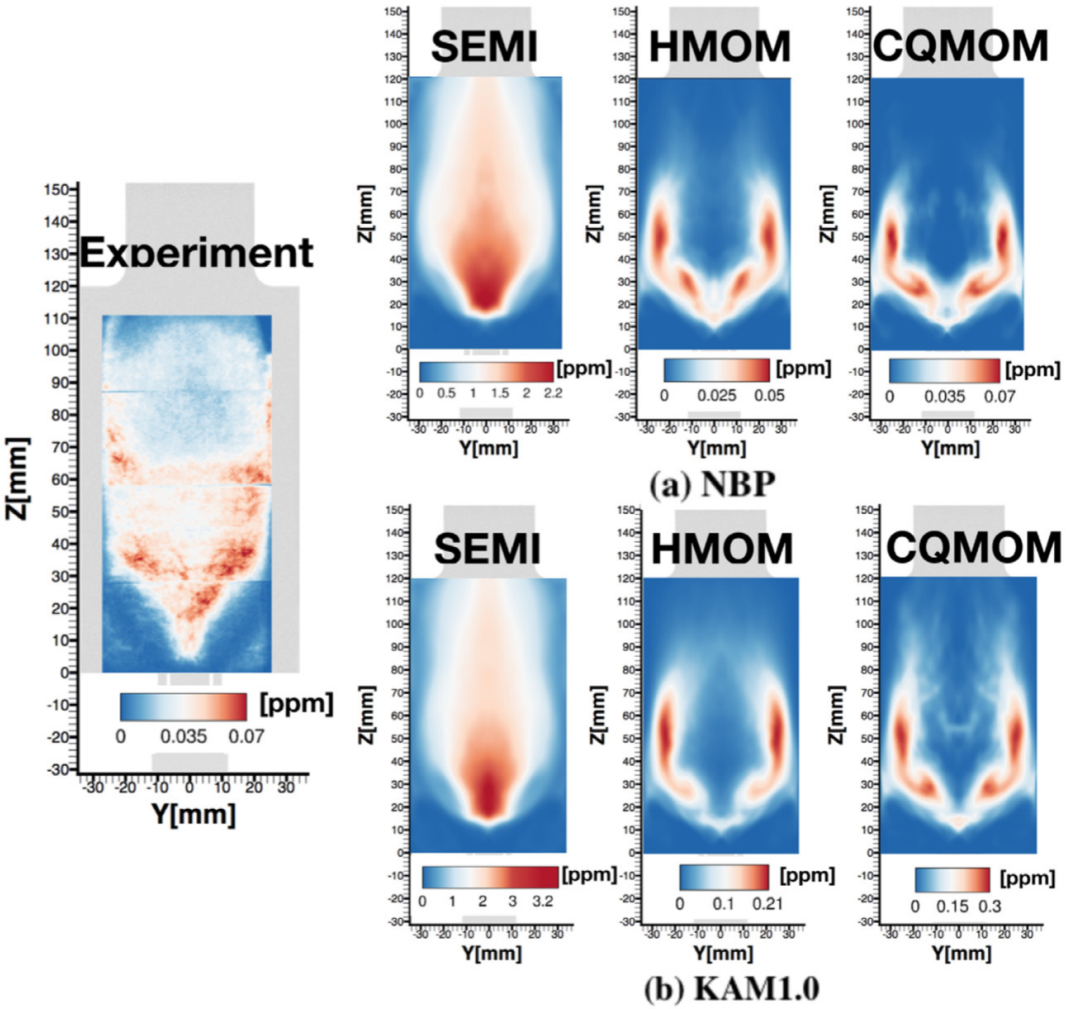

Figure 1.8: *Time-averaged soot volume fraction contours for the experimental measurement (left) and the different soot and moment description models. Extracted from Chong et al. (2019).*

Xuan (2019)). A similar issue was found by RF16 in the FIRST configuration: the ARCs counted with a model for soot nucleation that contained a single PAH dimerization (naphthalene and pyrene) to model soot inception. Indeed, Selvaraj et al. (2016) found that it was insufficient to accurately reproduce soot phenomena in the examined flames if pyrene was the only species considered for nucleation, as one of the mechanisms developed by RF16. Nevertheless, the ARC was derived by using only premixed flames as reference, which imply that several pathways that are activated primarily in diffusion flames were ignored, making hard to conclude in this particular study which effect was more critical.

1.5 Objectives

The virtual model formulation is based on the chemical data provided by a reliable and accurate detailed mechanism. The virtual chemistry approach remains powerful and flexible: one can develop a simplified mechanism *a priori*, without the need to perform *ad hoc* tuning of parameters based on experimental data. In this case, the objective of this thesis is to develop a reduced virtual mechanism for soot formation prediction in hydrocarbon-air combustion at low CPU cost. A sophisticated modeling assumption is proposed to limit the error propagation in the gas-solid transition. Also, a new procedure based on virtual approach basics to account for radiative heat losses is developed. The resulting models are first validated in 1-D laminar ethylene-air flames. Then, the models are applied to 2-D laminar flame configurations. Finally, a subgrid-scale model for turbulence-soot interactions is developed for LES of turbulent sooting flames.

1.6 Methodology

The gas-phase kinetics is represented by detailed or reduced models that enable to predict the soot precursors (C_2H_2, PAHs, etc.). Then, a nucleation model for soot small particles is considered, allowing the transition from gas to solid phases. The nucleating soot particles and other chemical species from the gas mixture are then taken into account by the soot numerical model to predict the soot evolution. The final solution is obtained in terms of soot volume fraction, particle number density, etc.
The virtual mechanism proposed in the present work will be constructed in two parts. In a first part where flame structure and mixture properties are treated by a virtual main mechanism. Then the second part deals with soot volume fraction prediction by a virtual sub-mechanism. The optimization of these two components of the virtual approach is done using a target flames library built with a detailed mechanism and user-chosen configurations. Knowing that the chemistry has a big impact into soot formation, the detailed chemistry must be representative of the case considered and accurate in prediction of the quantities of interest: it will trace the physics followed by the virtual mechanism through the learning database. A machine learning algorithm will then perform the optimization and train the set of virtual species and virtual reactions properties. Contrary to real mechanisms, a virtual chemistry would preferably look for the final product: soot volume fraction for instance. As a novel approach, soot volume fraction estimation is therefore envisaged in a straightforward way. To do so, the idea is to predict a virtual soot pseudo-species, similar to CDSM with the BINs. By doing so, the virtual chemistry would not require a coupling between the gas phase and the solid phase, but instead it would include a gas-solid formalism without distinction and would allow a simplified structure without making further assumptions, leading to very low computational cost.

In addition, a new virtual approach is proposed to account for radiative heat transfer.
As in every virtual mechanism, it would also be possible to perform LES of turbulent sooting flames in different configuration and combustion regimes, a feature that is not common to other models with reduced kinetics. The turbulence-soot interactions will be addressed by a new subgrid-scale model for the virtual soot sub-mechanism, which depends on the turbulent combustion regime encountered.
The structure of this thesis is as follows. Chapter 2 introduces the virtual chemistry approach. The virtual chemistry methodology is first presented. Next, the virtual main mechanism is presented, which covers the flame structure prediction. Then, the state of the art of virtual sub-mechanisms for pollutant prediction is presented: examples of the CO and NOx virtual models in laminar flames are shown. Finally, the reactive flow governing equations in the virtual chemistry framework are described.
In Chapter 3, the virtual soot sub-mechanism is developed. First the virtual chemistry principle is introduced for laminar flames. The virtual soot sub-mechanism is presented: the architecture of the virtual scheme and the optimization strategy are described. Then, the virtual models for gas and soot radiation are described. Once this the virtual model is established, the optimization set-up is exhibited: the learning database using the detailed chemistry solutions and the computed cases are shown. The new virtual main and sub-mechanisms, and virtual radiative models are validated on 1-D laminar ethylene-air flames. Last, the virtual models are challenged in 2-D laminar flames configurations: a premixed slot burner and a non-premixed coflow burner.
The basics of turbulent combustion modeling are presented in Chapter 4. Different numerical methods in turbulent combustion are first introduced. Then, the reactive flow governing equations in the LES framework are reported: a description of the LES formalism is made, followed by the derivation of the filtered balance equations. Lastly, the turbulent combustion models in LES are presented, with an especial focus on the Thickened Flame model for LES (TFLES).
Chapter 5 is dedicated to the application of the new soot virtual models to turbulent sooting flames. The study begins with the introduction of the laminar combustion model and continues with its coupling to the resolution of turbulent flames. Then, time and length scale analyses of the laminar flames are performed, which helps to identify the combustion regimes in the turbulent sooting flames. A subgrid-scale model is then proposed to account for turbulence-soot interactions using the virtual sub-mechanism. Later, a 3-D turbulent sooting flame configuration is introduced, where a description of the experimental and numerical setups is reported. Finally, the numerical results using the new virtual models are presented for the cold and reactive flows validations.

1.7 Conclusion

In this chapter, a physico-chemical description of soot formation was introduced. The whole process comprises very complex stages of particle dynamics (nucleation, condensation, coagulation) and surface chemistry (oxidation, surface growth) that are very important and should be included in a soot model. The impact of soot precursors and soot geometry was also discussed.
A revision of gas-phase kinetics modeling was made and the role of detailed and reduced mechanisms in numerical combustion was identified by focusing on the advantages and disadvantages of each method, and on the interaction between turbulent flames and soot formation.
The different soot numerical models were subsequently presented. Soot evolution prediction still remains a big challenge in numerical combustion, highlighting the direct commitment between precision in soot prediction and computational cost of simulations.
After the overview of previous works in section 1.4, it should be mentioned that the choice of the numerical soot model and the gas phase chemistry has a significant influence on turbulent flames results and the construction of the new reduced model must be done very carefully.
As it will be discussed in Chapter 3, a reference flame database including soot formation should be defined prior to the construction of the virtual mechanism. The present work will consider the detailed soot kinetics model proposed by the CRECK Modeling Group (Saggese et al. (2015)). This kinetic mechanism has been extensively validated on several experimental data in many different systems (Saggese et al. (2015); Pejpichestakul et al. (2019); Pejpichestakul et al. (2019)). It includes the detailed chemistry of the gas-phase (oxidation, hydrocarbon pyrolysis, PAH formation, etc.), and the chemistry governing the formation and evolution of soot particles and aggregates (Saggese et al. (2015)); *i.e.* this kinetic scheme spans the complexity necessary to hold every sooting flame characteristics, from gas phase to solid phase.
In practical 3-D turbulent configurations, simulating a sooting flame with such a detailed kinetic mechanism is unfeasible. This is why a virtual reduced chemistry model constructed by targeting flame properties using this chemistry is a good alternative: representative physico-chemical phenomena of soot formation will be pursued by the virtual chemistry.
Finally, virtual chemistry concept and philosophy of the present work was presented. A new strategy for predicting soot formation has been established, which would allow aiming at the soot volume fraction without making further assumptions on the gas-solid transition. Similar to BINs in CRECK's model, it will do it by considering a virtual pseudo-species representing soot particles. This approach conducts to lower the CPU cost in LES of turbulent sooting flames.

Chapter 2

Virtual Chemistry approach

Contents

In the present chapter the virtual chemistry methodology is presented. The virtual main mechanism is presented in three steps: the thermodynamics, transport and kinetic rate parameters optimizations. A state of the art of the virtual sub-mechanisms for pollutant prediction is reported. Finally, transport equations in the virtual chemistry framework are derived.

2.1 Introduction

This original virtual chemistry method was proposed at EM2C laboratory by Cailler et al. (2017). The main purpose of a virtual mechanism is to recover specific flame physical properties over a given set of targeted flame configurations (Cailler et al. (2017)) computed under detailed chemistry assumption. The virtual chemistry is designed to retrieve for instance the flame temperature, the laminar flame speed, the formation of pollutants, etc. The target flames archetypes should be representative of those encountered in practical configurations. In this chapter, virtual chemistry approach is described and a few examples are given in the state of the art of methane-air flames applications were developed in the last four years (Cailler et al. (2017); Cailler (2018); Cailler et al. (2020); Maio (2020); Maio et al. (2020)). New models for ethylene-air sooting flames and radiative heat losses are presented in chapter 3.

2.2 Virtual chemistry methodology

A virtual kinetic mechanism is basically divided in two independent blocks: the main virtual mechanism and satellite virtual sub-mechanisms (Cailler et al. (2020)). Figure 3.1 displays a schematic presentation of the approach. The main mechanism is trained to reproduce mean mixture properties, temperature and heat release, whereas the sub-mechanisms are addressed to predict species of interest, such as pollutants formation (CO, NOx, PAHs or soot).

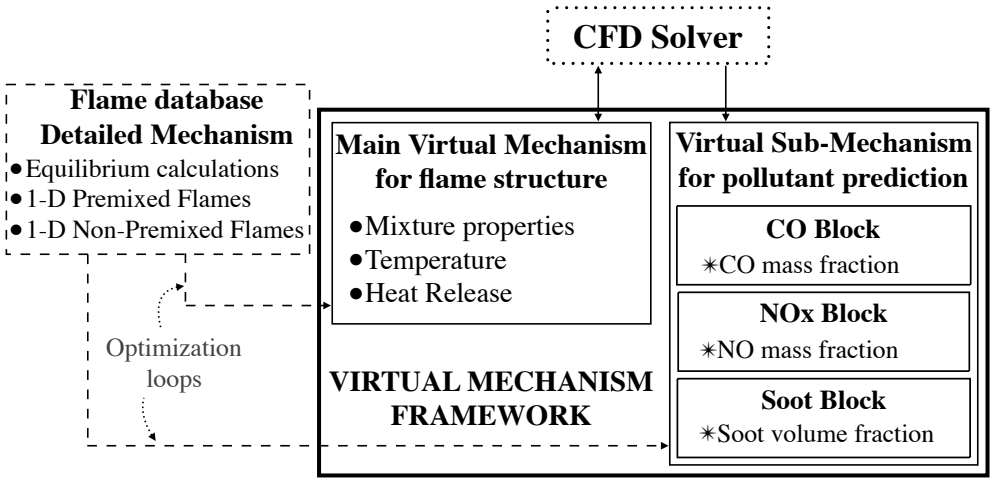

Figure 2.1: *Schematics of virtual chemistry methodology. Based on Cailler et al. (2020).*

In the following subsections this methodology is presented for the main and satellite mechanisms. The former is subdivided in three parts attacking the thermodynamics, the transport and chemical kinetics optimization. The latter

is split in two as it represents the late works on CO and NO prediction using virtual chemistry. The optimization techniques correspond to those extensively described in Cailler (2018) and Maio (2020) and they will not be introduced in the present manuscript.

2.3 Virtual main mechanism: Temperature prediction

A main mechanism consisting in 2 virtual reactions R_1^M and R_2^M, and 8 virtual species was proposed in Cailler et al. (2017) for methane-air flames:

$$\alpha^v_{F,1}F + \alpha^v_{Ox,1}Ox + \alpha^v_{D,1}D \rightarrow \alpha^v_{I,1}I + \alpha^v_{D,1}D \qquad (R_1^M)$$

$$\alpha^v_{I,2}I \rightarrow \sum_{k=1}^{N_P^v=4} \alpha^v_{P_{k,2}}P_k \qquad (R_2^M)$$

where F represents the fuel (methane, ethylene, etc.), Ox the oxidizer (O_2), D the inert dilutant species (N_2), I the virtual intermediate species and P_k the virtual products. The $\alpha^v_{k,r}$ refers to the stoichiomethic coefficients per unit mass of the k^{th} virtual species in the r^{th} virtual reaction, and N_P^v the number of virtual products. The super-index v stands for virtual chemistry quantities, and hereinafter, d will indicate the detailed chemistry quantities.
To define our virtual chemistry system, it is firstly necessary to determine thermodynamic properties of the virtual species. Secondly, the transport properties of the gas mixture are specified. Finally, kinetic parameters of the virtual reactions are established.

2.3.1 Thermodynamic properties optimization

The thermodynamic properties of virtual products are optimized by considering thermodynamic properties at equilibrium in adiabatic conditions, such as the enthalpy (h^v) and the heat capacity (c_p) of the mixture (Cailler et al. (2017); Cailler et al. (2020)).
The vector of thermodynamic properties of the virtual species k is $\mathbf{\Psi^v_k} = \left\{c^v_{p,k}, h^v_k\right\}$, where its elements are calculated by using the NASA fitted polynomials functions (McBride et al. (1993)):

$$\frac{c_{p,k}}{R} = a_{1,k} + a_{2,k}T + a_{3,k}T^2 + a_{4,k}T^3 + a_{5,k}T^4; \qquad (2.1)$$

$$\frac{h_{p,k}}{RT} = a_{1,k} + \frac{a_{2,k}}{2}T + \frac{a_{3,k}}{3}T^2 + \frac{a_{4,k}}{4}T^3 + \frac{a_{5,k}}{5}T^4 + \frac{a_{6,k}}{T}. \qquad (2.2)$$

Each thermodynamic coefficient $a^v_{l,k}$ is then optimized for every virtual product in R^M_2 so that they meet the thermodynamic mixture properties at the initial fresh gas condition and at thermodynamic equilibrium of burnt gases. Optimization using a database accounting for non-adiabatic effects is also discussed in Maio et al. (2019).
The optimization is done by using an in-house genetic algorithm developed by Cailler (2018), where the objective cost function to minimize is:

$$f^{\text{th}} = |\psi^{\mathbf{v}} - \psi^{\mathbf{d}}| \tag{2.3}$$

where the superscripts d and v stand for detailed and virtual chemistries quantities, respectively; and ψ represents the thermodynamic properties of the gaseous mixture. These are obtained as follows:

$$\psi^v = \sum_{k=1}^{N^v_{sp}} \psi^v_k Y^v_k; \quad \psi^d = \sum_{k=1}^{N^d_{sp}} \psi^d_k Y^d_k; \tag{2.4}$$

where Y_k is the mass fractions of the k^{th} species, N_{sp} is the number of species in the kinetic mechanism. ψ_k is referred to the thermodynamic properties of the k^{th} species in the virtual or detailed mechanisms ($c_{p,k}$ or h_k).
The fuel F, oxidizer Ox and dilutant species D retain the real thermo-chemical properties of their respective species in the detailed mechanism, therefore the fresh gases thermodynamic conditions are clearly achieved.
Since the intermediate species I is considered to be fully consumed in reaction R^M_2, only virtual products P_k should be optimized at the thermodynamic equilibrium condition.
The objective cost function is then written as:

$$f^{\text{th}} = \sum_{k=1}^{N^v_{sp}} \psi^v_k Y^v_k|^{eq} - \sum_{k=1}^{N^d_{sp}} \psi^d_k Y^d_k|^{eq}; \tag{2.5}$$

where $|^{eq}$ means that it is evaluated at thermodynamic equilibrium condition. Separating the virtual reactants (F, Ox, D) and virtual products; and recalling no intermediate species present at equilibrium state:

$$f^{\text{th}} = \sum_{k\in\{F;Ox;D\}} \psi^v_k Y^v_k|^{eq} + \sum_{k=1}^{N^v_P} \psi^v_{P_k} Y^v_{P_k}|^{eq} - \sum_{k=1}^{N^d_{sp}} \psi^d_k Y^d_k|^{eq}; \tag{2.6}$$

where $Y^v_{P_k}$ is the mass fraction of the k^{th} virtual product P_k and $\psi^v_{P_k}$ its thermodynamic property. The first summation term is known since thermodynamic parameters of F, Ox and D are known. Similarly, the third summation term

is obtained from detailed chemistry calculations. Lets define $Y_P^v = \sum_k Y_{P_k}^v$ the virtual products mass fraction, then each virtual product mass fraction at equilibrium can be expressed as $Y_{P_k}^v|^{eq} = \alpha_{P_k}^v Y_P^v$, with $\alpha_{P_k}^v$ the stoichiometric coefficient per unit mass of the k^{th} virtual product (*cf.* reaction R_2^M).
Using the polynomials expressions in Eqs. 2.1 and 2.2, one can write:

$$f^{\text{th}} = \sum_{l=1}^{N_T=6} \left[\sum_{k=1}^{N_P^v} a_{l,P_k}^v \alpha_{P_k}^v - \sigma_l / Y_P^v|^{eq} \right]; \tag{2.7}$$

by considering σ_l as:

$$\sigma_l = \sum_{k=1}^{N_{sp}^d} a_{l,k}^d Y_k^d|^{eq} - \sum_{k\in\{F;Ox;D\}} a_{l,k}^v Y_k^v|^{eq} \quad \text{for} \quad l = 1, 2, \ldots, N_T. \tag{2.8}$$

The quantity $\sigma_l / Y_P^v|^{eq}$ is known *a priori* from detailed results and is defined as the target quantity in the optimization procedure and it is aimed to learn the mixture thermodynamics at equilibrium in the main virtual mechanism. The counter l goes up to $N_T = 6$ to retrieve both $c_{p,k}$ and h_k. The final results of the optimization include the values of $a_{l,k}^v$ for every virtual product, followed by an inversion of the linear system:

$$\sum_{k=1}^{N_P^v} a_{l,P_k}^v \alpha_{P_k}^v = \frac{\sigma_l}{Y_P^v|^{eq}}; \tag{2.9}$$

where the stoichiometric coefficients per unit mass $\alpha_{P_k}^v$ are determined, as in Cailler et al. (2017).
Expression 2.7 is given for a single initial state condition: pressure, temperature and element's composition. In global mechanisms (*cf.* subsection 1.2.2), to mimic the variation of mixture properties at equilibrium for different initial compositions, the stoichiometric coefficients per unit mass are set as a function of the fresh gases composition (*e.g.* mixture fraction Z), *i.e.* $\alpha_{P_k}^v = \alpha_{P_k}^v(Z)$. Then, to optimize the entire thermodynamic system, one needs to include them all in the objective cost function. In this case, for N_c initial state conditions, the total cost function will be:

$$f_M^{\text{th}} = \sum_{j=1}^{N_c} f^{\text{th}}(Z_j); \tag{2.10}$$

this will permit to well capture the equilibrium flame temperature over the entire flammability range (Cailler et al. (2017)), as seen in Fig. 2.2 for methane-air combustion (Maio (2020)).

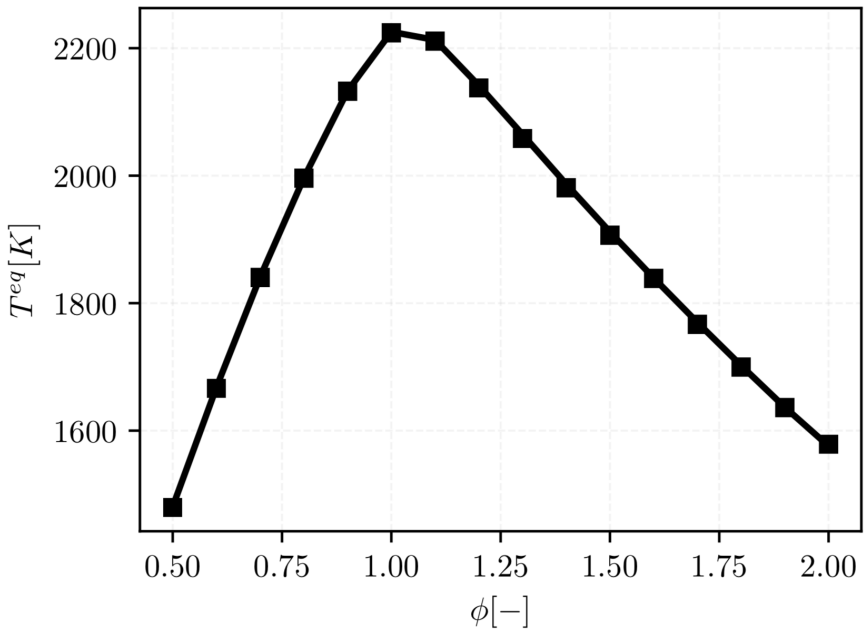

Figure 2.2: *Equilibrium temperature at adiabatic conditions over the entire flammability range for methane-air combustion at atmospheric pressure and 300 K. Virtual chemistry results (symbols) compared against the 53-species reference detailed chemistry (continuous line). From Maio (2020).*

2.3.2 Transport properties

Regarding transport equations, the gas mixture dynamic viscosity is calculated using a power-law approximation:

$$\mu^v = \mu_0 \left(\frac{T}{T_0} \right)^{\beta}; \tag{2.11}$$

where μ_0 is the reference dynamic viscosity at temperature T_0 and β was optimized to get the evolution of viscosity with temperature. For methane-air and ethylene-air combustion $\mu_0 = 1.8405$ $[\mathrm{kg} \cdot \mathrm{m}^{-1} \cdot \mathrm{s}^{-1}]$ and $\beta = 0.6759$, previously validated for a global chemistry model (Franzelli et al. (2010); Franzelli et al. (2015)). The mixture thermal conductivity λ^v is related to the reference Prandtl number Pr_0^v, the gas viscosity μ^v and the heat capacity c_p^v as:

$$\lambda^v = \frac{\mu^v c_p^v}{Pr_0^v}; \tag{2.12}$$

Finally, the virtual species molecular diffusion term is expressed using a unity Lewis number, this means that for the molecular diffusion term can be written:

$$Y_k^v V_{k,i}^v = -D^v \frac{\partial Y_k^v}{\partial x_i} = -\left(\frac{\lambda^v}{\rho c_p^v} \right) \frac{\partial Y_k^v}{\partial x_i}, \tag{2.13}$$

where $V^v_{k,i}$ is the i^{th} component of the molecular diffusion velocity of the k^{th} virtual species. The molecular diffusion coefficients of virtual species are considered equals to D^v for $k = 1, \ldots, N^v_{sp}$ (Cailler et al. (2020)).
Despite having set Le=1 for the virtual species, this does not prevent us targeting flame solutions computed using detailed mechanisms and more complex diffusion models for the molecular diffusion terms (*e.g.* mixture-averaged diffusion).
The optimization of transport coefficients of virtual species in the main mechanism to capture preferential diffusion effects is out of scope of this work. However, a novel treatment for soot transport properties in the new soot virtual sub-mechanism is established in chapter 3.

2.3.3 Kinetic parameters optimization

Chemical reaction rates of virtual reactions R^M_1 and R^M_2 are given by their respective Arrhenius closures:

$$q_1 = A^v_1(Z) \exp\left(\frac{-E^v_{a,1}}{RT}\right) [F]^{n^v_{F,1}} [Ox]^{n^v_{Ox,1}}; \tag{2.14}$$

$$q_2 = A^v_2 \exp\left(\frac{-E^v_{a,2}}{RT}\right) [I]^{n^v_{I,2}(Z)}. \tag{2.15}$$

Here, for any virtual reaction r and virtual species k, the pre-exponential constant A^v_r, the activation energy $E^v_{a,r}$ and the reaction rate orders $n_{k,r}$ are optimized in order to minimize a cost function defined as:

$$f^{kin}_M(A^v_r, E^v_{a,r}, n^v_{k,r}) = \sum_{i=1}^{N_c} \left(w_1 \frac{\left|S^v_{L_i} - S^d_{L_i}\right|}{S^d_{L_i}} + w_2 \frac{\left\|T^v_i - T^d_i\right\|_{L_2}}{\left\|T^d_i\right\|_{L_2}} \right) \tag{2.16}$$

where S_{L_i} and T_i are the laminar flame speed and the temperature profile of the i^{th} operating condition (out of N_c), and w_1 and w_2 are the cost function weights fixed at 0.01 and 0.99, respectively, with the intention to give a suitable impact on both criteria (Cailler et al. (2017)). The L_2-norm applied to a function $\varphi(x)$ is defined as $\|\varphi\|_{L_2} = \int_{-\infty}^{\infty} \varphi(x)^2 dx$. The Z-dependence of kinetic parameters A^v_1 and $n^v_{I,2}$ serves to adjust the reaction rates for a wide range of operating conditions Cailler et al. (2017). In this way, the 2-step structure captures for the entire range of flammability of 1-D premixed laminar flames: laminar flame speed and temperature profiles up to equilibrium (*cf.* Figs. 2.3 and 2.4). Also, this model is capable to retrieve 1-D counterflow diffusion flames temperature profiles for a wide span of strain rates (*cf.* Fig. 2.5).

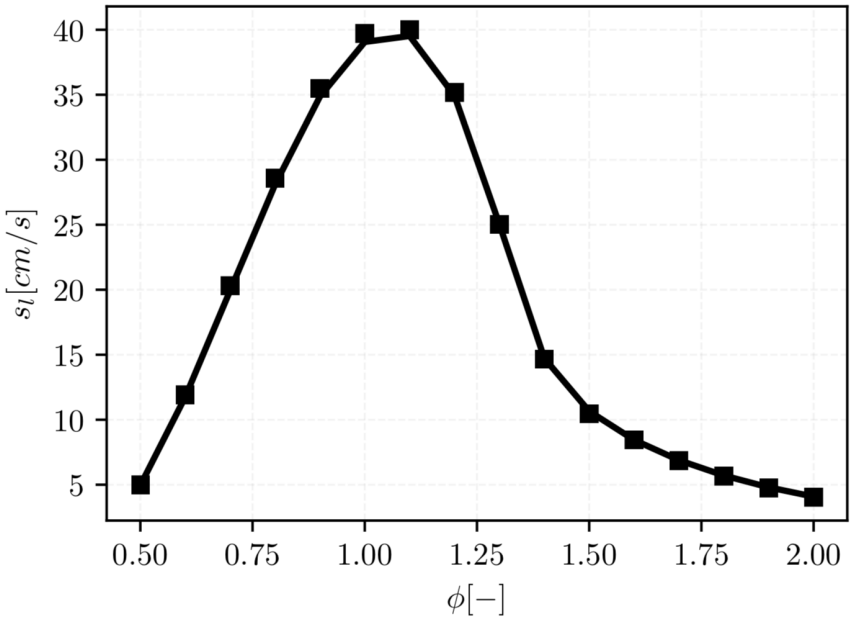

Figure 2.3: *Laminar flame speed for 1-D methane-air freely-propagating flames at 1 atm. Virtual chemistry (symbols) is compared against detailed chemistry (continuous line). From Maio (2020).*

2.4 Virtual sub-mechanisms: State of the art

Pollutant prediction using virtual chemistry is one of the relevant topics of this approach because it could be added to the solver depending on the user's necessity. CO and NO virtual mechanisms were developed at EM2C laboratory in previous PhD thesis (Cailler (2018); Maio (2020)). These mechanisms were validated in 1-D and 2-D laminar flames, as well as 3-D turbulent flames in different practical configurations and regimes (Cailler et al. (2017); Cailler et al. (2020); Maio et al. (2019); Maio et al. (2020)).

2.4.1 CO virtual sub-mechanism

For methane-air flames Cailler (2018) proposed the CO 3-step virtual sub-mechanism below:

$$\alpha_F^{v,1} F + \alpha_{Ox}^{v,1} Ox \rightarrow \alpha_{CO}^{v,1} CO + (1 - \alpha_{CO}^{v,1}) A_1 \qquad (R_1^{CO})$$

$$F + A_1 \rightarrow F + CO \qquad (R_2^{CO})$$

$$CO \leftrightarrow A_2 \qquad (R_3^{CO})$$

Here A_1 and A_2 are two new intermediate virtual species. Reaction R_1^{CO} represents the fast CO production from oxidation, while R_2^{CO} represents the slow

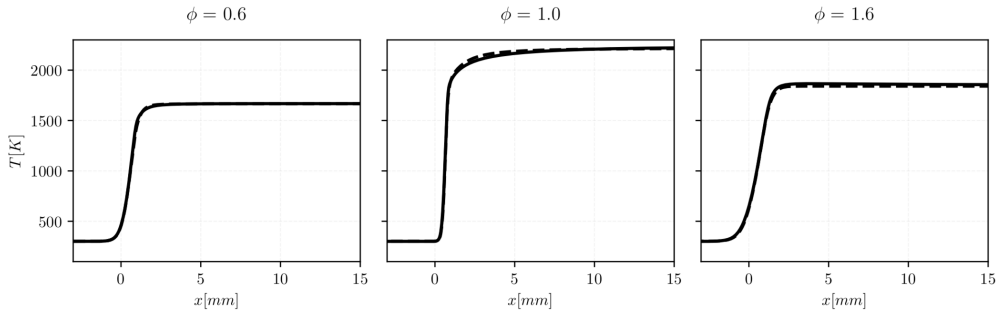

Figure 2.4: *Temperature profiles of 1-D methane-air freely-propagating flames for different inlet equivalence ratios ϕ: lean, stoichiometric, rich. Virtual chemistry (dashed line) is compared against detailed chemistry (continuous line). From Maio (2020).*

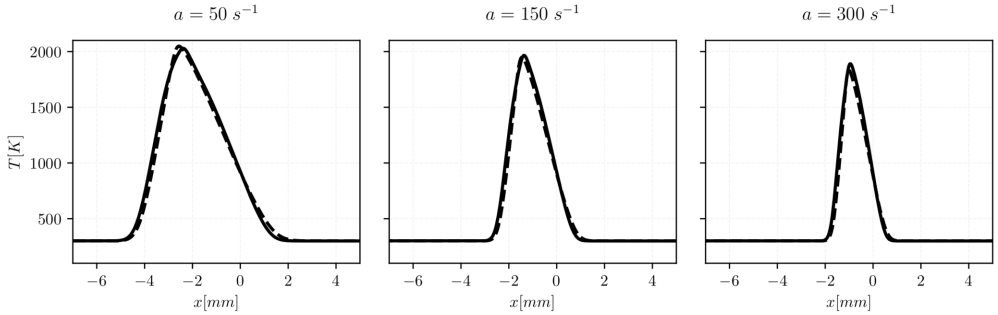

Figure 2.5: *Temperature profiles of 1-D methane-air counterflow diffusion flames for different strain rates a. Virtual chemistry (dashed line) is compared against detailed chemistry (continuous line). From Maio (2020).*

formation in rich flames. Reaction R_3^{CO} captures the recombination processes in the post-flame zone and includes a reverse reaction to predict CO equilibrium concentration. Reaction R_1^{CO} saved the same parameters from R_1^M for consistency in F and Ox consumption. This virtual scheme was primarily validated in 1-D laminar premixed and non-premixed flames and tested in 2-D laminar flames (*cf.* Fig. 2.6).
Similarly to the main mechanism, the reaction rate parameters of reactions R_1^{CO} to R_3^{CO} are optimized by minimizing the following objective function:

$$f_{CO}^{kin}(A_r^v, E_{a,r}^v, F_{k,r}^v) = \sum_{i=1}^{N_c} \frac{\left\| Y_{CO,i}^v - Y_{CO,i}^d \right\|_{L_2}}{\left\| Y_{CO,i}^d \right\|_{L_2}}; \tag{2.17}$$

where for each i^{th} operating condition, out of N_c operating conditions, it is considered the CO mass fraction profiles of the detailed and virtual mechanisms: $Y_{CO,i}^d$ and $Y_{CO,i}^v$ respectively.
The CO virtual mechanism was extended to the non-adiabatic case by Maio

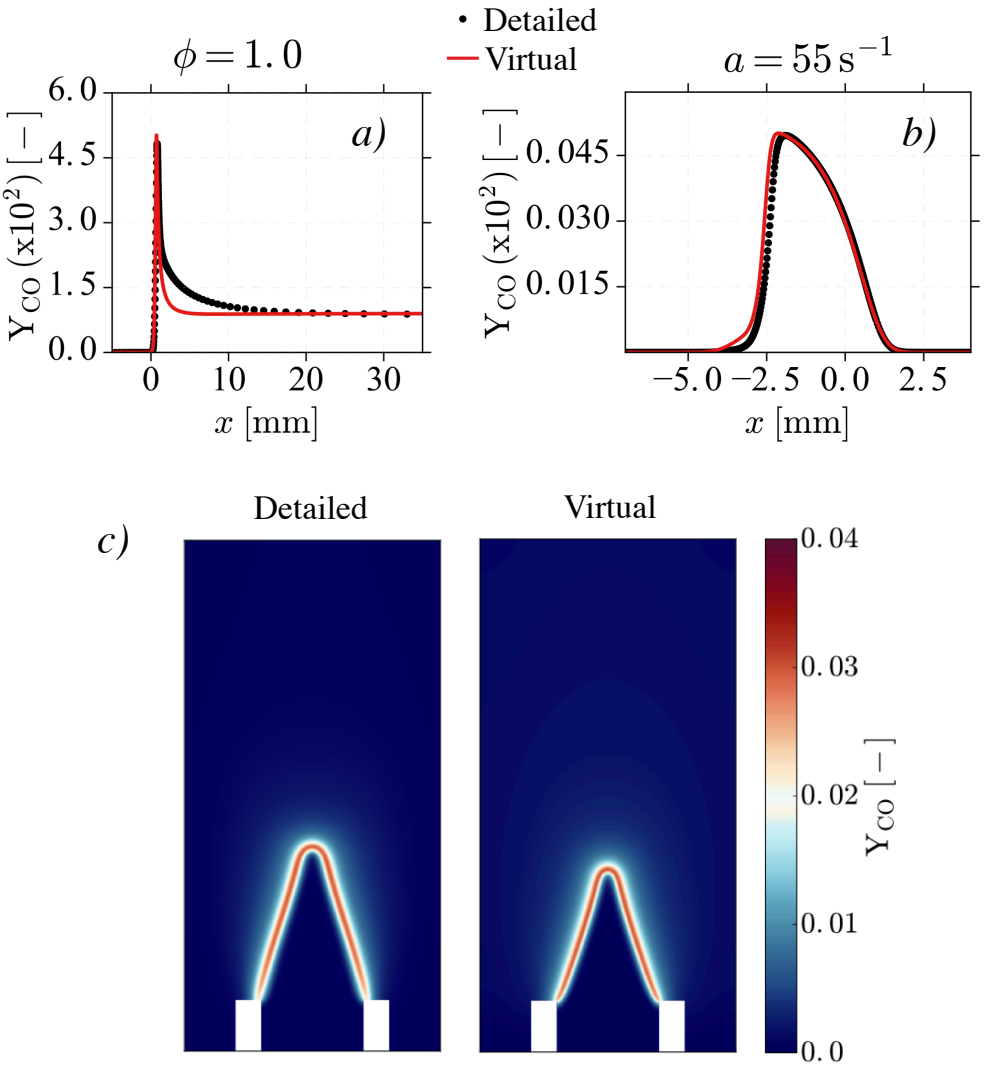

Figure 2.6: *CO mass fraction profiles in 1-D methane-air laminar flames: a) Premixed flame, b) Non-premixed counterflow flame. c) A 2-D laminar flame example: CO mass fraction fields in a Partially-Premixed Slot Burner using detailed chemistry (left) and virtual chemistry (right). From Cailler (2018).*

et al. (2019). In addition, it was challenged in turbulent configurations including wall heat losses and also in multi-regime conditions (Maio (2020)); in both cases having a very good agreements comparing to experimental results.

2.4.2 NO virtual sub-mechanism

Maio (2020) has proposed a NOx virtual sub-mechanism for methane-air flames that accounts for the whole NO pathway through 6 virtual reactions as is shown

below:

$$\alpha_F^{v,1} F + \alpha_{Ox}^{v,1} Ox \rightarrow \alpha_{B_1}^{v,1} B_1 + \alpha_{B_2}^{v,1} B_2 + \alpha_{B_3}^{v,1} B_3 \qquad (R_1^{NO})$$

$$B_1 + F + Ox \rightarrow \alpha_{NO}^{v,2} NO + \alpha_{B_2}^{v,2} B_2 \qquad (R_2^{NO})$$

$$F + NO \rightarrow F + B_2 \qquad (R_3^{NO})$$

$$B_3 \rightarrow NO \qquad (R_4^{NO})$$

$$B_3 \rightarrow B_2 \qquad (R_5^{NO})$$

$$B_2 \leftrightarrow NO \qquad (R_6^{NO})$$

B_1, B_2 and B_3 are additional intermediate species and are conceived in reaction R_1^{NO}. Reaction R_2^{NO} and R_3^{NO} are dedicated to predict prompt NO. Reaction R_3^{NO} also captures the fast NO reburning in rich conditions. Reactions R_4^{NO} to R_6^{NO} are dedicated to slow NO formation in the post-flame zone. In addition, R_6^{NO} reverse virtual reaction guarantees equilibrium conditions. Reaction R_1^{NO} maintains the values from virtual reaction R_1^{M} like in CO virtual sub-mechanism. NO virtual mechanism was firstly validated in 1-D laminar premixed and non-premixed flames and tested in 2-D laminar flames (*cf.* Fig. 2.7).
The optimization was done differently this time. The optimization was split in two steps: the first step to capture exclusively prompt NO and the second one to incorporate thermal NO and reburning (Maio et al. (2020)). The cost function associated to this optimization is similar to the CO case:

$$f_{NO}^{kin}(A_r^v, E_{a,r}^v, F_{k,r}^v) = \sum_{i=1}^{N_c} \frac{\left\| Y_{NO,i}^v - Y_{NO,i}^d \right\|_{L_2}}{\left\| Y_{NO,i}^d \right\|_{L_2}}; \qquad (2.18)$$

where the NO mass fraction profiles are intervening ($Y_{NO}^d(x)$ and $Y_{NO}^v(x)$) instead for every operating condition considered.
An extension of the NO virtual mechanism for n-heptane-air flames is under development by Nguyen-Van (2021) and is challenged in a 3-D turbulent two-phase combustion flame.

2.5 Reactive flow governing equations

The reactive flow governing equations are as follows:

Virtual main mechanism:

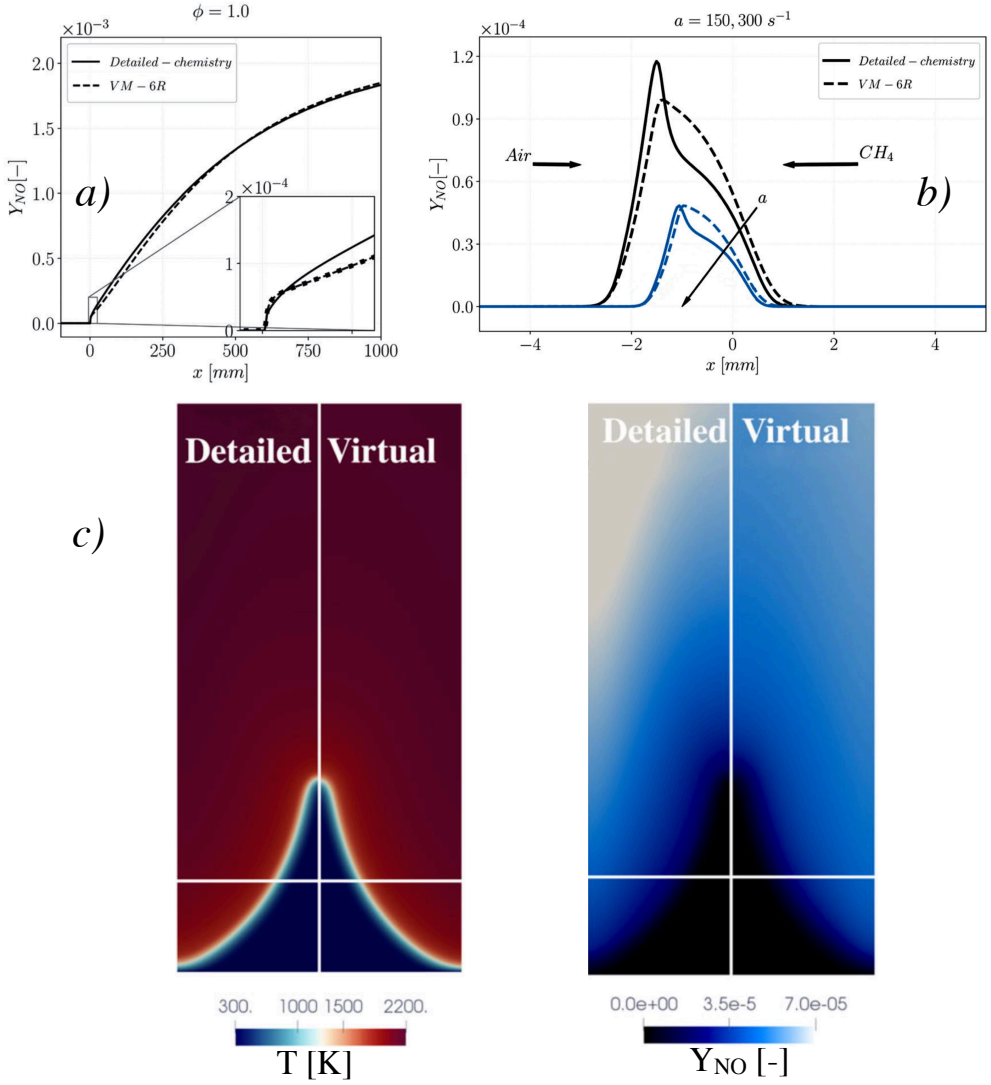

Figure 2.7: *NO mass fraction profiles in 1-D methane-air laminar flames: a) Premixed flame, b) Non-premixed counterflow flame. c) A 2-D laminar flame example: Temperature (left) and NO mass fraction (right) fields in a Premixed Slot Burner. From Maio et al. (2020).*

- *Mass conservation equation:*

$$\frac{\partial \rho}{\partial t} + \frac{\partial}{\partial x_i}(\rho u_i) = 0. \tag{2.19}$$

- *Momentum conservation equation:*

$$\rho \frac{\partial u_j}{\partial t} + \frac{\partial}{\partial x_i}(\rho u_i u_j) = -\frac{\partial P}{\partial x_j} + \frac{\partial \tau_{ij}}{\partial x_i}. \tag{2.20}$$

- *Energy conservation equation:*

$$\frac{\partial \rho e_t}{\partial t} + \frac{\partial}{\partial x_i}\left(\rho u_i e_t\right) = \frac{\partial}{\partial x_i}\left(\lambda \frac{\partial T}{\partial x_i} - \rho \sum_{k=1}^{N_s^M}\left(-D^v \frac{\partial Y_k^M}{\partial x_i}\right) h_k\right) + \frac{\partial}{\partial x_i}\left(\sigma_{ij} u_j\right) + \dot{Q}_r. \tag{2.21}$$

- *Species mass fraction conservation equation:*

$$\rho \frac{\partial Y_k^M}{\partial t} + \frac{\partial}{\partial x_i}\left(\rho u_i Y_k^M\right) = -\frac{\partial}{\partial x_i}\left(-\rho D^v \frac{\partial Y_k^M}{\partial x_i}\right) + \dot{\omega}_k^M. \tag{2.22}$$

- *Equation of state (perfect gas):*

$$P = \rho \frac{R}{\overline{W}} T. \tag{2.23}$$

Virtual pollutant sub-mechanism:

- *Species mass fraction conservation equation:*

$$\rho \frac{\partial Y_k^{S_p}}{\partial t} + \frac{\partial}{\partial x_i}\left(\rho u_i Y_k^{S_p}\right) = -\frac{\partial}{\partial x_i}\left(-\rho D^v \frac{\partial Y_k^{S_p}}{\partial x_i}\right) + \dot{\omega}_k^{S_p}. \tag{2.24}$$

In these equations the quantities with the superscript M correspond to the virtual main mechanism and S_p designates the virtual sub-mechanism of pollutant species p. e_t, P, ρ and u_i stand for the total energy, the pressure, the mixture density and the i^{th} component of the velocity, respectively. $\dot{Q}_r$ denotes the radiative source term. D^v is the molecular diffusion coefficient common to all virtual species (Eq. 2.13). $\dot{\omega}_k$ represents the chemical source term of the k^{th} species. σ_{ij} stands for the sum of a pressure and viscous tensor τ_{ij}, which are respectively written as:

$$\sigma_{ij} = -P\delta_{ij} + \tau_{ij}, \tag{2.25}$$

and

$$\tau_{ij} = \left(\kappa - \frac{2}{3}\mu\right)\frac{\partial u_l}{\partial x_l}\delta_{ij} + \mu\left(\frac{\partial u_i}{\partial x_j} + \frac{\partial u_j}{\partial x_i}\right), \tag{2.26}$$

where κ and μ stand for the volume viscosity and dynamic viscosity, respectively. δ_{ij} represent the Kronecker function, where $\delta_{ij} = 1$ if $i = j$, and $\delta_{ij} = 0$ otherwise.

A perfect gas assumption (Eq. 2.23) is made and is only used by the main virtual mechanism since is the responsible to reproduce the thermodynamics of the mixture properties.

Recalling the flow chart from Fig. 3.1: in a given time step the flame/flow solver calls Eqs. 2.19 to 2.23 using the main mechanism mixture properties and kinetics; and if the pollutant virtual scheme is ever activated, Eq. 2.24 is solved for all additional species in the virtual sub-mechanism.

2.6 Conclusion

Recent works of Cailler (2018) and Maio (2020) showed that the virtual chemistry is a very promising approach that could be introduced in turbulent flames for different configurations and combustion regimes, without making further assumptions in the model as it is done in other reduced kinetics models.
Due to the simplicity of the model, it is possible to retrieve flame characteristics at very low CPU cost, such as temperature, heat release and pollutant emission. CO and NOx predictions were previously studied and validated in several laminar and turbulent applications, demonstrating that virtual chemistry can retrieve very accurate results with such a reduced structure. Still, optimization of the virtual chemistry architecture should be addressed in order to well define the number of virtual species and virtual reactions that are necessary to well predict the flame characteristics at different time scales.
In the following chapters, the virtual chemistry approach will be adapted to sooting flames. The study will start with the adiabatic laminar flame condition, followed by the introduction of radiative heat losses in the sooting flame; both in a 1-D configuration. The second step will be to validate it in 2-D laminar flames in different theoretical and experimental configurations. Finally, the virtual soot and radiative models will be challenged in turbulent flames.

Chapter 3

Soot virtual chemistry in laminar flames

Contents

In the present chapter, a soot formation model based on the virtual chemistry approach is proposed for laminar hydrocarbon-air flames. A radiative model is also developed using the basics of virtual approach. The principles of the virtual approach are first introduced. The new virtual soot sub-mechanism and radiative models are derived for the virtual approach framework. The optimization set-up and strategy are then established. The new virtual models are validated in 1-D laminar flames and then challenged to 2-D laminar flames, for different flame configurations. Results are eventually compared to numerical and experimental data. The content of this chapter refers to an article submitted to "Combustion and Flame".

3.1 Introduction

The objective of this work is to develop a highly-reduced soot model for the prediction of the soot volume fraction, encompassing both the detailed soot precursor chemistry and the physics of particles dynamics interactions. For that purpose, we follow a methodology based on a recent approach called Virtual Chemistry, introduced by Cailler et al. (2017) to predict pollutants formation such as CO (Cailler et al. (2020); Maio et al. (2019)) or NOx (Maio et al. (2020)). The virtual chemistry method consists in building-up an optimized set of reduced virtual chemical reactions including virtual species. A machine learning algorithm is applied to retrieve a set of user-defined constraints such as the temperature profiles, the heat release or targeted pollutant mass fraction. Here we focus on the prediction of the soot volume fraction f_v. Predictions of the particle number density and the particle size distribution are not considered in this thesis.
The chapter is structured as follows. The virtual chemistry principle is presented in Section 3.2. An extension of the virtual approach is implemented to handle soot formation in laminar flames in Section 3.3. Also, a new procedure is developed in Section 3.4 in order to include radiative heat transfer in the computations. The optimization set-up of the virtual models and the computation cases are presented in Section 3.5. The virtual approach is then validated in 1-D premixed and non-premixed configurations in Section 3.6. Finally, the virtual chemistry formalism is challenged in a 2-D premixed slot burner and the 2-D non-premixed coflow burner from Santoro et al. (1983) in Section 3.7.

3.2 Virtual Chemistry principle

A virtual mechanism consist of virtual species and virtual reactions whose thermodynamic and chemical properties are optimized using machine learning algorithms in order to retrieve properties of reference flames gathered in a learning database (Cailler et al. (2017)). The virtual reactions between the virtual

species do not represent real chemical processes but form a mathematical architecture designed to reproduce user-specified targets such as temperature and mass fractions of combustion products and pollutant species.
A virtual scheme consists of a main block that models the heat release from the flame and sub-mechanisms dedicated to predict pollutants. Figure 3.1 depicts a schematic presentation of the approach. Virtual kinetic sub-mechanisms have so far been developed to predict pollutants such as carbon monoxide (CO, Cailler et al. (2020)) and nitrogen oxides (NOx, Maio et al. (2020)).

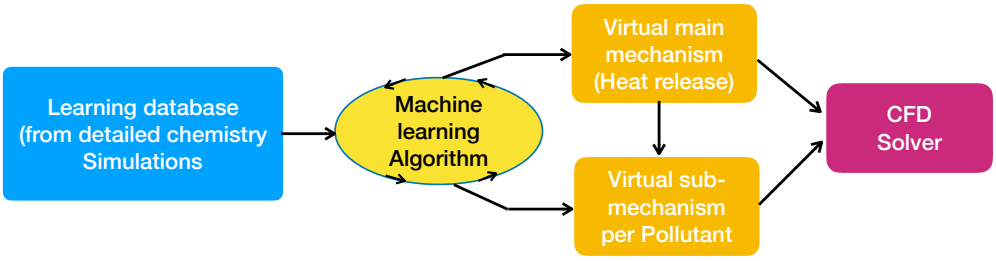

Figure 3.1: *Schematic presentation of virtual chemistry methodology.*

The virtual main mechanism structure presented in (Cailler et al. (2017); Cailler et al. (2020)) has shown that the following reaction scheme, composed of 8 virtual species and 2 virtual reactions, accurately captures the heat release and the flame temperature for a wide range of fuel compositions:

$$\alpha^M_{F,1} F + \alpha^M_{Ox,1} Ox + \alpha^M_{D,1} D \rightarrow \alpha^M_{I,1} I + \alpha^M_{D,1} D \qquad (R^M_1)$$

$$I \rightarrow \sum_{k=1}^{N^M_P=4} \alpha^M_{P_{k,2}} P_k \qquad (R^M_2)$$

In this mechanism, F represents the fuel, Ox the oxidizer, D the inert dilutant species, I a virtual intermediate species and P_k the virtual products. $\alpha^M_{k,r}$ is the stoichiometric coefficient per unit mass of the k^{th} virtual species in the r^{th} virtual reaction, and N^M_P is the number of virtual products. The superscript M stands for virtual main chemistry. The vector of thermochemical parameters χ^M (see Appendix A.2) of the main mechanism is optimized through the evolutionary algorithm proposed by Cailler et al. (2017).
Thermodynamic and transport properties of the virtual species as well as specific gas constants are calibrated, using a machine learning algorithm, to recover averaged properties of the multi-component real mixture.

3.3 Virtual soot sub-mechanism

3.3.1 Scheme architecture

As shown in Fig. 3.2(top), a classical soot model requires first a fine description of the detailed chemistry leading to the soot precursor formation (C_2H_2, PAHs, etc.) (Saggese et al. (2015)). Then, the formation of the particles is described though a one-precursor (C_2H_2 or PAH) nucleation model (Leung et al. (1991); Schuetz and Frenklach (2002)) or multiple-PAHs approach (Saggese et al. (2015); Selvaraj et al. (2016)). Some approaches consider that PAHs grow until they reach an intermediate state, called dimer, between the gas and solid phases (Blanquart and Pitsch (2007); Mueller et al. (2009b)). Finally, the solid phase is modeled employing dedicated particles interaction and distribution formalisms such as for instance sectional (Rodrigues et al. (2018)) or MOMs (Mueller et al. (2009b)) approaches. These successive modeling stages lead to the prediction of the soot characteristics such as volume fraction, particle number density and particle size distribution.
Most of chemical reduction methods, such as tabulated (Fiorina et al. (2005)) or analytically-reduced (Pepiot (2008)) approaches, are limited to the gas-phase kinetics. The description of the solid phase, based on classical approaches, remains very time consuming. The virtual soot sub-mechanism proposed in the present work (Fig. 3.2 bottom) has the advantage of reducing the overall process by targeting only the final quantities of interest.
Here we focus on the soot volume fraction f_v^s as a target. For that purpose, soot particles are represented by a virtual chemical species $\mathcal{S}$. The following chemical structure is proposed to predict the formation of the virtual soot species $\mathcal{S}$:

$$\alpha^s_{F,1}F + \alpha^s_{Ox,1}Ox \rightarrow \alpha^s_{V_1,1}V_1 + \alpha^s_{V_3,1}V_3 \qquad (R^s_1)$$

$$V_1 \rightarrow \alpha^s_{\mathcal{S},2}\mathcal{S} + \alpha^s_{V_2,2}V_2 \qquad (R^s_2)$$

$$\mathcal{S} + V_1 + V_2 \rightarrow \alpha^s_{\mathcal{S},3}\mathcal{S} + \alpha^s_{V_3,3}V_3 \qquad (R^s_3)$$

$$\mathcal{S} + Ox + V_2 \rightarrow Ox + 2V_3 \qquad (R^s_4)$$

where V_1, V_2 and V_3 are three virtual species and $\alpha^s_{k,r}$ is the stoichiometric coefficient per unit mass of the k^{th} virtual species in the r^{th} virtual reaction. The superscript s stands for virtual soot sub-mechanism.
The soot production is initiated by reaction R^s_1. The rate of progress of this reaction must be equal to that of reaction R^M_1 in order to be consistent with the

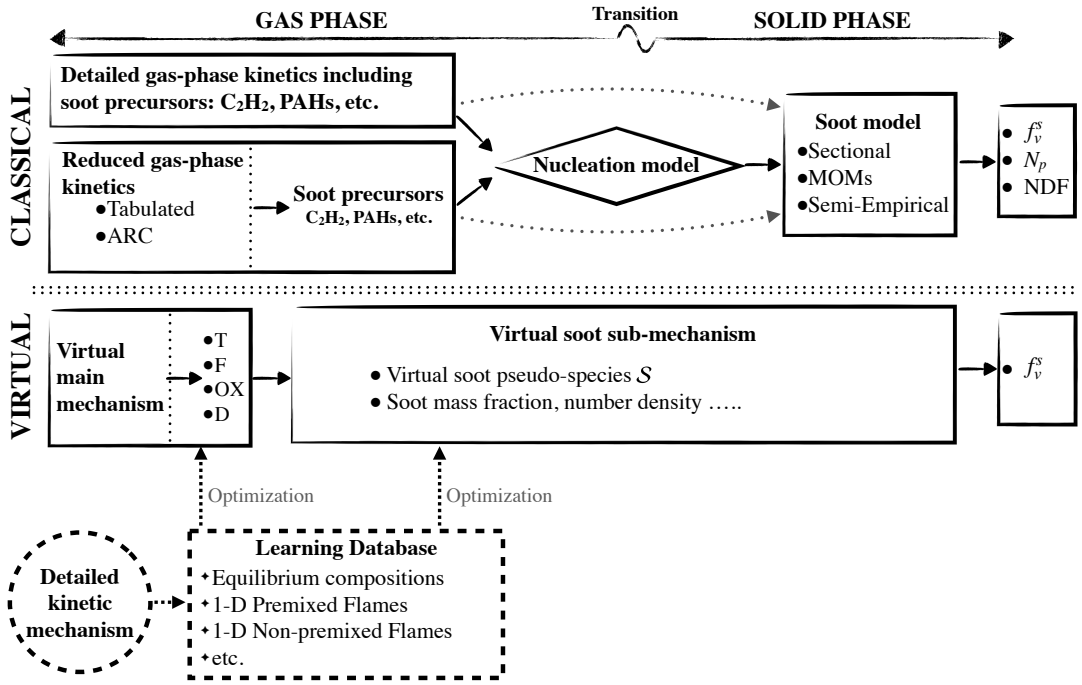

Figure 3.2: *Diagram soot formation models; top: Current Models, bottom: Virtual Chemistry concept.*

fuel oxidation through the main virtual mechanism. The three virtual species V_1, V_2 and V_3 together with virtual reactions R_2^s, R_3^s and R_4^s represent the nucleation, surface growth and coagulation, and oxidation of soot particles. This approach encompasses all the mechanisms of soot formation in both gas and solid phases, without modeling individually each physical step.

3.3.2 Kinetic parameters optimization

The virtual soot sub-mechanism reaction rates of reactions R_1^s through R_4^s are expressed as follows:

$$q_1^s = [F]^{n_{F,1}^s}[Ox]^{n_{Ox,1}^s} A_1^s(Z) \exp\left(-\frac{E_{a,1}^s}{RT}\right), \tag{3.1}$$

$$q_2^s = [V_1]^{n_{V_1,2}^s} A_2^s(Z) \exp\left(-\frac{E_{a,2}^s}{RT}\right), \tag{3.2}$$

$$q_3^s = [\mathcal{S}]^{n_{\mathcal{S},3}^s(Z)}[V_1]^{n_{V_1,3}^s}[V_2]^{n_{V_2,3}^s(Z)} A_3^s(Z) \exp\left(-\frac{E_{a,3}^s}{RT}\right), \tag{3.3}$$

$$q_4^s = [\mathcal{S}]^{n^s_{\mathcal{S},4}}[Ox]^{n^s_{Ox,4}}[V_2]^{n^s_{V_2,4}} A_4^s(Z) T^{\beta_4^s} \exp\left(-\frac{E^s_{a,4}}{RT}\right), \tag{3.4}$$

where $E^s_{a,r}$ is the the activation energy, A^s_r is the pre-exponential constant, $n^s_{k,r}$ is the order of species k in reaction r, and β^s_r is the temperature dependence exponent. $\varphi(Z)$ indicates a dependence on the mixture fraction Z, which is defined as:

$$Z = \frac{Y^s_D - Y^s_D|^{Ox}}{Y^s_D|^F - Y^s_D|^{Ox}} \tag{3.5}$$

where Y^s_D is the dilutant mass fraction and $|^{Ox}$ (respectively $|^F$) stands for pure oxidizer (respectively pure fuel) condition. As previously mentioned, kinetic rate parameters of Eq. 3.1 are given by the first reaction R_1^M of the main mechanism, *i.e.* $A^s_1 = A^M_1$, $E^s_{a,1} = E^M_{a,1}$, $n^s_{F,1} = n^M_{F,1}$, $\alpha^s_{F,1} = \alpha^M_{F,1}$, $\alpha^s_{Ox,1} = \alpha^M_{Ox,1}$ and $n^s_{Ox,1} = n^M_{Ox,1}$.

The ensemble of virtual chemical parameters of the virtual soot sub-mechanism constitutes a vector $\chi^s = \{A^s_r, E^s_{a,r}, \alpha^s_{k,r}, n^s_{k,r}, \beta^s_4\}$ to be optimized. Also, the mass conservation imposes: $\alpha^s_{V_1,1} + \alpha^s_{V_3,1} = 1$, $\alpha^s_{\mathcal{S},2} + \alpha^s_{V_2,2} = 1$ and $\alpha^s_{\mathcal{S},3} + \alpha^s_{V_3,3} = 3$. Finally, in order to enhance the capacity of prediction of the virtual mechanism in a wide range of operating conditions, the dependence on the mixture fraction Z is established for some elements of χ^s, as it was made for previous pollutant virtual models (Cailler et al. (2020); Maio et al. (2020)), such as A^s_r (for all reactions), $n^s_{\mathcal{S},3}(Z)$ and $\alpha^s_{\mathcal{S},3}(Z)$.

The kinetic parameters in vector χ^s are optimized by minimizing the following cost function:

$$\mathcal{C}^s(\chi^s) = \sum_{i=1}^{N_c} \left(w_s \frac{\left\| f^s_{v,i} - f^d_{v,i} \right\|_{L_2}}{\left\| f^d_{v,i} \right\|_{L_2}} + (1 - w_s) \frac{\left\| \mathrm{grad} f^s_{v,i} - \mathrm{grad} f^d_{v,i} \right\|_{L_2}}{\left\| \mathrm{grad} f^d_{v,i} \right\|_{L_2}} \right), \tag{3.6}$$

where $f^s_{v,i}$ and $f^d_{v,i}$ are the soot volume fraction profiles of the i^{th} flame solution (out of N_c flame solutions in the learning database), respectively computed with virtual and detailed reference chemistries. The superscript d stands for reference detailed chemistry solutions. N_c is the number of 1-D reference flame solutions which constitute the learning database. The weight w_s is set to 0.9, which is close to what is used in the virtual main mechanism (Cailler et al. (2020)).

The soot volume fraction f^s_v is calculated from the virtual soot mass fraction $Y^s_{\mathcal{S}}$:

$$f^s_v = \frac{\rho}{\rho_s} Y^s_{\mathcal{S}} \tag{3.7}$$

where ρ is the gaseous mixture density, and ρ_s is the soot density considered constant, ρ_s =1800 kg m^{-3}.

3.4 A new virtual model for radiative heat transfer

Radiative heat transfer in the gas phase may significantly impact the heat release and the flame temperature. To account for this phenomenon, radiative gas properties of the reactive flow must also be included in the optimization process of the virtual main mechanism. These properties depend on gas temperature and mixture composition (Barlow et al. (2001)). For sooting flames, the Planck mean absorption coefficient κ_{Planck} can be decomposed as $\kappa_{\text{Planck}} = \kappa_{\text{gas}} + \kappa_{\text{soot}}$ (Modest (2013)), where κ_{gas} and κ_{soot} correspond to gas and solid phases, respectively.

3.4.1 Gas radiation model: virtual approach

Here, the proposed virtual radiation model for the gas phase uses the following polynomial expression for the gaseous Planck mean absorption coefficient κ^M_{gas} as in Barlow et al. (2001):

$$\begin{aligned}\kappa^M_{\text{gas}}(Z,T) &= \gamma^M_0(Z) + \gamma^M_1(Z)(1000/T) + \gamma^M_2(Z)(1000/T)^2 \\ &+ \gamma^M_3(Z)(1000/T)^3 + \gamma^M_4(Z)(1000/T)^4 + \gamma^M_5(Z)(1000/T)^5,\end{aligned} \tag{3.8}$$

where the polynomial coefficients $\gamma^M_l(Z)$ are to be optimized, in order to retrieve solutions of canonical combustion configurations, which include radiation heat transfer.
The vector of thermochemical parameters χ^M of the main mechanism along with the vector of coefficients $\Gamma^M = (\gamma^M_0, \gamma^M_1, \dots \gamma^M_5)$ are optimized through the evolutionary algorithm proposed by Cailler et al. (2017). The optimization procedure consists in minimizing the following cost function:

$$\mathcal{C}^M(\chi^M, \Gamma^M) = \sum_{i=1}^{N_c} \left| \psi^M_i - \psi^d_i \right|, \tag{3.9}$$

where N_c is the number of flame elements included in the learning database. ψ^M_i and ψ^d_i are respectively the virtual and the targeted reference flame properties, such as mixture equilibrium conditions and flame speed and temperature, retained for the optimization (Cailler et al. (2017)).

3.4.2 Soot particles radiation model

The Planck soot absorption coefficient κ^v_{soot} is expressed from the soot volume fraction f^s_v predicted by the virtual soot sub-mechanism and the gas temperature T given by the main mechanism:

$$\kappa^v_{\text{soot}} = \alpha f^s_v T, \tag{3.10}$$

where α is a modeling constant set to 1302 $\text{m}^{-1}\text{K}^{-1}$ as in Modest (2013).

3.5 Virtual schemes optimization set-up

3.5.1 Learning database and virtual scheme optimization

The reference flame database is generated using the detailed soot kinetics model proposed by the CRECK Modeling Group (Saggese et al. (2015)) which consists of 16797 reactions and 297 species. Among these species, 20 lumped pseudo-species called "BIN" are considered. BIN_1 through BIN_4 correspond to heavy PAHs with 20, 40, 80 and 160 carbon atoms respectively. The nascent soot particles are classified as BIN_5 and they grow from spherical shape (BIN_5 to BIN_{11}) until they take an aggregate form (BIN_{12} to BIN_{20}) (Saggese et al. (2015)). This kinetic mechanism has been extensively validated on several experimental data in many different systems (Saggese et al. (2015); Pejpichestakul et al. (2019); Pejpichestakul et al. (2019)). This mechanism is used here for all detailed chemistry ethylene-air combustion simulations. Radiative heat losses are calculated using the optically-thin narrow-band radiation model based on Soufiani and Taine (1987), which is included in REGATH package (Darabiha and Candel (1992)). The reference soot volume fraction is defined from the detailed chemistry flame solutions as $f_v^d = (\rho/\rho_s)Y_{soot}^d$, where $Y_{soot}^d = \sum_i Y_{\mathrm{BIN}_i}$ for $i = 5, 6, \ldots, 20$ (Saggese et al. (2015)).

The virtual main mechanism is trained by employing the genetic algorithm detailed in Cailler et al. (2020). The reference flame solutions, used to evaluate the cost function given by Eq. 3.9, comprise 1-D freely-propagating laminar premixed flames including radiative heat transfer for a range of equivalence ratios covering the flammability limits ($\phi = 0.5$ and $\phi = 3.0$). It has been shown in (Cailler et al. (2017); Cailler et al. (2020)) that this learning database is sufficiently large to recover heat release and temperature in both premixed and non-premixed flame regimes. To account for multi-mode combustion in the virtual soot sub-mechanism, the learning database is made of both 1-D freely-propagating premixed flames and 1-D counterflow non-premixed flames as in Maio et al. (2020). The targeted premixed flames cover equivalence ratios from $\phi = 1.8$ to $\phi = 2.8$ at atmospheric pressure and initial temperature of 298 K. Non-premixed flames, where pure ethylene at 298 K is injected against air at 298 K, cover strain rates from $a = 6s^{-1}$ to $a = 95s^{-1}$. The total number of operating conditions N_c in the database is $N_c = N_c^{\mathrm{fpf}} + N_c^{\mathrm{cf}} = 17$, where $N_c^{\mathrm{fpf}} = 11$ and $N_c^{\mathrm{cf}} = 6$ are the number of premixed and counterflow target flames in the learning database, respectively. Table 3.1 summarizes the different operating conditions of 1-D premixed and non-premixed ethylene-air flames included in the learning database.

All detailed chemistry simulations include thermophoretic effects for all species BIN_5 to BIN_{20}. Unity Lewis number is assumed for virtual species present in the main and virtual mechanisms excepted for the virtual soot species $\mathcal{S}$ for which $\mathrm{Le}_{\mathcal{S}} = 25$ is considered. This value is estimated by averaging the Lewis number of BINs found in the detailed mechanism. See Appendix A.1 for more

Virtual scheme	Reference archetype	Operating condition
Main mechanism	Adiabatic and Radiative premixed flames	$\phi = \{0.5, \cdots, 3.0\}$; $\Delta\phi = 0.1$
Soot sub-mechanism	Adiabatic and Radiative premixed and non-premixed flames	$\phi = \{1.8, \cdots, 2.8\}$; $\Delta\phi = 0.1$ $a = \{6, 10, 25, 45, 60, 95\}$ s^{-1}

Table 3.1: *List of operating conditions of 1-D flames included in the learning database.*

details.
All flame calculations, with both detailed and virtual chemistries, are performed with the REGATH package (Darabiha and Candel (1992)). The optimized reaction rate parameters to account for premixed and non-premixed flames in the virtual soot sub-mechanism are given in Appendix A.2.

3.5.2 Computed cases

The virtual mechanisms and radiation models are now challenged on 1-D and 2-D ethylene-air flames. The following series of computations are performed:

- D-A: Adiabatic flames using the detailed CRECK mechanism (Saggese et al. (2015));
- D-R: Non-adiabatic flames using the detailed CRECK mechanism (Saggese et al. (2015)). Only gas radiation is considered using the narrow-band radiation model based on Soufiani and Taine (1987) for 1-D configurations, and on that of Barlow et al. (2001) for 2-D configurations;
- D-Rs: Non-adiabatic flames using the detailed CRECK mechanism (Saggese et al. (2015)). Gas radiation is modeled as in the case D-R, whereas solid phase radiation is modeled using Eq. 3.10;
- V-A: Adiabatic flames using the developed virtual mechanisms;
- V-R: Non-adiabatic flames using the the virtual mechanism. Only gas radiation is considered;
- V-Rs: Non-adiabatic flames using the the virtual mechanism. Both gas and particle radiation are considered.

Table 3.2 summarizes the computed cases, indicating the kinetic model and radiative effects involved.

Computed case	D-A	D-R	D-Rs	V-A	V-R	V-Rs
Kinetic model	Detailed mechanism			Virtual mechanism		
Adiabatic	√	–	–	√	–	–
Gas radiation	–	√	√	–	√	√
Soot radiation	–	–	√	–	–	√

Table 3.2: *Summary of computed cases. Kinetic model and radiative effects involved are indicated.*

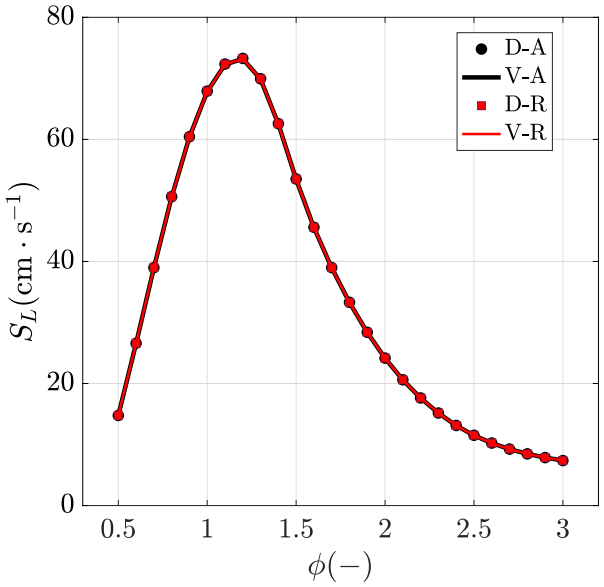

Figure 3.3: *Evolution of the laminar flame speed of 1-D premixed ethylene-air flames ($P = 1$ atm, $T_0 = 298$ K): comparison between the four cases D-A, D-R, V-A, V-R.*

3.6 1-D laminar ethylene-air flame computations

3.6.1 Validation of virtual main mechanism

3.6.1.1 1-D freely-propagating premixed flames

Simulations of 1-D freely-propagating premixed ethylene-air flames are first conducted. The laminar consumption speed S_L is plotted in Fig. 3.3 as a function of the equivalence ratio ϕ. The virtual approach predicts very well the flame speed in all conditions. As the radiative heat losses take place essentially in hot gases, the flame front and the flame speed S_L are not affected by radiation. Figure 3.4 presents temperature profiles obtained at $\phi = 2.3$ for four cases D-A, D-R, V-A, and V-R. Both the adiabatic and non-adiabatic virtual mechanisms

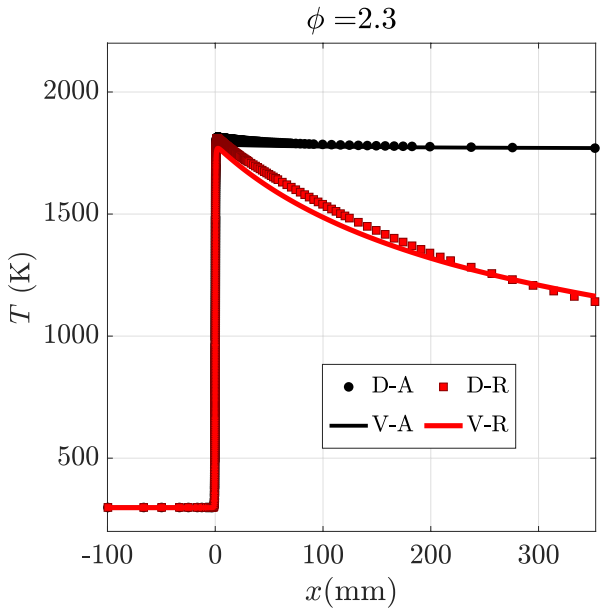

Figure 3.4: *Impact of radiative heat losses on temperature profile in a 1-D freely-propagating premixed ethylene-air flame ($\phi = 2.3$): comparison between the four cases D-A, D-R, V-A, V-R*

reproduce very well the reference temperature profiles. The impact of radiation on the temperature, especially visible for long distances (long residence times), is well captured by the virtual chemistry and radiation models.

3.6.1.2 1-D non-premixed counterflow flames

The gas phase virtual radiative model is validated in this section for non-premixed flames. Four series of 1-D ethylene-air counterflow flames are computed at different strain rates a again for the four conditions D-A, D-R, V-A, and V-R. Figure 3.5 illustrates the evolution of the maximum flame temperature with the strain rate. In both adiabatic and radiative cases, the virtual main chemistry and virtual radiative models predict very well this evolution for a very wide range of strain rates, from equilibrium up to quenching conditions. As expected, the influence of radiation on the maximum flame temperature is evidenced for very low strain rates.

3.6.2 Validation of soot virtual sub-mechanism and virtual radiative model

3.6.2.1 1-D freely-propagating premixed flames

Temperature and soot volume fraction profiles are shown in Fig. 3.6 for equivalence ratios equal to 2.1 and 2.4, respectively. Solutions are plotted for the six

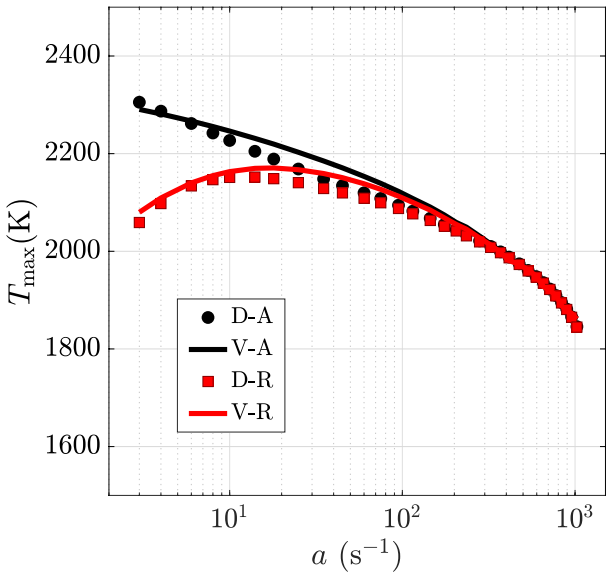

Figure 3.5: *Evolution of the maximum temperature $T_{\max}$ with the strain rate a in 1-D non-premixed ethylene-air counterflow flames: comparison between the four cases D-A, D-R, V-A, V-R.*

simulation cases D-A, D-R, D-Rs, V-A, V-R and V-Rs.
Again, for both $\phi = 2.1$ and $\phi = 2.4$, comparisons between D-A/V-A and D-R/V-R results in Fig. 3.6 (top) show that the virtual main mechanism accurately captures the temperature profiles with and without considering gas radiation. The soot volume fraction profiles, plotted in Fig. 3.6 (bottom) are also very well predicted by the virtual soot sub-mechanism for these operating conditions. The soot production, enhanced by radiative heat transfer, also significantly increases by more than 2 orders of magnitude between $\phi = 2.1$ and $\phi = 2.4$.
The influence of solid phase radiation on temperature is only significant for $\phi = 2.4$, where the soot volume fraction is high enough (cases D-Rs and V-Rs). The virtual model which includes both gas and solid particles radiation predicts very well the temperature and soot reference solutions.

3.6.2.2 1-D non-premixed counterflow flames

Figure 3.7 presents temperature and soot volume fraction profiles for an adiabatic 1-D non-premixed counterflow flame (strain rate $a = 10$ s^{-1}) computed with both detailed (D-A) and virtual (V-A) chemistry approaches. Pure ethylene is injected from right while air is injected from left. Soot formation takes place in a rich region located between the maximal flame temperature position ($x = -4$mm) and the stagnation plane ($x = 0$). The soot volume fraction is

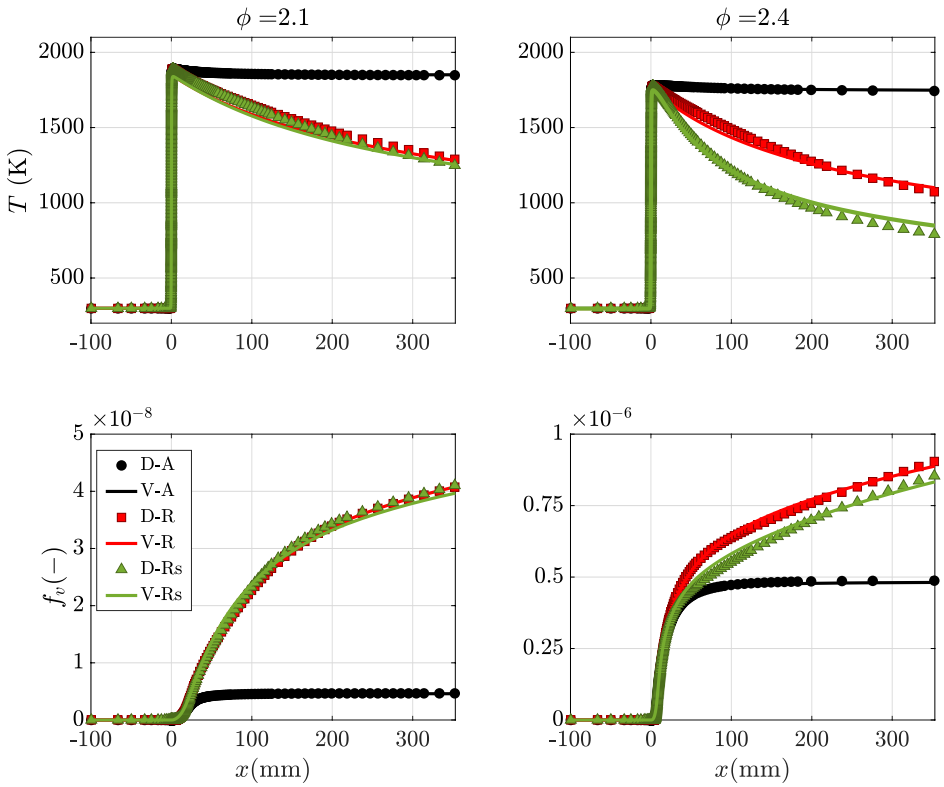

Figure 3.6: *Temperature (top) and soot volume fraction (bottom) profiles of premixed ethylene-air flames, with and without considering solid particle radiation for different equivalence ratios ϕ: comparison between the six cases:D-A, D-R, D-Rs, V-A, V-R, V-Rs.*

well predicted by the virtual soot sub-model trained to capture both premixed and non premixed flame archetypes as indicated on Table 3.1.
It is interesting to focus on the dashed-dotted profile that shows the soot volume fraction profile obtained with a virtual scheme sub-mechanism (V-A-Prem.) trained to target only 1-D premixed flames. The target premixed flames are accessible only within the flammability limits, highlighted by the grey area in Fig 3.7. The peak of the soot volume fraction is located at the rich side of the grey zone. It can be seen that such target flame is unable to capture the soot produced here beyond the rich extinction limit.
As indicated in Sec. 3.5.1, the virtual scheme used in case V-A has been optimized with a Lewis number of species $\mathcal{S}$ set to $\mathrm{Le}_{\mathcal{S}} = 25$ whereas Le=1 has been assumed for all other virtual species. As soot particles diffusion is very small compared to gaseous species, assuming unity Lewis also for the soot would have been unrealistic. This is illustrated in Fig. 3.8 where the solution obtained with Le=1 for all species considerably underestimates the soot production.
Finally, the evolution of maximum temperature $T^{\max}$ and maximum soot vol-

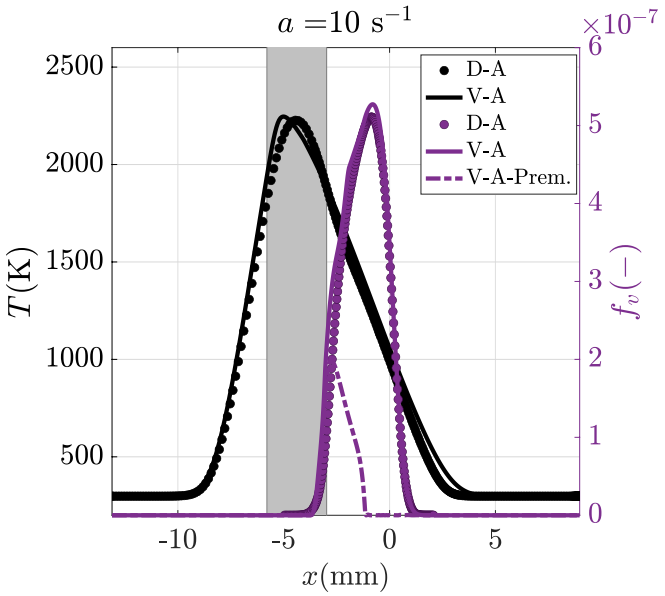

Figure 3.7: *Temperature and soot volume fraction profiles of adiabatic and non-adiabatic 1-D non-premixed counterflow flame using detailed and virtual models, cases D-A and V-A. Soot volume fraction profile obtained by a virtual soot sub-mechanism optimized on a learning database including only 1-D premixed flames (V-A-Prem.) is also plotted. The region covered by the learning database of only 1-D premixed flames within the extinction limits is shown by the grey area.*

ume fraction $f_v^{\max}$ as a function of strain rate a are presented in Fig. 3.9 for adiabatic simulation cases D-A and V-A as well as non-adiabatic cases D-Rs and V-Rs including both gaseous and solid phases radiative heat losses. The virtual soot sub-mechanism predicts well the soot volume fraction maximum value $f_v^{\max}$ of 1-D counterflow ethylene-air flames for a large range of strain rates a.

3.6.3 Application of virtual chemistry to burner-stabilized flames

The reduced chemistry approach is now applied to a burner-stabilized ethylene-air flame studied within the International Sooting Flame (ISF) Workshop (ISF5 (2021)). Two equivalence ratio of $\phi = 2.34$ and $\phi = 2.64$ are investigated at atmospheric pressure and temperature of $T = 298$ K. Simulations are conducted by imposing at the inlet the fresh gases injection velocity measured in experiments (Menon et al. (2007); Xu et al. (1997)) (6.73 cm·s^{-1}). Figure 3.10 (top) show that for both detailed and virtual radiative simulations, numerical prediction of temperature agrees very well with experimental measurements (Menon et al. (2007)). Soot volume fraction profiles plotted in Fig. 3.10 (bottom), exhibit also a fair agreement between simulations and experimental data. Therefore, even if burner-stabilized flames where not included in the learning

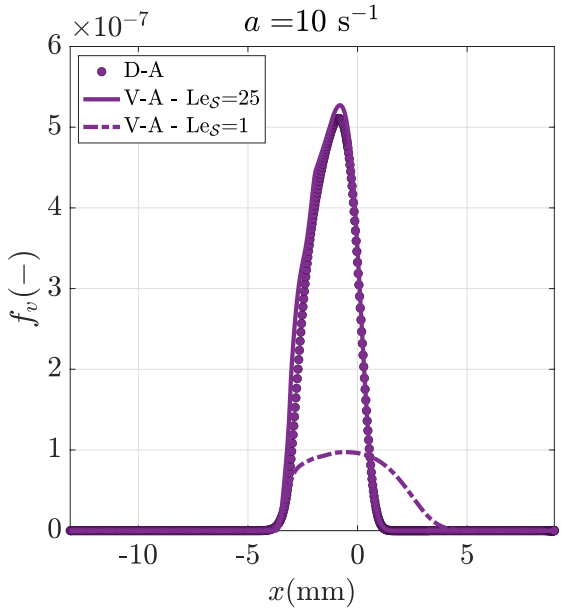

Figure 3.8: *Influence of the virtual soot species $\mathcal{S}$ Lewis number, Le$_{\mathcal{S}}$, on soot formation in a counterflow ethylene-air flame.*

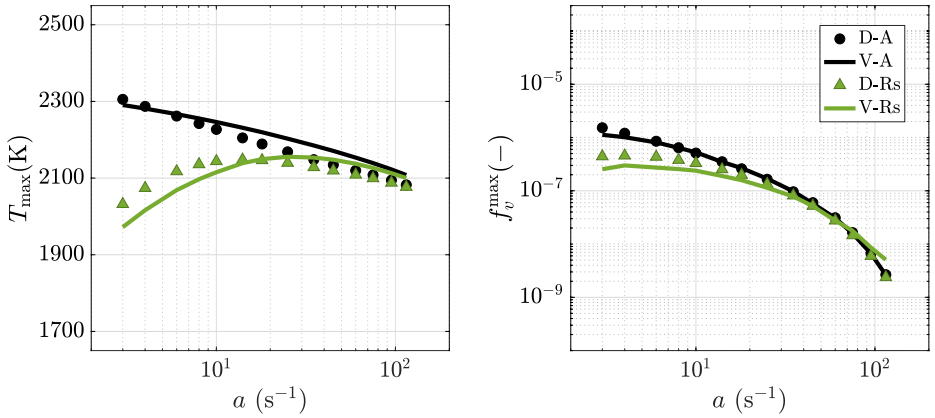

Figure 3.9: *Evolution of the maximum temperature $T^{\max}$ (left), and maximum soot volume fraction $f_v^{\max}$ (right) as a function of strain rate a in 1-D counterflow non-premixed ethylene-air flames: comparison between for the four cases D-A, V-A, D-Rs, and V-Rs.*

database, the virtual chemistry is able to capture their chemical structure.

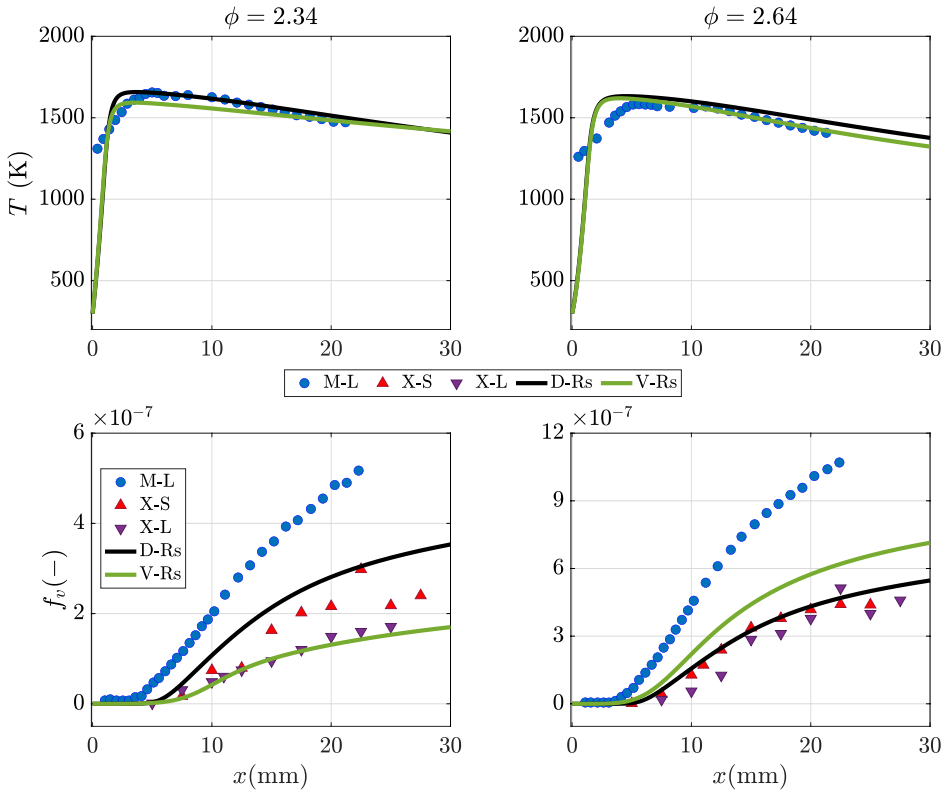

Figure 3.10: *Burner-stabilized premixed ethylene-air flames for $\phi = 2.34$ and $\phi = 2.64$. Comparison of numerical results (D-Rs and V-Rs) of temperature (top) and soot volume fraction (bottom) profiles against experiments; (M-L) Menon et al. (2007) and (X-S, X-L) Xu et al. (1997).*

3.7 Application of virtual chemistry to 2-D laminar flames

3.7.1 2-D laminar ethylene-air premixed slot burner

The geometry of the premixed slot burner is shown in Fig. 3.11. The domain is long enough to allow soot formation. The cell size in the flame front are $\Delta_x \sim 0.03$ mm, leading to 15-20 cells across the thermal layer.
Boundary conditions are indicated in Fig. 3.11. The burner walls are adiabatic. The computation is carried out on half of the domain because of the symmetric geometry of the burner. Symmetry is also assumed for outer lateral boundary conditions. Ethylene-air mixture with equivalence ratio of $\phi = 2.5$ at $T = 298$ K and $p = 1$ atm is injected at the inlet. A parabolic axial velocity distribution, with mean axial velocity $u_m = 30$ cm $\cdot$ s^{-1}, is imposed to mimic a fully-developed channel flow. The six numerical cases presented in Sec. 3.5.2 are computed. Simulations are carried out with the laminarSMOKE

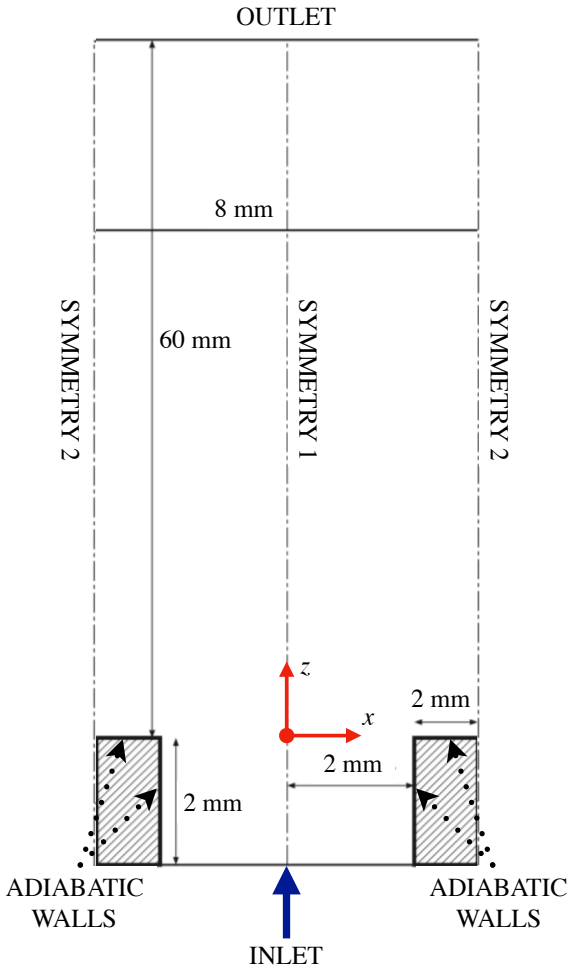

Figure 3.11: *Premixed slot burner: geometry of the numerical setup used in simulations.*

package (Cuoci et al. (2013b); Cuoci et al. (2013a)) based on the OpenFOAM framework, designed to handle arbitrarily complex kinetic mechanisms.
Figure 3.12 compares the virtual soot sub-mechanism (case V-R) and the detailed model (case D-R) results. The analysis of predicted temperature fields shows the ability of the virtual chemistry to capture accurately the flame position. A good agreement is also observed on the soot volume fraction fields. Temperature and soot volume fraction profiles along the centerline are plotted in Fig. 3.13 for the six simulation cases D-A, D-R, D-Rs, V-A, V-R and V-Rs. All temperature profiles show very good agreement with the detailed chemistry simulations. Heat losses are fairly captured by the virtual radiation model. The soot volume fraction profiles are also well predicted by the three approaches. When radiative effects are included, earlier soot inception is observed as in 1-D

flames results.

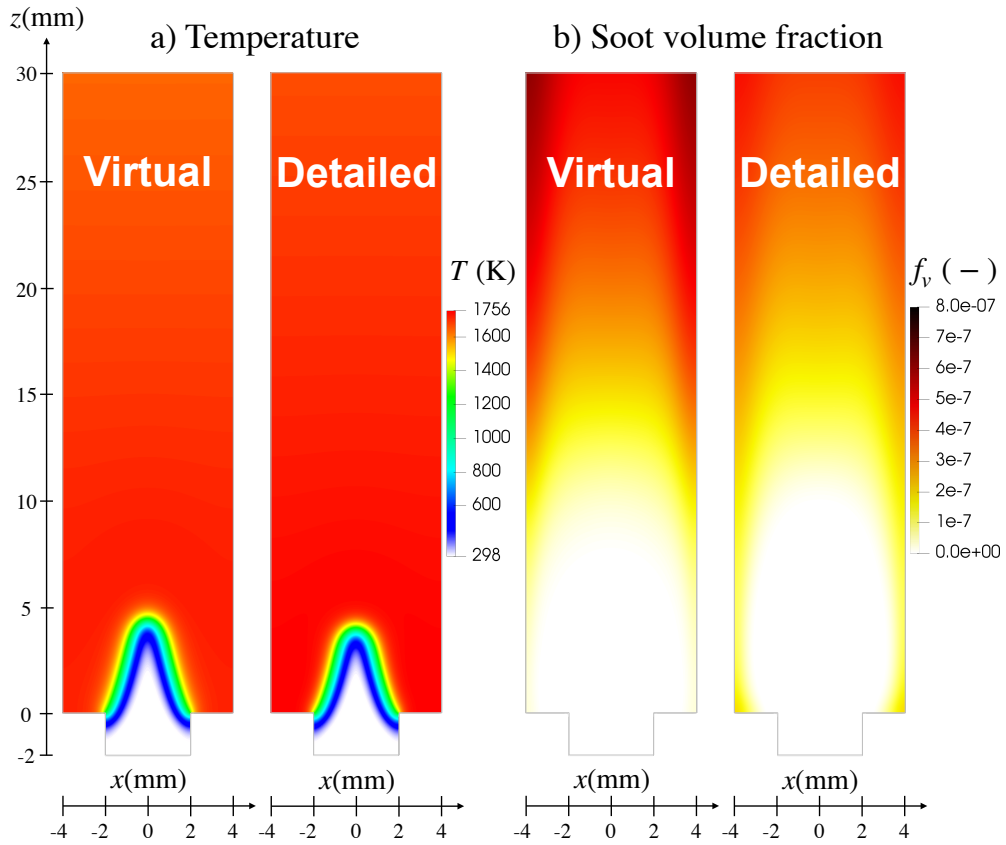

Figure 3.12: *Premixed Slot Burner: comparison of a) temperature and b) soot volume fraction fields using the virtual and detailed models, case V-R (left) and case D-R (right).*

A computing time analysis, without accounting for radiative heat transfers, shows that the virtual chemistry computation including both main and soot mechanisms (12 species and 6 reactions) is about $\mathcal{C}_t = 2100$ times faster than the detailed mechanism calculations (297 species and 16797 reactions). This value is consistent with the speed-up factor found by Maio et al. (2020).

3.7.2 2-D laminar Santoro Coflow Burner

The non-premixed flame experimentally studied by Santoro et al. (1983) is now computed with the virtual soot model. The burner consists of a central pipe fed with pure ethylene surrounded by a concentric tube for air injection. The fuel and air flow rates are 3.85 $cm^3 \cdot s^{-1}$ and 713.3 $cm^3 \cdot s^{-1}$, respectively. Further details on the experimental setup are given in (Santoro et al. (1983).) The 2-D numerical domain is 152 mm long and 47.5 mm wide. Following ISF recommendations (ISF5 (2021)), symmetry condition is retained at the

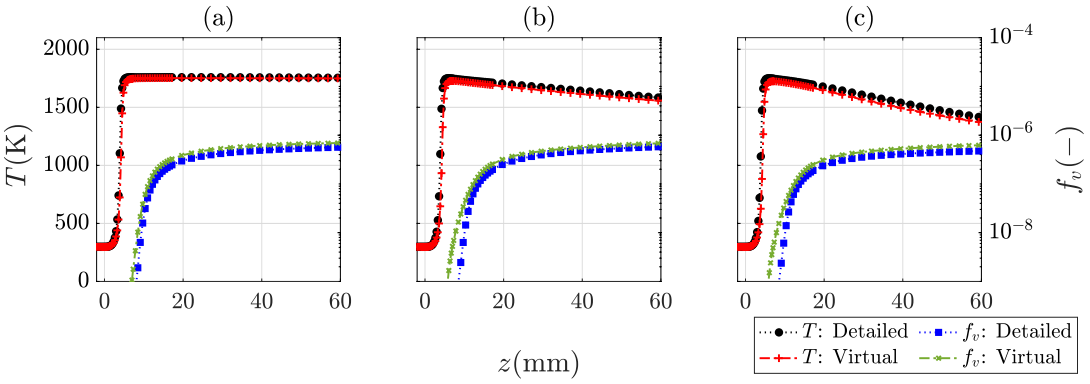

Figure 3.13: *Premixed Slot Burner: Temperature and soot volume fraction profiles along the centerline. Comparison of simulation (a) between cases D-A and V-A, (b) between cases D-R and V-R, and (c) between cases D-Rs and V-Rs.*

centerline and slip walls are prescribed for the outer lateral boundary. The cartesian grid is made of 26270 cells with a characteristic size of $\Delta_x \sim 0.075$ mm in the flame region, close to values used in Bodor et al. (2019). The inlet fuel velocity follows a parabolic distribution adapted to fully-developed flow with a mean velocity $u_m^{\text{fuel}} = 3.98\ \text{cm} \cdot \text{s}^{-1}$. Constant velocity $u_m^{\text{coflow}} = 8.9\ \text{cm} \cdot \text{s}^{-1}$ is prescribed at the air inlet. Both fuel and air are injected at $T = 298$ K. The inner tube wall temperature is imposed at $T = 350$ K. Simulations are carried out with the laminarSMOKE package (Cuoci et al. (2013b); Cuoci et al. (2013a)) based on the OpenFOAM framework.

The virtual chemistry simulation includes both gas and solid phases radiation phenomena (V-Rs), which are both significant in this configuration (Santoro et al. (1987)). 2-D iso-contour of temperature and soot volume fraction fields are shown in Fig. 3.14.

Temperature radial profiles are plotted in Fig. 3.15, for two heights above the burner at $z = 10$ mm and 50 mm. Numerical results using the virtual models (V-Rs) are in very good agreement with experimental data from Santoro et al. (1987). Virtual non-adiabatic (V-Rs) simulation results display similar precision to detailed simulation (D-Rs) results.

Soot volume fraction profiles are illustrated in Fig. 3.16, for two heights above the burner $z = 15$ mm and 50 mm. Comparing to the experimental measurements from ISF5 (2021), both virtual (V-Rs) and detailed (D-Rs) non-adiabatic models predict well the soot peak positions at both heights. The peak values predicted by the virtual model are close to those obtained by the detailed simulation. However, both results underpredict the maximum value of soot volume fraction (f_v): about half the maximum value at $z = 15$ mm, and about one eighth at $z = 50$ mm. Discrepancies are therefore due mainly to the detailed mechanism and not to the virtual chemistry reduction method.

Radially-integrated soot volume fraction, defined as $F_v(z) = \int_r 2\pi f_v(r,z) r dr$,

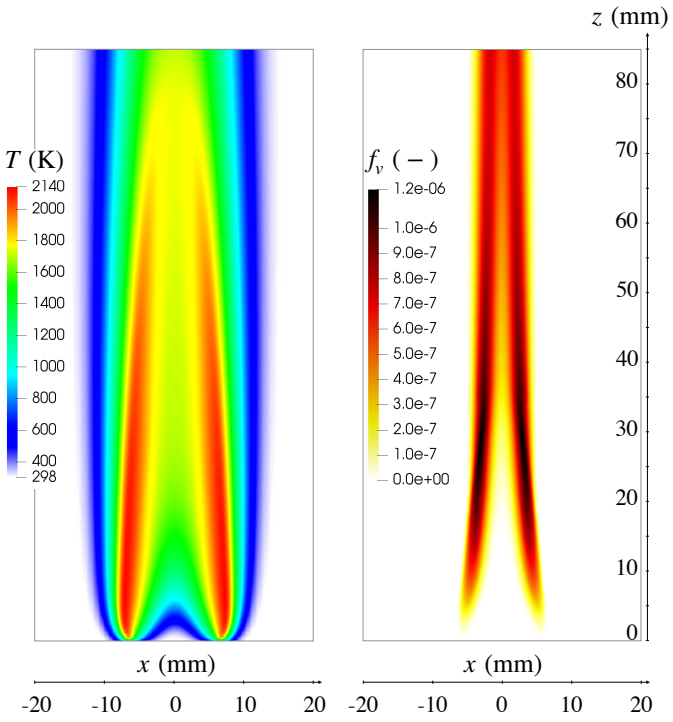

Figure 3.14: *Santoro Coflow Flame: Temperature (left) and soot volume fraction (right) fields using the virtual chemistry and radiative models.*

profiles along the centerline are compared against experiments in Fig 3.17. In addition to D-Rs solutions, detailed chemistry solutions obtained by other groups are also indicated. Simulation results of Blacha et al. (2012) have been obtained using a detailed chemistry mechanism including 71 species and 803 reactions. Soot particles distribution has been modeled with a sectional method whereas radiative heat transfers from soot particles are captured with the assumption of an optically thin medium according to Di Domenico et *al.* Di Domenico et al. (2010). Simulation results of Zhang et al. (2009) have been obtained using a detailed chemistry mechanism from Appel et al. (2000) including of 99 species and 531 reactions. Soot particles distribution has been modeled with a sectional method whereas a statistical narrow-band correlated-k based band model was employed to obtain the absorption coefficients of H_2O, CO_2 and CO (Liu et al. (2004)).

The radially-integrated soot volume fraction is fairly captured up to 20 mm, experimental data are underestimated up to one order of magnitude further downstream. It is not the case Zhang detailed chemistry solutions which match perfectly the experiments. We attribute the failure of virtual chemistry in this region to the flame archetypes retained in the learning database. This is confirmed by the non-adiabatic detailed calculation (D-Rs), which is capable to reproduce this tendency, even though the order of F_v is underpredicted.

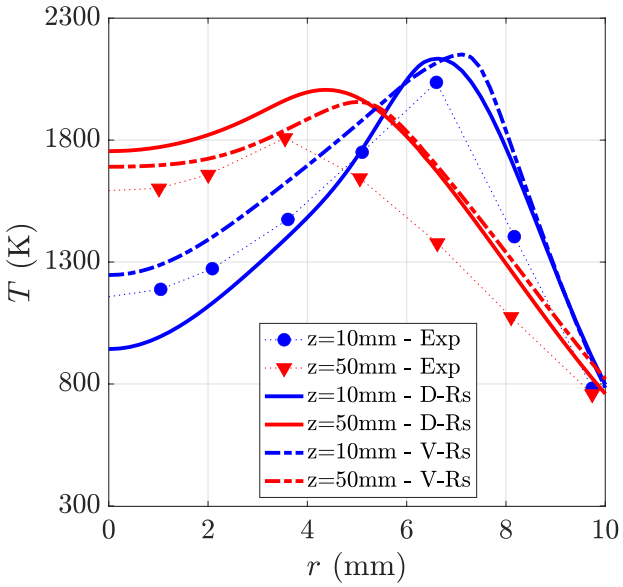

Figure 3.15: *Santoro Coflow Flame: Temperature radial profiles. Comparison of detailed and virtual chemistry results (lines) against experimental data (symbols).*

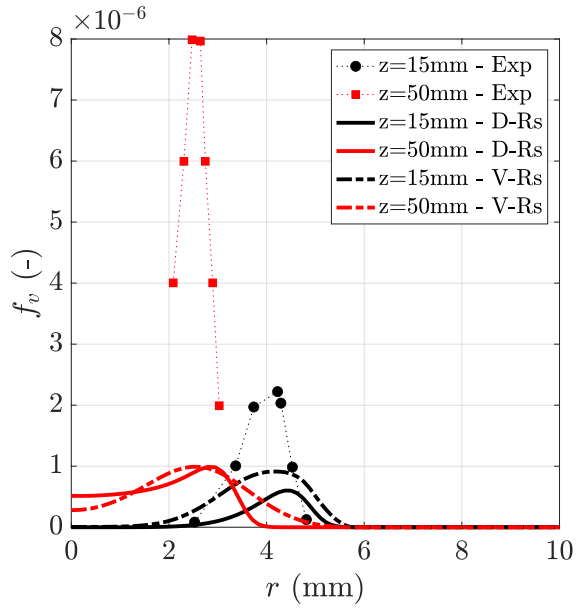

Figure 3.16: *Santoro Coflow Flame: Soot volume fraction radial profiles. Comparison of detailed and virtual chemistry results (lines) against experimental data (symbols).*

Indeed, close to the burner exit, the chemical flame structure follows a classi-

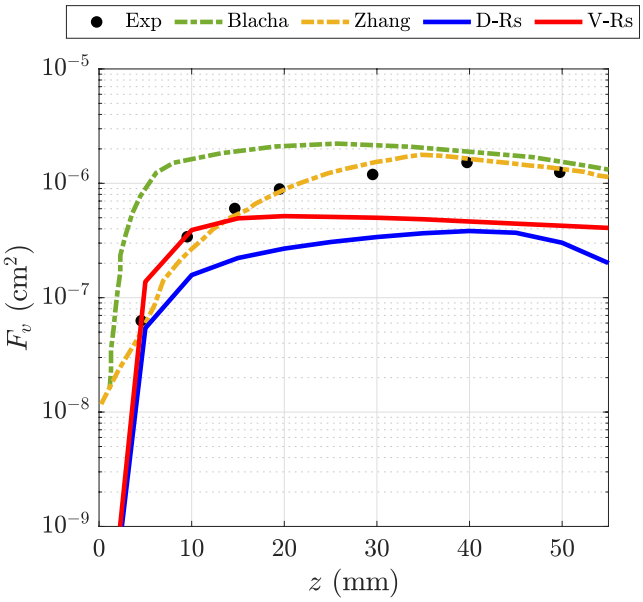

Figure 3.17: *Santoro Coflow Flame: Integrated soot volume fraction profiles along the centerline. Comparison of detailed and virtual chemistry results against experimental measurements. Numerical results from other groups are also included.*

cal non-premixed flamelet where pure fuel diffuses into pure air. Such flamelet element has been well targeted during the optimization process. However, further downstream, burner gases mix with surrounding air coflow prior entering the soot chemistry reactive layer. The flame archetype is therefore closer to a diluted air/burnt gases stream counterflowing the fuel stream, a configuration which is not considered during the virtual soot sub-mechanism optimization process.

3.8 Conclusions and discussion

A new reduced virtual chemistry model is developed to predict the temperature profiles and heat release rate and soot volume fraction in laminar ethylene-air flames. Also, a virtual approach is proposed in order to include gas phase radiative heat transfer in the simulations. The simplicity of the models makes possible to retrieve flame characteristics, such as temperature and heat release rate together with soot volume fraction. Indeed, this new virtual approach integrates for the first time both gaseous and solid phases in a virtual mechanism, by bypassing the gas-solid complex formalism without explicit mathematical distinction between both phases.
Numerical results using the new virtual model are validated in 1-D ethylene air flames in canonical configurations, such as premixed and non-premixed

flames, against reference detailed chemistry calculations. Additionally, the virtual model is challenged in a 1-D burner-stabilized flame configuration, giving very good results when compared to reference detailed chemistry calculations and experimental measurements. This shows that the virtual model is capable to predict soot in configurations other than those used to build the reference database.
Furthermore, simulations in two 2-D configurations are carried out using the virtual models: a premixed slot burner and a non-premixed coflow burner from the ISF workshop. In both configurations, very good results of the flame structure and soot characteristics are obtained. In overall, the new virtual soot sub-mechanism captures soot physical phenomena with good level of accuracy and is comparable to other numerical works in the literature with more detailed models. Also, the new virtual radiative model well provides well the heat losses.
In general, a massive reduction of the soot kinetics model is obtained, passing from 297 species and 16797 reactions in the reference detailed mechanism to 12 virtual species and 6 virtual reactions in the virtual mechanism. This chemical reduction has a big impact on the computational cost of the simulations. The CPU cost is reduced by a factor of about 2100 in 2-D laminar flames, considering the virtual and detailed models.
However, in order to predict more complex soot phenomena such as a diluted condition as it is found in some regions of the Santoro flame, the optimization process would need the addition of other flame archetypes to enrich the learning database. This may also demand further parametrization of the chemical parameters or the addition of new virtual reactions.
Also, additional features, such as in order to capture particle size distribution, can be added to the virtual soot sub-mechanism to better describe the soot formation. In this case, the particle number density and/or the total soot surface can be envisaged to be transported in the virtual combustion system. Supplementary hypotheses may be required, involving a new strategy in the optimization process. This could result in the reconstruction of the associated particle size distribution, given by the inversion of the three-moment system that has been established (Franzelli et al. (2019)).
Finally, conception of an automated process could ease the construction of the architecture of virtual mechanism. Analysis of the chemical species characteristic time scales could be useful to lead the process. This may permit the developer to better identify the important chemical pathways to the pollutant species under study and find a link to the minimum degree of freedom needed in the combustion equation system.

Chapter 4

Turbulent combustion modeling

Contents

In this chapter, the fundamentals of turbulent combustion are presented. Numerical methods employed for turbulent reactive flows are first introduced. The Large-Eddy Simulation strategy and its formalism are described, and then applied to the governing equations of the turbulent reactive flow. Unsolved terms are closed in the LES framework. The different turbulent combustion models for LES are described. Eventually, the Thickened Flame model for LES is reported, which constitutes the numerical method to solve the turbulent flame structure later.

4.1 Numerical methods in turbulent combustion

Three strategies exist in computational fluid dynamics (CFD) to solve the Navier-Stokes equations (N-S) in turbulent regimes: Direct Numerical Simulation (DNS), Reynold-Averaged Navier-Stokes (RANS) approach and Large-Eddy Simulations (LES). In DNS, the N-S equations are fully resolved. This is very computational demanding, since all turbulent structures in the Kolmogorov cascade must be temporally and spatially solved. Therefore, using DNS to solve practical turbulent configurations remains unfeasible and is reserved to fundamental problems. In the case of RANS, however, a time-averaging operation is made on the N-S equations and turbulent fluxes are modeled. Only time-averaged quantities are transported and, in consequence, some averaged and fluctuating terms of the RANS equations must be modeled for all the turbulent energetic spectrum in the Kolmogorov cascade. Finally, in LES the N-S equations are solved for the large energetic eddies while the small-scale energetic structures are modeled. The main advantage of LES compared to RANS, by resolving large energetic structures, it allows better reproduction of the turbulent mixing processes (Pope (2000)), and therefore better characterization of turbulent-flame interactions and prediction of chemical species (Poinsot and Veynante (2012)). Then, the filter size Δ linked to the LES grid element define a cut-off wave number $k_c = \pi/\Delta$, which determines the limit on the spectral space between large and small turbulent energy structures. Figure 4.1 (Mercier (2015)) shows the scope of the three techniques used in CFD simulations in the physical and spectral spaces, which depicts how each one handles the turbulent energy structures found in the turbulent flow. The CPU cost increases when considering three approaches in the following direction: RANS→LES→DNS.
Lately, LES is frequently used for the simulation of turbulent combustion in practical applications, such as industrial burners and aeronautical combustors. In this thesis, turbulent sooting flames are computed using the LES technique.

4.2 Governing equations in the LES framework

4.2.1 LES formalism

Filtered quantities $\overline{\varphi}$ are defined as:

$$\overline{\varphi}(\mathbf{x},t) = \int \varphi(\mathbf{x}',t) G_\Delta(\mathbf{x}-\mathbf{x}') d\mathbf{x}'. \tag{4.1}$$

where G_Δ is a LES filter of width Δ. The Favre-filtering operation ($\widetilde{\cdot}$) on φ is defined as:

$$\widetilde{\varphi}(\mathbf{x},t) = \frac{\overline{\rho\varphi}}{\overline{\rho}} \tag{4.2}$$

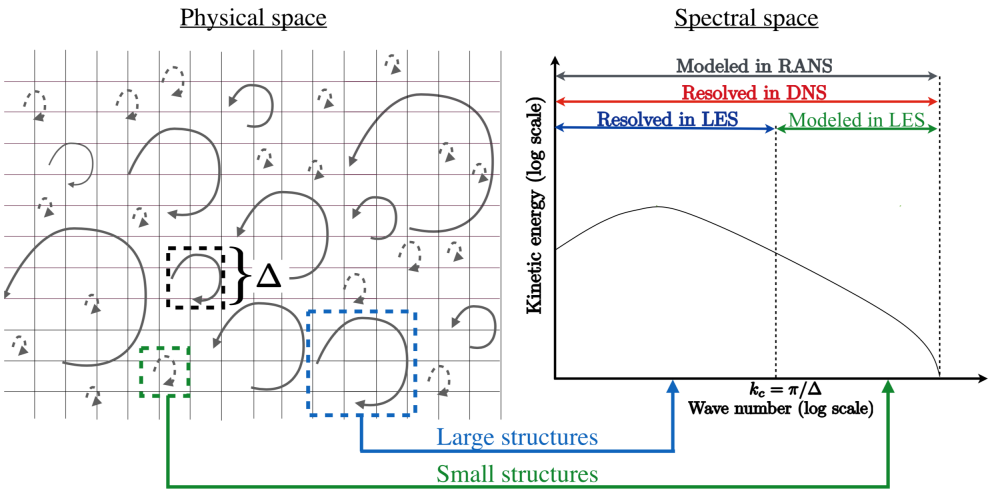

Figure 4.1: *CFD resolution techniques in turbulent flows considering homogeneous and isotropic turbulence (From Mercier (2015)). The filter size Δ of the numerical grid determines wether the turbulent energy structures are resolved or not (left). Resolution and modeling considerations for DNS, RANS and LES approaches regarding the turbulent energy structures in the energy cascade (right). $k_c = \pi/\Delta$ denotes the cut-off wave number used in LES filtering.*

In this regard, a total quantity φ is composed of the resolved component $\widetilde{\varphi}$ and the fluctuation component φ'', which is usually referred to as subgrid- or subfilter-scale part. Then, $\varphi = \widetilde{\varphi} + \varphi''$. The decoupling of resolved and fluctuating components is implicitly made by the LES grid, where turbulent structures larger than twice the size of the filter Δ_x are typically resolved.

4.2.2 Filtered balance equations

The turbulent reactive flow is governed by the N-S equations. In LES using virtual chemistry, a filtering operation is performed to Eqs. 2.19 to 2.22 in the main mechanism and Eq. 2.24 in the pollutant sub-mechanism, which reads:

Main mechanism:

$$\frac{\partial \overline{\rho}}{\partial t} + \frac{\partial}{\partial x_i}\left(\overline{\rho}\widetilde{u}_i\right) = 0 \tag{4.3}$$

$$\frac{\partial \overline{\rho}\widetilde{u}_j}{\partial t} + \frac{\partial}{\partial x_i}\left(\overline{\rho}\widetilde{u}_i\widetilde{u}_j\right) = -\frac{\partial \overline{P}}{\partial x_j} + \frac{\partial}{\partial x_i}\left(\overline{\tau}_{ij} - \overline{\rho}\left(\widetilde{u_i u_j} - \widetilde{u}_i\widetilde{u}_j\right)\right) \tag{4.4}$$

$$\frac{\partial \overline{\rho}\widetilde{e}_t}{\partial t} + \frac{\partial}{\partial x_i}\left(\overline{\rho}\widetilde{u}_i\widetilde{e}_t\right) = \frac{\partial}{\partial x_i}\left(\lambda\frac{\partial T}{\partial x_i} - \rho\sum_{k=1}^{N_s^M} Y_k^M V_k^M h_k\right) + \frac{\partial}{\partial x_i}\left(\overline{\sigma_{ij}u_j} - \overline{\rho}\left(\widetilde{u_i e_t} - \widetilde{u}_i\widetilde{e}_t\right)\right) + \overline{\dot{Q}}_r \tag{4.5}$$

$$\frac{\partial \overline{\rho}\widetilde{Y}_k^M}{\partial t} + \frac{\partial}{\partial x_i}\left(\overline{\rho}\widetilde{u}_i\widetilde{Y}_k^M\right) = \frac{\partial}{\partial x_i}\left(\overline{\rho V_{k,i}^M Y_k^M} - \overline{\rho}\left(\widetilde{u_i Y_k^M} - \widetilde{u}_i\widetilde{Y}_k^M\right)\right) + \overline{\dot{\omega}}_k^M \tag{4.6}$$

Pollutant sub-mechanism:

$$\frac{\partial \overline{\rho}\widetilde{Y}_k^{s_p}}{\partial t} + \frac{\partial}{\partial x_i}\left(\overline{\rho}\widetilde{u}_i\widetilde{Y}_k^{s_p}\right) = \frac{\partial}{\partial x_i}\left(\overline{\rho V_{k,i}^{s_p} Y_k^{s_p}} - \overline{\rho}\left(\widetilde{u_i Y_k^{s_p}} - \widetilde{u}_i\widetilde{Y}_k^{s_p}\right)\right) + \overline{\dot{\omega}}_k^{s_p} \tag{4.7}$$

Unclosed terms of the filtered equations are expressed as follows (Poinsot and Veynante (2012)):
Reynolds stress tensor: Using a Boussinesq assumption for a completely diffusive behavior, $\overline{\tau}_{ij}^{sgs}$ is modeled as:

$$\overline{\tau}_{ij}^{sgs} = -\overline{\rho}\left(\widetilde{u_i u_j} - \widetilde{u}_i\widetilde{u}_j\right) = \overline{\rho}\nu_t\left[\left(\frac{\partial \widetilde{u}_i}{\partial x_j} + \frac{\partial \widetilde{u}_j}{\partial x_i}\right) - \frac{2}{3}\delta_{ij}\frac{\partial \widetilde{u}_k}{\partial x_k}\right] \tag{4.8}$$

where ν_t stands for the turbulent kinematic viscosity. Several closures models exist for ν_t in the literature (Germano et al. (1991); Nicoud and Ducros (1999); Nicoud et al. (2011)).

Energy and species fluxes: $\overline{q}_i^{sgs}$ and $\overline{J}_{i,k}^{sgs}$ normally have gradient-type closures, respectively as:

$$\overline{q}_i^{sgs} = \overline{\rho}\left(\widetilde{u_i e_t} - \widetilde{u}_i\widetilde{e}_t\right) = -\frac{\mu_t \overline{c_p}\left(\overline{T}, \overline{Y}_k\right)}{\mathrm{Pr}_t}\frac{\partial \widetilde{T}}{\partial x_i} + \sum_{k=1}^{N_s}\overline{J}_{i,k}^{sgs}\widetilde{h}_k \tag{4.9}$$

$$\overline{J}_{i,k}^{sgs} = \overline{\rho}\left(\widetilde{u_i Y_k} - \widetilde{u}_i\widetilde{Y}_k\right) = \overline{\rho}\left(\frac{\nu_t}{\mathrm{Sc}_{t,k}}\frac{W_k}{W}\frac{\partial \widetilde{X}_k}{\partial x_i} - \widetilde{Y}_k\widetilde{V}_i^{c,sgs}\right) \tag{4.10}$$

where the turbulent Schmidt number $\mathrm{Sc}_{t,k}^v$ (of species k) and the turbulent Prandtl number Pr_t are usually set to a constant value or evaluated dynamically (Moin et al. (1991)).

Filtered laminar diffusion fluxes of momentum, energy and species: a gradient-kind closure is used, as follows:

$$\overline{\tau}_{ij} = \overline{\rho\nu}\left[\left(\frac{\partial \widetilde{u}_i}{\partial x_j} + \frac{\partial \widetilde{u}_j}{\partial x_i}\right) - \frac{2}{3}\delta_{ij}\frac{\partial \widetilde{u}_k}{\partial x_k}\right] \tag{4.11}$$

$$\overline{q}_i = -\overline{\lambda\frac{\partial T}{\partial x_i} + \rho\sum_{k=1}^{N_s} Y_k V_k h_k} = -\overline{\lambda}\frac{\partial \widetilde{T}}{\partial x_i} + \sum_{k=1}^{N_s}\overline{J_{i,k}}\widetilde{h}_{sk} \tag{4.12}$$

$$\overline{J}_{i,k} = \overline{\rho V_{k,i} Y_k} = \overline{\rho}\left(-\overline{D}_k\frac{W_k}{W}\frac{\partial \widetilde{X}_k}{\partial x_i} + \widetilde{Y}_k\widetilde{V}_i^c\right) \tag{4.13}$$

Filtered radiative heat transfer: $\overline{\dot{Q}}_r$ is significant in turbulent jet flames, at high temperatures (Ihme and Pitsch (2008)) and with significant presence of soot particles (Zhang et al. (2011)). In this work, the optically thin approximation is kept for the radiative source term. The filtered radiative source term is approximated by neglecting subgrid-scale temperature and mixture fraction fluctuations: $\overline{\dot{Q}}_r \simeq \dot{Q}_r(\widetilde{T}, \widetilde{Z})$, Poitou et al. (2008).

Filtered chemical source term: the term $\overline{\dot{\omega}}_k$ is challenging to close in turbulent combustion systems, especially because of the high interaction with the turbulent structures and its peculiar behavior at the flame front, which is highly dependent on the turbulent combustion regime (Poinsot and Veynante (2012)). Numerous models exist in the literature to retrieve the subgrid-scale effects in the turbulent reactive flow. A summary of the main techniques are presented in Section 4.3.

4.3 Turbulent combustion modeling in LES

The reproduction of the turbulent flame structure is severely affected by the numerical grid size in LES, especially in large industrial configurations where one cannot afford a fine resolution of the flame front because of the CPU limits. In consequence, to properly resolve the flame front, turbulence-chemistry interactions must be modeled at the subgrid scale. Similar issues are encountered in the prediction of pollutant species. However, the different chemical source terms closures are function of the turbulent combustion model considered within the LES framework. Several methods are proposed in the literature (Fiorina et al. (2015); Poinsot and Veynante (2012)), where three main numerical approaches are summarized below:

- The *turbulent mixing method* supposes that the chemical time scale is shorter than the integral time scale of the turbulent reactive flow $\tau_c < \tau_t$. Here, the turbulent mixing processes limits the chemical reaction rates. Some examples of this method are the Eddy Dissipation Model (Magnussen and Hjertager (1977)) and the Linear-Eddy Model (Menon and Calhoon Jr (1996)), but these were mainly used in RANS calculations rather than LES.

- The *statistical methods* describe the turbulent reactive flow properties in LES through a Probability Density Function (PDF) (Pope (1985)) or a Filtered Density Function (FDF) (Haworth (2010)). These approaches have been extensively used in LES of turbulent flames. However, it can be computational demanding and may require complex modeling hypothesis when Lagrangian and Eulerian strategies are involved.
- The *geometrical methods* characterize and track the turbulent flame front by making assumptions on the vicinity of the propagating iso-surface dividing the fresh and burnt gases zones. A first approach, called the G-equation model (Kerstein et al. (1988)), considers the flame thickness negligible and traces the flame surface with the help of a field variable $\widetilde{G}$. In other approaches, the flame thickness is resolved across the reactive layer of the flame. The main examples of these strategies are the Thickened Flame model for LES (TFLES, Colin et al. (2000)) and the Filtered-Tabulated Chemistry for LES (F-TACLES, Fiorina et al. (2010)). In F-TACLES the flame front is explicitly filtered in the physical space, while in TFLES the flame front is artificially thickened.

The virtual chemistry approach has presented very good capabilities to reproduce the turbulent flame structure and pollutant prediction using the TFLES (Cailler et al. (2017); Maio et al. (2019); Maio et al. (2020)). Therefore, this methodology is retained in this thesis. The TFLES approach is introduced in the following subsection.

4.4 Artificial thickened flame model for LES (TFLES)

The TFLES model provides a good description of the chemical source terms. It is characterized by its easy implementation and robustness in combustion modeling. In this method, originally developed for the RANS approach (Butler and O'Rourke (1977)), the thickening operation is done preserving the flame consumption speed, while the diffusion and species source terms are modified. This broadening process is ensured by the thickening factor F_T. The diffusion coefficient and the species source terms are then multiplied and divided by F_T. In the laminar premixed flames theory, the following expressions are well founded:

$$S_L^0 = \sqrt{D\overline{\dot{\omega}}} \tag{4.14}$$

$$\delta_L^0 = \frac{D}{S_L^0} \tag{4.15}$$

where S_L^0 and δ_L^0 are the laminar flame consumption speed and thermal thickness, respectively, D the thermal diffusivity and $\overline{\dot{\omega}}$ the mean reaction rate. By multiplying D and dividing $\overline{\dot{\omega}}$ by $F_T > 1$, S_L^0 maintain its value while δ_L^0 widens. However, this procedure makes the flame smoother and the turbulent

flame speed decreases, *i.e.* it affects the turbulence-chemistry interactions. It was shown by Angelberger et al. (1998) that turbulent eddies smaller than $F\delta_L^0$ does not affect the thickened flame and a subgrid-scale model is needed.
When the ratio between the turbulent length scale and the laminar flame thickness is decreased, the flame becomes more and more insensitive to turbulence motions (Poinsot and Veynante (2012)). This ratio is decreased when the flame is thickened. An efficiency function Ξ_Δ (subgrid-scale wrinkling factor) has then been introduced by Colin et al. (2000) to account for turbulence-flame interactions in the thickened region. Models such as algebraic expressions (Boger et al. (1998); Boger and Veynante (2000)), similarity models (Knikker et al. (2002); Knikker et al. (2004)) or balance equations (Weller et al. (1998); Boger and Veynante (2000); Hawkes and Cant (2000)) may be used to express Ξ_Δ. Generally, equilibrium condition hypotheses of turbulence and flame wrinkling are made (Charlette et al. (2002a); Colin et al. (2000); Pitsch and De Lageneste (2002)). However, there are some limitations when flame development is in its early stages (Veynante and Moureau (2015)). Therefore, a dynamic formulation of Ξ_Δ was proposed as an alternative (Charlette et al. (2002b); Wang et al. (2011); Veynante and Moureau (2015)), which is evaluated on an ongoing basis with the calculations.
A strategy to avoid an increase of the diffusive fluxes in mixing controlled regions was proposed by Legier et al. (2000). It consist to dynamically applying the thickening operation across the flame reactive layer. A flame sensor S_F is then used to track the flame position. S_F equals one (respectively zero) inside the flame region (respectively outside).
The filtered balance equation for the species k using the TFLES closure from Colin et al. (2000), reads:

$$\frac{\partial \overline{\rho}\widetilde{Y}_k}{\partial t} + \frac{\partial}{\partial x_i}\left(\overline{\rho}\widetilde{u}_i\widetilde{Y}_k\right) = \frac{\partial}{\partial x_i}\left(\overline{\rho}F_T\Xi_\Delta\overline{D}_k\frac{\partial \widetilde{Y}_k}{\partial x_i}\right) + \frac{\Xi_\Delta}{F_T}\overline{\dot{\omega}}_k. \tag{4.16}$$

The dynamic TFLES approach using virtual chemistry is presented in Chapter 5.

4.5 Conclusion

In this chapter, the basics of turbulent combustion was presented. The LES formulation was introduced, a noteworthy strategy to tackle the simulations of turbulent flames in practical configurations. The filtered governing equations in LES were established, as well as the different closures for the unresolved terms in the LES framework. The different techniques used to close the filtered chemical source terms in turbulent combustion were described. The Thickening Flame model for LES was introduced. This model will be used in the virtual chemistry framework.

Chapter 5

Soot virtual chemistry in turbulent flames

Contents

In this Chapter, the new virtual soot sub-mechanism and radiative models are challenged in a turbulent flame configuration. First, the laminar flame context is introduced. The virtual species governing equations in turbulent combustion are detailed, using the TFLES closures. Time and length scales analyses are performed, which lay the foundation for the development of a new subgrid-scale model to capture the turbulence-soot interactions in the virtual chemistry framework. The turbulent flame experimental and numerical setups are defined for the application case. The virtual models for chemistry, radiation and subgrid-scale turbulence-soot interactions are challenged to a turbulent sooting flame and results are eventually compared to numerical and experimental data. The content of this chapter refers to an article under preparation for submission to "Combustion and Flame".

5.1 Introduction

Soot modeling in turbulent flames is a great challenge because of the complexity of multi-physical phenomena involved. The numerical modeling strategy used in Large-Eddy Simulations (LES) is usually divided in three sections: modeling of the gas-phase, the solid-phase, and the soot-turbulence-chemistry interactions. The gas-phase kinetics must reproduce not only the flame structure but also small hydrocarbon radicals, such as acetylene, and soot precursors, such as polycyclic aromatic hydrocarbons (PAHs) (Frenklach and Wang (1994)). The prediction of these species needs the knowledge of the complex chemical pathways involved in detailed mechanisms involving hundreds of species and thousands of reactions. It involves prohibitive CPU times in LES of practical applications. Consequently, kinetic reduction techniques such as tabulated kinetics methods (Gicquel et al. (2000); Ihme and Pitsch (2008)), analytically reduced chemistry approaches (Pepiot (2008)) and global optimized chemistry (Franzelli et al. (2010)) are generally employed in LES of turbulent sooting flames.
A solid-phase model is dedicated to reproduce the dynamics and surface reactivity of soot particles. In LES, reduced soot models are preponderant in the literature, such as discrete sectional methods (Grader et al. (2018); Rodrigues et al. (2018)), Method of moments (MOMs) (Mueller and Pitsch (2012b)) or even semi-empirical methods (Franzelli et al. (2015); Franzelli et al. (2019)). Several authors have shown that both the gas-phase kinetic chemistry and the soot models, as well as the soot nucleation strategy, have a considerable impact on soot formation (Xuan and Blanquart (2015); Selvaraj et al. (2016); Han et al. (2019); Chong et al. (2019); Jain and Xuan (2019)).
Modeling the soot-turbulence interactions is a crucial point in LES of turbulent flames. The formulation of the subgrid-scale closure of the filtered soot source terms was addressed in multiple occasions (El-Asrag et al. (2007); Mueller and Pitsch (2011); Yang et al. (2019)). In overall, it has been observed that a high

soot particles intermittency is found at the subfilter level and the disparate characteristic time scales of soot phenomena can affect the formation process, which could be difficult to handle.
A high degree of detail of the selected numerical models results in a high computational demand. To overcome with this issue, a reduced soot kinetic mechanism was proposed in Chapter 3 based on the virtual chemistry approach (Cailler et al. (2017)). The originality of this approach is that soot prediction is modeled to reproduce the soot volume fraction in a straightforward way and is optimized for several operating conditions, *i.e.* it has the advantage of reducing the overall process by targeting only the final quantities of interest. Hence, thanks to of its global nature, the virtual chemistry would circumvent intermediate pathways between the gas and solid phases, but it would remain accurate due to the optimization of thermochemical properties to reproduce target quantities, such as laminar flame speed, temperature and soot volume fraction. This model has proven to be able of predicting soot formation in several 1-D and 2-D laminar combustion configurations.
Moreover, virtual chemistry has presented very good capabilities to reproduce the turbulent flame structure and pollutant emission using the Thickened Flame model for LES (TFLES) (Colin et al. (2000); Cailler et al. (2017); Maio et al. (2019); Maio et al. (2020)). However, in LES of turbulent sooting flames, issues have arisen when developing a turbulent combustion model able to capture both the flame front (main reactive layer) and the interactions between turbulence and soot chemistry, which occurs at a much slower time scale. Therefore, a new subgrid-scale model is proposed here to manage the filtered soot source terms in a virtual chemistry framework.
This chapter is organized as follows. The virtual chemistry and radiative models for soot formation in laminar flames are presented in Section 5.2. Then, section 5.3 introduces the numerical model used for the LES of the turbulent reactive flow. Next, the subgrid-scale model used for the virtual soot chemistry, based on the analysis of the characteristic time and length of soot formation in laminar flames is presented in Section 5.4. The virtual chemistry, radiative and subgrid-scale models are applied to a 3-D a sooting turbulent non-premixed ethylene-air flame: the Sandia burner. The experimental and numerical setups are presented in Section 5.5. Results and validations are presented in Section 5.6. Finally, the conclusions and discussion are presented in Section 5.7.

5.2 Laminar sooting flames using virtual chemistry

In chapter 3 it was proposed a new reduced kinetic model for soot formation in hydrocarbon-air flames, based on the virtual chemistry approach (Cailler et al. (2017); Cailler et al. (2020)). This virtual mechanism is divided in two blocks: the virtual main mechanism and the virtual soot sub-mechanism. The thermodynamics, kinetic rate and radiative model parameters of both blocks

are optimized to reproduce the flame characteristics (main mechanism) and soot formation prediction (soot sub-mechanism), such as: mixture properties of the gas phase, laminar flame speed, temperature, radiative heat losses and soot volume fraction. The chemical structures of the virtual main and sub-mechanisms, as well as the virtual radiative model, are presented in the following sub-sections.

5.2.1 Virtual main mechanism

The main virtual mechanism is capable to reproduce the flame structure of a hydrocarbon-air combustion system and it consist of a 2-step, 8-species kinetic scheme as follows:

$$\alpha^M_{F,1}F + \alpha^M_{Ox,1}Ox + \alpha^M_{D,1}D \rightarrow \alpha^M_{I,1}I + \alpha^M_{D,1}D \qquad (R^M_1)$$

$$I \rightarrow \sum_{k=1}^{N^M_P=4} \alpha^M_{P_{k,2}}P_k \qquad (R^M_2)$$

where F, Ox and D correspond to the fuel, oxidizer and dilutant species. $N^M_P = 4$ combustion products P_k are considered. $\alpha^M_{k,r}$ is the stoichiometric coefficient per unit mass of the k^{th} virtual species in the r^{th} virtual reaction. The thermodynamics of the virtual products and the reaction rate parameters of the two reactions constitute a set of thermochemical parameters χ^M. Hence, χ^M is calibrated using a machine learning algorithm from (Cailler et al. (2017)), by targeting results using a reference detailed chemistry, which is composed of mixture equilibrium properties and flame characteristics, such as laminar consumption speed S_L, the temperature profile, etc. A unitary Lewis number assumption was made for the transport properties.

5.2.2 Virtual soot sub-mechanism

The virtual soot sub-mechanism is composed by a 4-reactions, 6-species kinetics scheme that reproduce global soot phenomena and has the following chemical structure:

$$\alpha^s_{F,1}F + \alpha^s_{Ox,1}Ox \rightarrow \alpha^s_{V_1,1}V_1 + \alpha^s_{V_3,1}V_3 \qquad (R^s_1)$$

$$V_1 \rightarrow \alpha^s_{\mathcal{S},2}\mathcal{S} + \alpha^s_{V_2,2}V_2 \qquad (R^s_2)$$

$$\mathcal{S} + V_1 + V_2 \rightarrow \alpha^s_{\mathcal{S},3}\mathcal{S} + \alpha^s_{V_3,3}V_3 \qquad (R^s_3)$$

$$\mathcal{S} + Ox + V_2 \rightarrow Ox + 2V_3 \qquad (R_4^s)$$

where $\mathcal{S}$ is the soot virtual species, and V_1, V_2 and V_3 are additional virtual products. $\alpha_{k,r}^s$ is the stoichiometric coefficient per unit mass of the k^{th} virtual species in the r^{th} virtual reaction. These virtual species in conjunction with the virtual reactions R_1^s–R_4^s make possible to predict the soot volume fraction. The chemical coupling between the main and sub-mechanisms is guaranteed by the virtual reactions R_1^M and R_1^s, by which is assumed these reactions provide the same reaction rate (*cf.* Chapter 3). Similar to the main mechanism, the reaction rate parameters of the soot kinetics form a chemical parameters set χ^s, which is optimized using the very same machine learning algorithm previously mentioned. Since the gas and solid phases are mathematically implicit without discrimination in the virtual soot system, the complexity of soot phenomena is avoided. Here, soot volume fraction is computed as $f_v^s = \rho Y_{\mathcal{S}}^s / \rho_s$ where $Y_{\mathcal{S}}^s$ is the soot mass fraction and ρ_s is the soot density, which is considered constant and equals to 1800 kg m^{-3}. Regarding the transport properties, soot Lewis number was set to 25, while the other virtual species kept the unitary Lewis number supposition.

5.2.3 Chemical source terms

The rate of progress $q_r^{\mathcal{V}_m}$ of the r^{th} virtual reaction belonging to a virtual mechanism $\mathcal{V}_m = (M, s)$, out of $N_r^{\mathcal{V}_m}$ reactions, is obtained by an Arrhenius-like closure:

$$q_r^{\mathcal{V}_m} = A_r^{\mathcal{V}_m}(Z) \cdot T^{\beta_r^{\mathcal{V}_m}} \cdot \exp\left(\frac{E_{a,r}^{\mathcal{V}_m}}{RT}\right) \cdot \prod_{k=1}^{N_s^{\mathcal{V}_m}} [\psi_k^{\mathcal{V}_m}]^{n_{k,r}^{\mathcal{V}_m}(Z)}, \qquad (5.1)$$

where $A_r^{\mathcal{V}_m}$, $\beta_r^{\mathcal{V}_m}$, $E_{a,r}^{\mathcal{V}_m}$ and $n_{k,r}^{\mathcal{V}_m}$ are elements of $\chi^{\mathcal{V}_m}$ and correspond to the pre-exponential factor, the constant of the pre-exponential factor temperature dependence, the activation energy and the reaction rate order of the virtual species $\psi_k^{\mathcal{V}_m}$ in the r^{th} reaction, respectively. $[\psi_k^{\mathcal{V}_m}]$ denotes the molar concentration of the virtual species $\psi_k^{\mathcal{V}_m}$. $N_s^{\mathcal{V}_m}$ is the number of virtual species $\psi_k^{\mathcal{V}_m}$ in $\mathcal{V}_m$. The dependence on the mixture fraction Z of certain chemical parameters were discussed in Chapter 3. The chemical source term of the k^{th} virtual species in $\mathcal{V}_m$ is therefore given by:

$$\dot{\omega}_k^{\mathcal{V}_m} = \sum_{r=1}^{N_r^{\mathcal{V}_m}} \nu_{k,r}^{\mathcal{V}_m} q_r^{\mathcal{V}_m} \qquad (5.2)$$

where $\nu_{k,r}^{\mathcal{V}_m}$ is the global stoichiometric coefficients per unit mass of the k^{th} virtual species in the r^{th} virtual reaction.

5.2.4 Radiative source term

Sooting flames may present significant radiative heat losses. The radiative model proposed in Chapter 3 is retained. An optically-thin approximation is considered to reproduce the radiative effects of temperature and soot in hydrocarbon-air sooting flames. The radiative source term reads:

$$\dot{Q}_r(T,Z) = 4\kappa^v_{\text{Planck}}(T,Z)\sigma\left(T^4 - T_b^4\right), \tag{5.3}$$

where T_b is the background cold temperature, σ is the Stephan-Boltzmann constant and κ^v_{Planck} is the virtual Planck absorption coefficient. κ^v_{Planck} is composed of the gas and solid phases contributions as $\kappa^v_{\text{Planck}} = \kappa^M_{\text{gas}} + \kappa^v_{\text{soot}}$. The gas absorption coefficient $\kappa^M_{\text{gas}}(Z,T)$ has a polynomial shape, where the set of polynomial coefficients Γ^M is optimized using the same strategy as before in the virtual kinetics. The soot absorption coefficient κ^v_{soot} is proportional to the soot volume fraction f^s_v given by the soot sub-mechanism and the temperature T given by the main mechanism, with the modeling constant $\alpha = 1302\ \text{m}^{-1}\text{K}^{-1}$ from Modest (2013).

5.3 Modeling the turbulent reactive flow

5.3.1 Virtual species equations with TFLES

The turbulent virtual species transport equations are coupled with the LES flow governing equations using a dynamic formulation of the Thickened Flame model for LES (TFLES) (Colin et al. (2000); Legier et al. (2000)). The Favre-filtered balance equations of mass fraction of the k^{th} virtual species Y_k belonging to the main and the soot mechanisms reads, respectively:
Virtual Main mechanism

$$\begin{aligned}&\frac{\partial \bar{\rho}\widetilde{Y}^M_k}{\partial t} + \frac{\partial}{\partial x_i}\left(\overline{\rho u}_i \widetilde{Y}^M_k\right) = \\ &\frac{\partial}{\partial x_i}\left[\left(F_T \Xi_\Delta \frac{\mu}{\text{Sc}^M_k} + (1-S_F)\frac{\mu_t}{\text{Sc}^M_{t,k}}\right)\frac{\partial \widetilde{Y}^M_k}{\partial x_i}\right] + \overline{\dot{\omega}}^M_k,\end{aligned} \tag{5.4}$$

Virtual soot sub-mechanism

$$\begin{aligned}&\frac{\partial \bar{\rho}\widetilde{Y}^s_k}{\partial t} + \frac{\partial}{\partial x_i}\left(\overline{\rho u}_i \widetilde{Y}^s_k\right) = \\ &\frac{\partial}{\partial x_i}\left[\left(F_T \Xi_\Delta \frac{\mu}{\text{Sc}^s_k} + (1-S_F)\frac{\mu_t}{\text{Sc}^s_{t,k}}\right)\frac{\partial \widetilde{Y}^s_k}{\partial x_i}\right] + \overline{\dot{\omega}}^s_k,\end{aligned} \tag{5.5}$$

where the superscripts M and s stand for the main and sub-mechanisms quantities, respectively. ρ is the mixture density and u_i is the i^{th} component of the

velocity. μ and μ_t are the laminar and turbulent viscosity, respectively. Sc and Sc_t are the laminar and turbulent Schmidt number. S_F is a global flame sensor defined as in Cailler et al. (2017):

$$S_F = (\max(S_{F,k}, 0), \text{for } k = 1, ..., N_{sp}) \tag{5.6}$$

where

$$S_{F,k} = \left(\min \left(\left| \frac{\overline{\dot{\omega}}_k^{\mathcal{V}_m}}{p \max(\dot{\omega}_k^{\mathcal{V}_m}(Z))} \right|, 1 \right), \text{for } \mathcal{V}_m = M \text{ and } s \right) \tag{5.7}$$

$\max(\dot{\omega}_k^{\mathcal{V}_m}(Z))$ is tabulated as function of the mixture fraction Z, from a collection of 1-D premixed laminar flames, varying the fresh gases equivalence ratio in the whole flammability limit. p is a threshold percentage value chosen to identify the flame reaction zone. The global thickening factor is given by the following definition:

$$F_T = (\max(F_{T,k}, 1), \text{for } k = 1, ..., N_{sp}) \tag{5.8}$$

where

$$F_{T,k} = \max \left[(F_{T,k}^{\max}) \cdot S_{F,k} + (1 - S_{F,k})), 1 \right]. \tag{5.9}$$

The maximum value of the species thickening factor $F_{T,k}^{\max}$ is computed so that the thickened reactive layer of species k is resolved by n grid points :

$$F_{T,k}^{\max} = \frac{n\Delta_x}{\delta_{r,k}^{\mathcal{V}_m}}, \tag{5.10}$$

where $\delta_{r,k}^{\mathcal{V}_m}$ is the reactive thickness of the k^{th} species and Δ_x is the grid size. This thickening flame model is validated in a 1-D laminar premixed ethylene-air flame in Appendix B.1 using the virtual mechanism presented in Section 5.2. The closure of the filtered chemical reaction term $\overline{\dot{\omega}}_k^s$ depends on the subgrid-scale (SGS) combustion regime. Time and length scale analyses of soot chemical processes are proposed in the next section in order to identify a consistent model strategy.

5.4 Subgrid-scale modeling of virtual soot chemistry

5.4.1 Soot chemical time and length scales analysis

This section aims to identify the time and length scales involved in the soot formation in order to select a consistent turbulent combustion modeling strategy. For that purpose, a series of 1-D freely-propagating premixed ethylene-air flames are computed at atmospheric pressure by using the virtual chemistry model presented in Section 5.2. The virtual scheme has been optimized in

Chapter 3 using several reference 1-D laminar flames computed with the detailed chemical scheme from Saggese et al. (2015). Temperature, virtual species mass fractions and normalized chemical source terms profiles calculated with the main and soot sub-mechanisms are plotted in Fig. 5.1 for two equivalence ratios $\phi = 2.1$ (left) and $\phi = 2.4$ (right). The coordinate $x = 0$ corresponds to the flame front position (mean temperature). Profiles presented in the two top figures correspond to those obtained by the main mechanism given by reactions R_1^M and R_2^M. For both equivalence ratios, chemical length scales are of the order of the thermal flame thickness, evaluated as:

$$\delta_L^0 = (T_{\max} - T_{\min}) / \max(dT/dx),$$

which is here about 1.3 mm for $\phi = 2.1$ and 1.5 mm for $\phi = 2.4$.
Virtual species mass fractions and reactions rates of the virtual soot sub-mechanism are shown in Fig. 5.1 (bottom) while a zoom at the flame front is presented in Fig. 5.1 (middle). The intermediate species V_1^s, directly linked to the consumption of F and O through reaction R_1^s is produced within the flame front. This is not the case of species involved in R_2^s to R_4^s, such as the $\mathcal{S}$ or intermediate species $V_1^{\mathcal{S}}$ and $V_2^{\mathcal{S}}$, which are mainly produced and consumed in a post-flame region. The thickness of the soot reactive layer δ_{soot}^0 is defined by the zone where $|\dot{\omega}_{\mathcal{S}}^s| > 0.001 \times \max(|\dot{\omega}_{\mathcal{S}}^s|)$. Here, δ_{soot}^0 appears to be much larger than the laminar flame thickness, about 100 mm for $\phi = 2.4$ and 500 mm for $\phi = 2.1$.
Chemical time scales τ_c^M and τ_c^s, representative of main and soot virtual chemistry, respectively, are defined as:

$$\tau_c^M = \frac{\delta_L^0}{S_{fg}^0}, \qquad \tau_c^s = \frac{\delta_{\text{soot}}^0}{S_{bg}^0}, \tag{5.11}$$

where S_{fg}^0 and S_{bg}^0 are the flame displacement speed in the fresh and burnt gases, respectively.
Chemical time scales associated with the flame front and the soot formation are plotted as a function of the equivalence ratio in Fig. 5.2. The soot chemistry is in average three orders of magnitude slower than the flame chemical time scale involved in the main reactive layer, where heat release occurs.

5.4.2 Subgrid-scale modeling of soot reaction rates

Turbulence interactions with flame and post-flame chemistry are evaluated by introducing the subgrid-scale Damkhöler numbers:

$$\mathrm{Da}^M = \frac{\tau_t}{\tau_c^M}, \qquad \mathrm{Da}^s = \frac{\tau_t}{\tau_c^s} \tag{5.12}$$

The turbulence time scale, τ_t, is expressed from the filter characteristic length Δ_x and the subgrid-scale velocity fluctuation u'_{sgs}:

$$\tau_t = \frac{\Delta_x}{u'_{sgs}}. \tag{5.13}$$

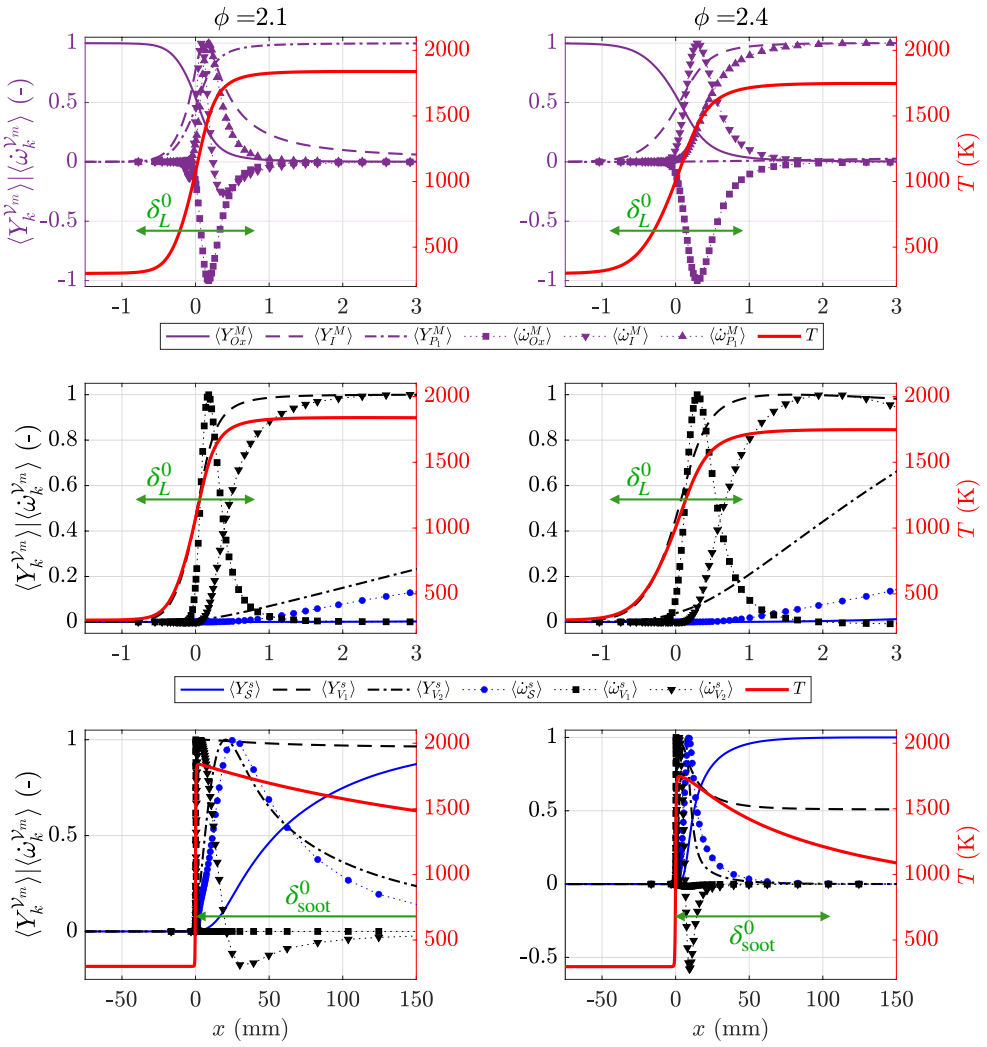

Figure 5.1: *Laminar flame profiles of main mechanism (top) and soot sub-mechanism (center and bottom) quantities at different equivalence ratios $\phi = 2.1$ (left) and $\phi = 2.4$ (right): Normalized mass fractions $\left\langle Y_k^{\mathcal{V}_m} \right\rangle$ (lines), normalized chemical source terms $\left\langle \dot{\omega}_k^{\mathcal{V}_m} \right\rangle$ (symbols with dotted lines), and temperature T (solid red lines). Normalization is defined as: $\langle \varphi \rangle = \varphi / \max(|\varphi|)$.*

As shown previously, chemical time scales involved in the main mechanism are of the order of 10^{-4} s, which is expected to be much smaller than the turbulence scales encountered in practical combustion chamber. Consequently $\text{Da}^M >> 1$, and the flamelet regime is retrieved. As in many geometrical modelling approaches (Fiorina et al. (2015)), the turbulent reaction rate for main mechanism species is modeled by introducing the subgrid-scale flame wrinkling

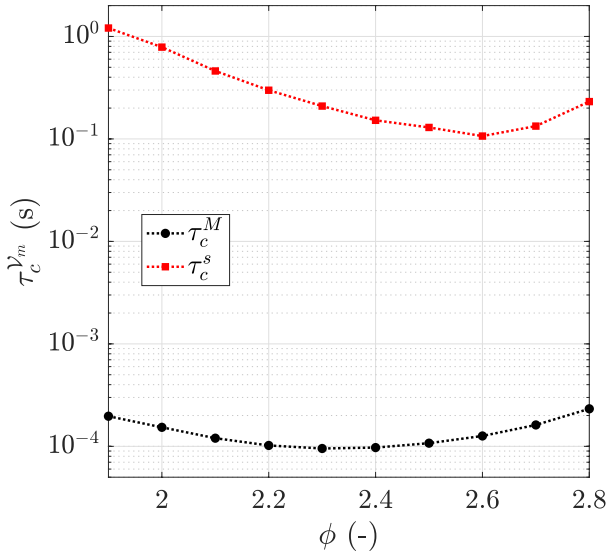

Figure 5.2: *Chemical time scales associated to the flame front τ_c^M and the soot formation τ_c^s in 1-D laminar premixed ethylene-air flames for different equivalence ratios ϕ.*

Ξ :

$$\overline{\dot{\omega}}_k^M = \frac{\Xi_\Delta}{F_T}\dot{\omega}_k^M(\widetilde{T},\widetilde{Z}) \tag{5.14}$$

As observed in Fig. 5.1, the virtual soot sub-mechanism involves both short and long time scales. The following hybrid formulation is therefore proposed to close the filtered chemical reaction rates $\overline{\dot{\omega}}_k^s$:

$$\overline{\dot{\omega}}_k^s = S_F \cdot \frac{\Xi_\Delta}{F_T}\dot{\omega}_k^s(\widetilde{T},\widetilde{Z}) + (1-S_F)\cdot \overline{\dot{\omega}}_k^s\Big|^{\text{PostFlame}} . \tag{5.15}$$

The first term on the RHS is equivalent to Eq. 5.14 and effective only across the flame front ($S_F = 1$), where the flamelet regime is encountered. The second term, activated in the post-flame region ($S_F = 0$), should consider the possibility of having chemical time scales slower than turbulent mixing phenomena.
Considering reactions R_1^s through R_4^s, and Eq. 5.2, the soot sub-grid source term post-flame closure (see Eq. 5.15) is then expressed as:

$$\overline{\dot{\omega}}_k^s\Big|^{\text{PostFlame}} = \sum_{r=1}^{N_r^s=4} \nu_{k,r}^s \overline{q_r^s}\Big|^{\text{PostFlame}} , \tag{5.16}$$

where $\overline{q_r^s}\Big|^{\text{PostFlame}}$ is the rate of progress post-flame closure of the r^{th} reaction of the soot virtual mechanism, defined as:

$$\overline{q_r^s}\Big|^{\text{PostFlame}} = \eta_r \cdot q_r^s(\widetilde{T},\widetilde{Z}). \tag{5.17}$$

η_r is a parameter which denotes the efficiency of the turbulence on the chemical reaction. To ensure consistency, rate of consumption of fuel and oxidizer present in reactions R_1^M and R_1^s must be the same in both main and soot virtual mechanisms. Consequently, η_1 is closed as follows:

$$\eta_1 = \frac{\Xi_\Delta}{F_T}. \tag{5.18}$$

It is expected that the soot characteristics time scales involved in reactions R_2^s to R_4^s are slower than subgrid turbulent time scale and $\mathrm{Da}^s << 1$. The combustion regime at the SGS corresponds therefore to a perfectly-stirred reactor (PSR) regime (Poinsot and Veynante (2012)). The efficiency factor η_r is then modeled by the Damkhöler number as:

$$\eta_r = \max\left(\frac{1}{\mathrm{Da}^s}, 1\right) \text{ for } r = 2, \text{ to } 4. \tag{5.19}$$

For large Da^s numbers, η_r is the clipped to 1 and is assumed that turbulence is not fast enough to affect the reaction. However for $\mathrm{Da}^s << 1$, the model considers that the subgrid-scale (SGS) turbulence enhances the chemical reactions by a factor $1/\mathrm{Da}^s$.

5.5 3-D turbulent sooting flame configuration: the Sandia burner

The virtual chemistry and radiative models for sooting flames presented in Section 5.2 are applied to conduct LES of the Sandia burner (Zhang et al. (2011)), which is a 3-D turbulent non-premixed ethylene-air jet flame studied by the International Sooting Flame (ISF) workshop (ISF5 (2021)).

5.5.1 Experimental setup

The burner, located into an air coflow, consists of a central jet of pure ethylene surrounded by a multitude of pilot flames. Burner geometry and dimensions are given in Fig. 5.3.
The main jet bulk velocity is $u_{fuel}^{\text{bulk}} = 54.7 \text{ cm} \cdot \text{s}^{-1}$. Pilot flames are fed with a premixed ethylene-air mixture of $\phi = 0.9$ at a mass flowrate of $1.772 \times 10^{-4} \text{ kg} \cdot \text{s}^{-1}$, corresponding to 2% of the heat release rate of the central jet. The air coflow mean velocity is $0.6 \text{ m} \cdot \text{s}^{-1}$. All gas flows are injected at atmospheric pressure and $T_0 = 294$ K. For further details on the experimental configuration, the reader may refer to Zhang et al. (2011).

5.5.2 Numerical setup

The computational domain, presented in Fig. 5.3, has a cylindrical shape with a diameter of $188D$ and a length of $500D$, where $D = 3.2$ mm is the inner

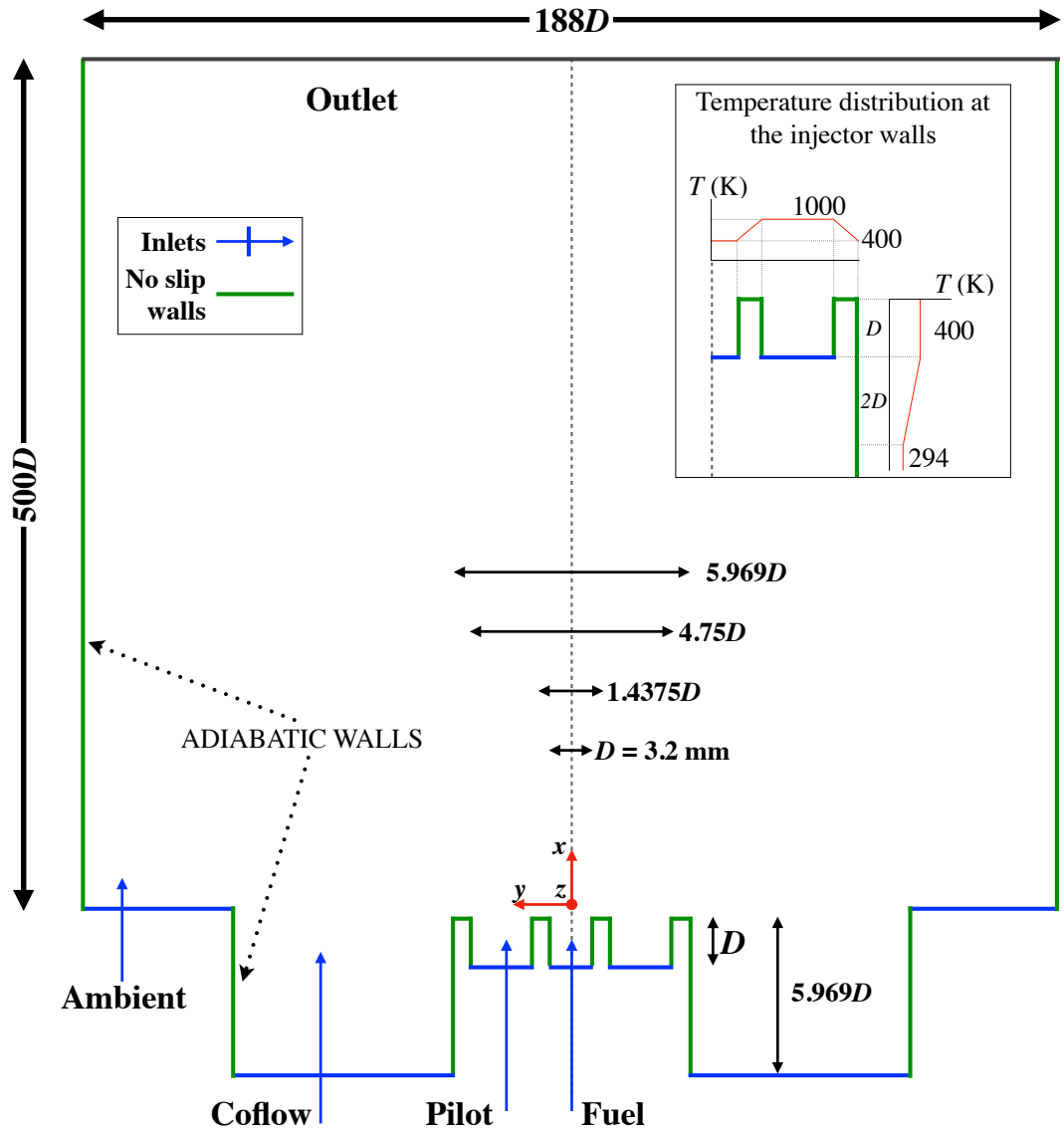

Figure 5.3: *Sandia burner: Schematics of the computational domain on the plane x-y. Geometry dimensions and different boundary conditions.*

diameter of the central tube. The unstructured grid, is made of 43.4 millions of tetrahedral cells. Smallest cells of length $\Delta_x \sim 0.1$ mm are located at the main jet exit.

No-slip wall condition are imposed at the injector and outer boundaries. Fully-developed velocity profiles issued from a pipe flow simulation are prescribed at the main inlet as in Rodrigues et al. (2018). Uniform velocity profiles is assumed at the pilot inlet boundary condition. It is assumed that gases entering the pilot inlet have a composition close to the equilibrium state of a

lean ethylene-air mixture at $\phi = 0.9$ and initial temperature of 294 K. The air coflow velocity is set to 0.6 $\mathrm{m} \cdot \mathrm{s}^{-1}$. Lateral walls are adiabatic. The injector walls are considered non-adiabatic, where a temperature distribution is imposed as shown in Fig. 5.3.
LES of the Sandia burner are carried out with the low-Mach, unstructured finite-volume YALES2 code (Moureau et al. (2011)). The convective terms are solved with a 4^{th} order temporal scheme for time integration and a centered 4^{th} order scheme for spatial discretization. The subgrid Reynolds stresses tensor are closed using the sigma model (Nicoud et al. (2011)). The virtual main mechanism, soot sub-mechanism and virtual radiative model presented in Section 5.2, are coupled with the LES solver. The turbulence-chemistry interactions of the main mechanism are solved using the TFLES model from Section 5.3, where the customized flame sensor S_F for virtual chemistry was adapted for ethylene-air sooting flames and validated with laminar thickened premixed flames in Appendix B.1. The SGS flame wrinkling Ξ is closed with the Charlette model (Charlette et al. (2002b); Wang et al. (2011)), with the constant parameter $\beta = 0.5$.
A constant Prandtl number $\mathrm{Pr} = 0.7$ is considered. The Lewis number for virtual species is set to unity expect for the virtual soot species $\mathcal{S}$: $\mathrm{Sc}_k = 0.7$, for k$\neq \mathcal{S}$. Indeed, according to Chapter 3, the Lewis number for the virtual soot species $\mathcal{S}$ is set to $\mathrm{Le}_{\mathcal{S}} = 25$, which corresponds to a laminar Schmidt number of $\mathrm{Sc}_{\mathcal{S}} = 17.5$. The turbulent Schmidt number of all virtual species, including $\mathcal{S}$, is dynamically evaluated as in Moin et al. (1991).
The filtered radiative source term (Eq. 5.3) is approximated by neglecting subgrid-scale temperature and mixture fraction fluctuations: $\overline{\dot{Q}}_r \simeq \dot{Q}_r(\widetilde{T}, \widetilde{Z})$ (Poitou et al. (2008)).
The time and Favre averaging for the variable statistics are performed for 250 ms of physical time.

5.6 Results

5.6.1 Cold flow validation: theoretical round jets

A numerical study similar to Rodrigues (2018) will be performed to characterize the cold flow in the Sandia burner. For this purpose, the pilot flame flow is shut down. LES of the fuel central jet along with the slow-speed air coflow are performed and results are compared to theoretical self-similar round jet solutions from Pope (2000).
Downstream far from the injection nozzle a turbulent round jet with a statistically-stationary and axisymmetric flow presents self-similar mean velocities profiles. The inverse of the axial velocity $\overline{U}_0(x)$ along the burner axis follows a linear

equation as:

$$\frac{U_{bulk}}{\overline{U}_0(x)} = \frac{1}{B}\left(\frac{x - x_0}{D}\right), \tag{5.20}$$

where U_{bulk} and D are the bulk velocity and the diameter of the jet, respectively. B is an empirical constant independent of the Reynolds number and x_0 is the virtual origin. The RMS of the axial velocity U_{rms} compared to the mean axial velocity along the centerline tends asymptotically to a constant value as:

$$\frac{U_{rms}}{\overline{U}_0(x)} \xrightarrow[x\to\infty]{} 0.25. \tag{5.21}$$

These two self-similar profiles are plotted in Fig. 5.4. For the linear profile, the virtual origin is $x_0 = -6$ mm. The empirical constant is $B = 6.8$ close to the value mentioned by Pope and established in Panchapakesan and Lumley (1993). Based on 250 ms of data averaging to statistically converge the flow, a good agreement is observed from about $(x/D \sim 5)$ in Fig. 5.4(a). The $U_{rms}/\overline{U}_0(x)$ profile in Fig. 5.4(b) also reaches to the expected asymptotic value after around 5 diameters.

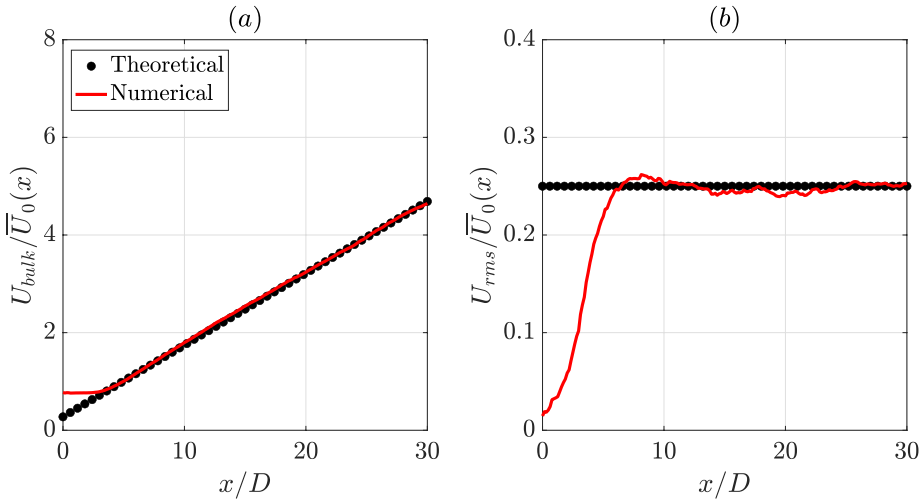

Figure 5.4: *Variation of (a) the mean $\overline{U}_0(x)$ and (b) the RMS of the axial velocity U_{rms} along the burner axis. Comparison between the theoretical self-similar solution and numerical results.*

Radial self-similar profiles are also encountered in this configuration. Pope (2000) has shown that the round jet spreads linearly with a constant spreading rate S_r:

$$r_{1/2} = S_r(x - x_0), \tag{5.22}$$

where $r_{1/2}(x)$ is the half-radius of the jet at position x. According to Panchapakesan and Lumley (1993), the spreading rate is $S_r = 0.096$ for and is independent of the Reynolds number (Pope (2000)). The self-similar mean velocity profile is then expressed using the cross-stream self-similar variable: $\xi = r/r_{1/2}$. In this manner, the self-similar mean velocity ratio $f_{\mathrm{self-sim.}}(\xi, x) = \overline{U}(\xi, x)/\overline{U}_0(x)$ has the same shape independently from the position x considered. However, as the configuration studied here includes a coflow of air, the the mean velocity ratio is rewritten as:

$$f_{\mathrm{self-sim.}}(\xi, x) = \frac{\overline{U}(\xi, x) - \overline{U}(+\infty, x)}{\overline{U}_0(x) - \overline{U}(+\infty, x))}, \tag{5.23}$$

where $\overline{U}(+\infty, x)$ corresponds to the air coflow velocity. Figure 5.5(a) presents numerical results. Very good agreement is obtained with the simulations and the self-similar behavior is well reproduced. Although results are very similar to Rodrigues (2018), the profiles using our numerical methods seems to get better accordance with the theoretical profile around $\xi = 2$.
The fluctuating velocity components are also estimated through the self-similar Reynolds stresses $\overline{u_i u_j}(\xi, x)/\overline{U}_0(x)$. The RMS values of the axial u, tangential u_θ and radial u_r components can be the estimated in the self-similar region in a similar way as in Eq. 5.23 and as a function of ξ. Figure 5.5(b) shows the different self-similar Reynolds stresses at $x = 50$ mm. LES results are challenged against the theoretical fittings (Hussein et al. (1994)). Good results are obtained and it is observed that the agreement is comparable to those obtained by Rodrigues (2018).

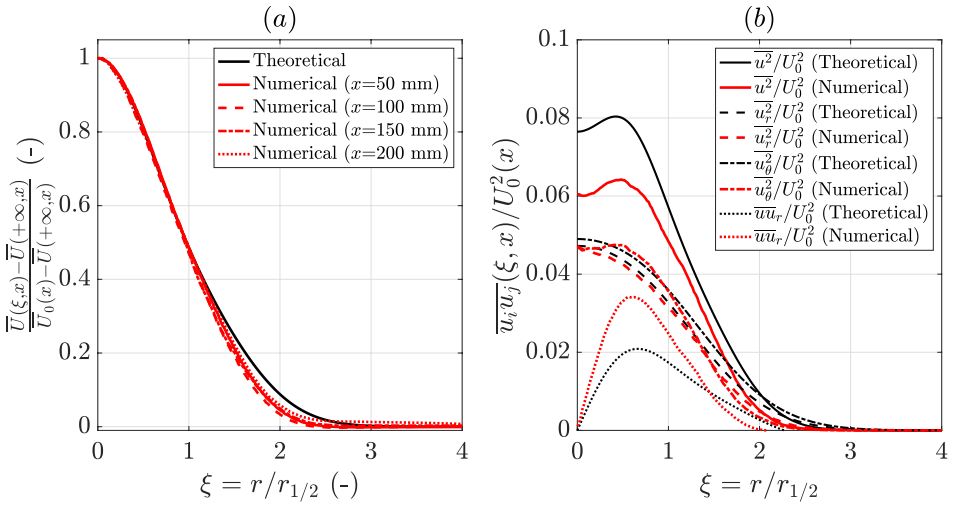

Figure 5.5: *Sandia burner: Radial self-similar solutions. (a) Mean radial velocities for different heights above the burner $x = 50$ mm, 100 mm, 150 mm and 200 mm. (b) Radial self-similar Reynolds stresses at $x = 50$ mm, in order to evaluate the fluctuations of each velocity component.*

5.6.2 Reactive flow validation against experiments

5.6.2.1 *Qualitative analysis*

Figure 5.6 shows instantaneous fields of temperature (a), soot volume fraction (b), soot production rate (c) soot consumption rate (d), gaseous radiative source term (e) and soot radiative source term (f) using the virtual main mechanism, the virtual soot sub-mechanism and the virtual radiation models. The black continuous lines plotted in all fields correspond to the stoichiometric mixture fraction Z_{st} visualizing the flame front. The flame length is about 830 mm ($x/D = 260$), as observed in experimental results (Zhang et al. (2011)).

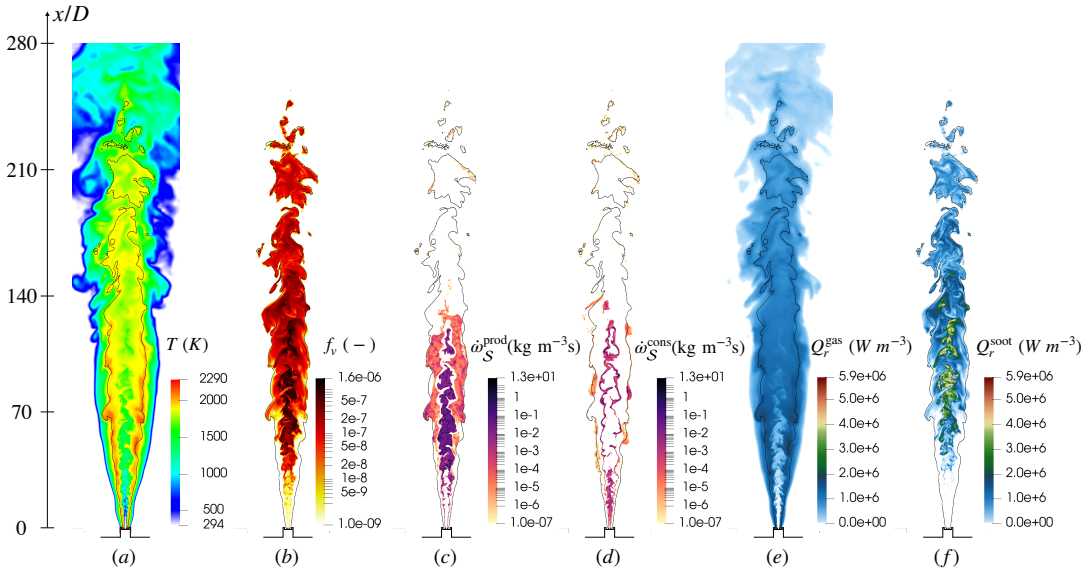

Figure 5.6: *Instantaneous fields of temperature (a), soot volume fraction (b), soot production rate (c) soot consumption rate (d), gas radiative heat loss rates (e) and soot radiative heat loss rate (f). The black continuous line on each figure corresponds to the stoichiometric mixture fraction Z_{st}.*

The temperature field plotted in Fig.5.6(a) shows that radiative heat losses decreases the peak temperature along the stoichiometric iso-line by 250 K.
The maximum soot volume fraction in Fig.5.6(b) reaches 2 ppm which corresponds to the order of magnitude of experimental measurements. The soot source term is split into two parts: production, Fig. 5.6(c) and consumption, Fig. 5.6(d). It shows that soot is formed in the rich region of the flame and then convected downstream where oxidation takes place.
Figures 5.6(e) and 5.6(f) show the gas and solid phase contribution to the radiative source term, respectively. The peak of radiative losses due to soot are greater by a factor of about 4 than those due to the gas phase.

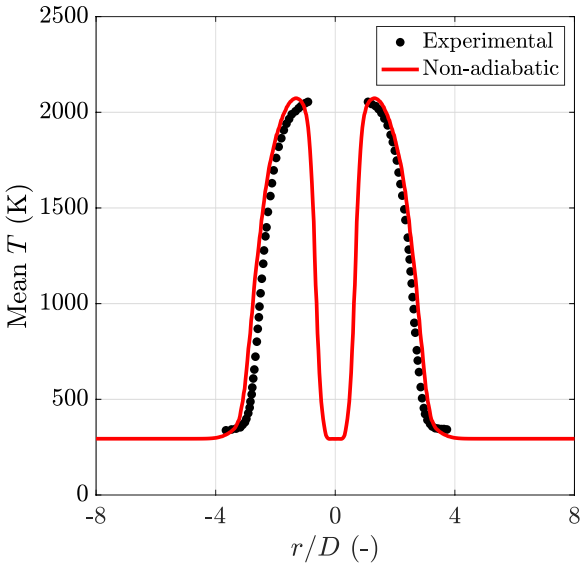

Figure 5.7: *Mean temperature radial profile close to the burner exit at x = 5 mm. Numerical results of non-adiabatic virtual model are compared to experimental measurements from Zhang et al. (2011).*

5.6.2.2 *Temperature and major species*

Figure 5.7 presents the mean temperature radial profile close to the burner exit (x = 5 mm). Numerical data of the non-adiabatic model are consistent with experimental results (Zhang et al. (2011)).
Figure 5.8 shows radial profiles of the mean (top) and RMS (bottom) temperature profiles further downstream, at x/D =134 and x/D =175. Numerical temperature profiles are in good agreement with experimental data Kearney et al. (2015). Solutions exhibit the same accuracy than in Rodrigues et al. (2019), where a tabulated chemistry with detailed database and a Monte Carlo radiative models have been used.
Figure 5.9 presents the Mean (top) and RMS (bottom) profiles of X_{O_2}/X_{N_2}. For both x/D =134 and x/D =175 positions, mean profiles are in good agreement with experimental measurements.

5.6.2.3 *Soot volume fraction*

Figure 5.10 shows radial profiles of mean soot volume fraction profiles at different heights x/D. Numerical results using the non-adiabatic virtual model are compared to experimental data extracted from the ISF database (ISF5 (2021)). The virtual chemistry model fairly reproduces the soot formation. Discrepancies of the results are in conformity with the state of the art of the Sandia flame (Rodrigues et al. (2019); Jain and Xuan (2019)).

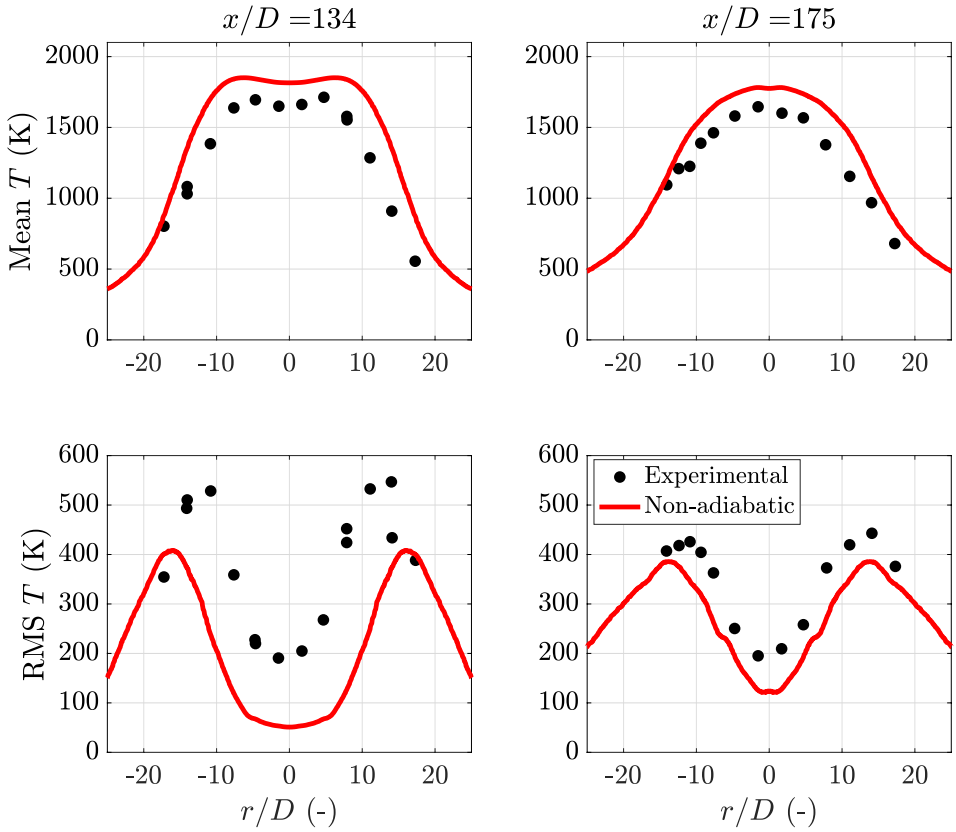

Figure 5.8: *Radial profiles of mean (top) and RMS (bottom) temperatures at $x/D =$ 134 (left) and $x/D = 175$. Numerical results of non-adiabatic case are compared to experimental results from Kearney et al. (2015).*

Figure 5.11 shows radial profiles of RMS soot volume fraction profiles at different heights x/D. Soot fluctuations are retrieved with a good order of magnitude. Discrepancies on the soot levels might be explained by the lack of temperature fluctuations (Fig. 5.8 (bottom)), due to the turbulence-soot-radiation interactions.

5.6.2.4 *Soot intermittency*

The soot intermittency is defined as the probability of soot presence at a given position. The threshold value of soot volume fraction is set to 0.03 ppm as in C.R. Shaddix (2010). Figure 5.12 shows the numerical and experimental intermittency profiles. Experimental data are extracted from C.R. Shaddix (2010). Numerical results of Rodrigues et al. (2019) are also included. Soot presence is overestimated close to the burner. Similar behavior were also found in another turbulent jet configuration Mueller and Pitsch (2012b).

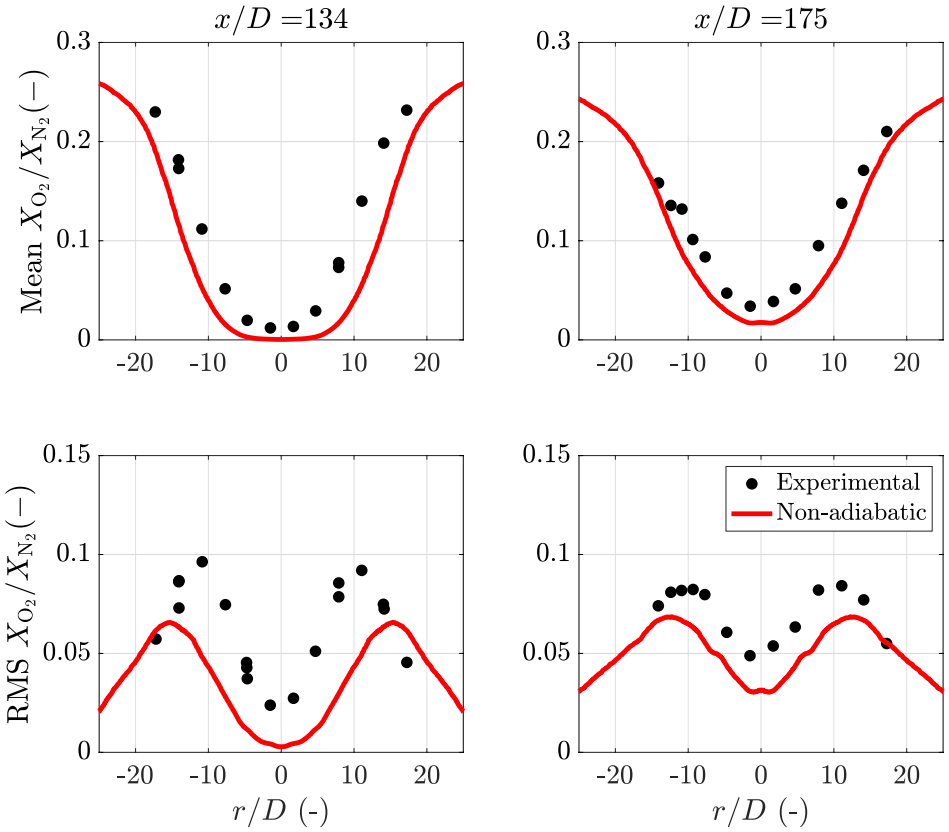

Figure 5.9: *Radial profiles of mean (top) and RMS (bottom)* X_{O_2}/X_{N_2} *at* $x/D =$ 134 *(left) and* $x/D = 175$. *Numerical results of case non-adiabatic are compared to experimental results from Kearney et al. (2015).*

5.6.2.5 *Effect of the radiative heat losses*

To quantify the impact of radiative heat losses, the adiabatic and non-adiabatic virtual models are considered. Mean temperature profiles along the burner axis are plotted in Fig. 5.13. Two experimental points from Fig. 5.8 as well as numerical results from other groups are also included in this figure. A very good response is obtained by the virtual radiative model, where the temperature of the non-adiabatic case agrees with results of other authors.
It should be reminded that Rodrigues et al. (2019) considered a tabulated chemistry for the gas phase based on Wang et al. (2013) and it considers PAHs up to coronene ($C_{24}H_{12}$), an aerosol discrete sectional method for soot formation with a lumped PAH for the nucleation model (Rodrigues et al. (2018)) and Monte Carlo method for radiation (Rodrigues et al. (2019)), transporting a total of 33 variables. Jain and Xuan (2019) considered a tabulated chemistry for the gas phase based on Narayanaswamy et al. (2010) and it considers PAHs

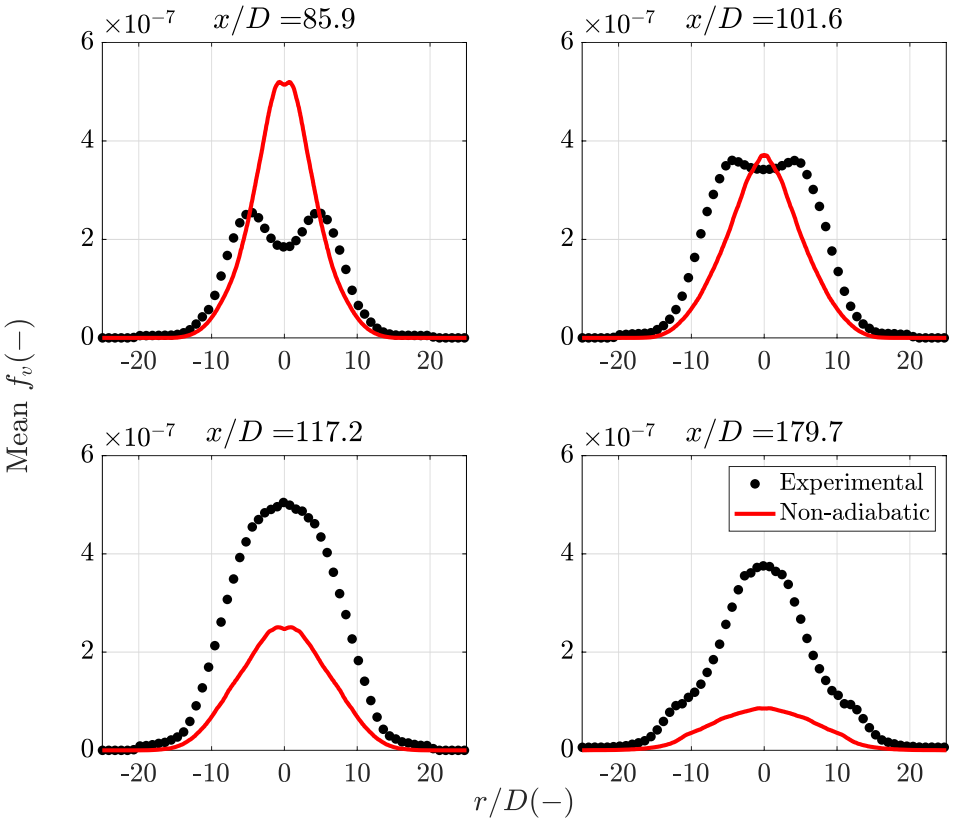

Figure 5.10: *Radial profiles of Mean soot volume fraction at different heights x/D. Numerical results of the non-adiabatic virtual model are compared to experimental data (ISF5 (2021)).*

up to acepyrene ($C_{18}H_{10}$), the soot formation was modeled using a method of moments (Blanquart and Pitsch (2009); Mueller et al. (2009c)) including a multiple species nucleation strategy (Jain and Xuan (2019)) and an optically thin approximation for radiation Barlow et al. (2001).
Figure 5.14 presents numerical results of mean soot volume fraction as well as experimental measurements from ISF5 (2021) along the burner axis. Numerical results of Rodrigues et al. (2019) and Jain and Xuan (2019) are also included. The maximum soot volume fraction is properly predicted by the virtual non-adiabatic model. The virtual adiabatic model underpredicts this maximum value. Soot is formed faster in both virtual models, while the consumption rate is fairly captured after the peak. This is similar to results observed in other turbulent jet flames in the literature (Mueller and Pitsch (2012b); Sewerin and Rigopoulos (2018)). Compared to the other numerical models, the virtual chemistry model is indeed in line with the state of the art of this configuration. In overall, the impact of radiation on the soot volume fraction is of first order.

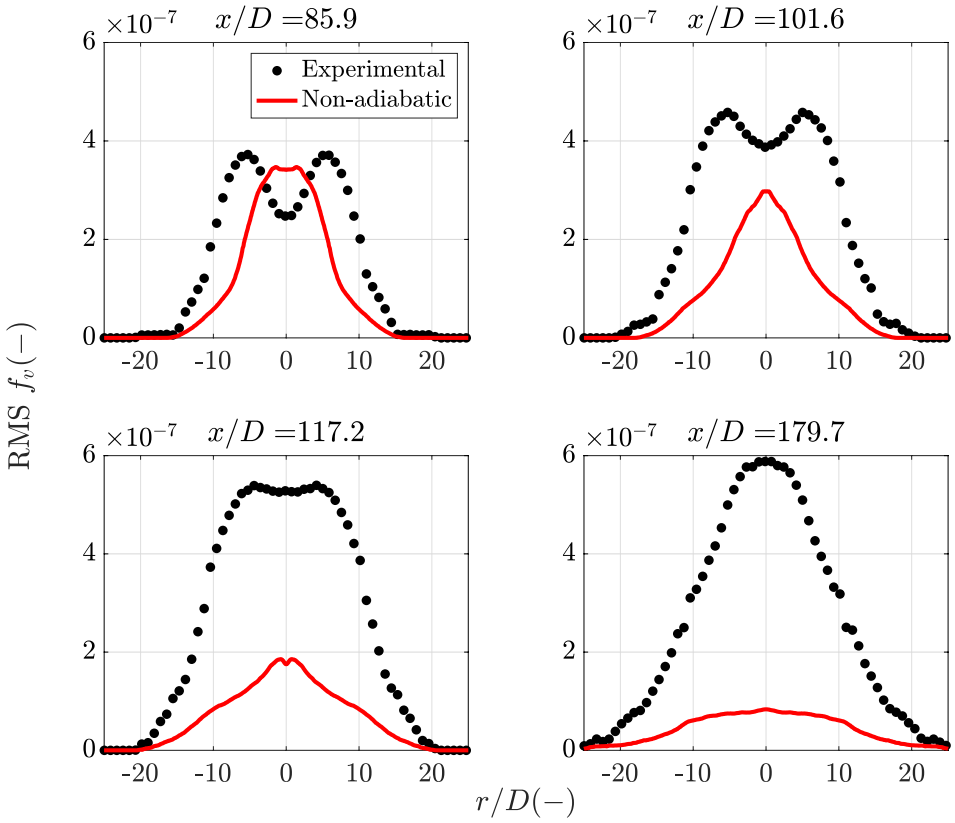

Figure 5.11: *Radial profiles of RMS soot volume fraction at different heights x/D. Numerical results of the non-adiabatic virtual model are compared to experimental data (ISF5 (2021)).*

A total computing time of around 2.2×10^5 CPU-hours was required to cover the 250 ms simulation time, which corresponds to about 3 times less than the total cost made by Rodrigues et al. (2019) and Jain and Xuan (2019). The addition of the radiative term did not impacted the computational cost using the virtual approach.

5.6.2.6 *Effect of the soot SGS model*

A simulation has been performed by neglecting the impact of the subgrid turbulence on the soot chemistry in the post-flame region (i.e. $\eta_r = 1$ for $r = 1$ to 4). Figure 5.15 compares the solution of this simulation against experiments. A significant under-estimation of f_v is revealed when turbulent soot model is turned off.

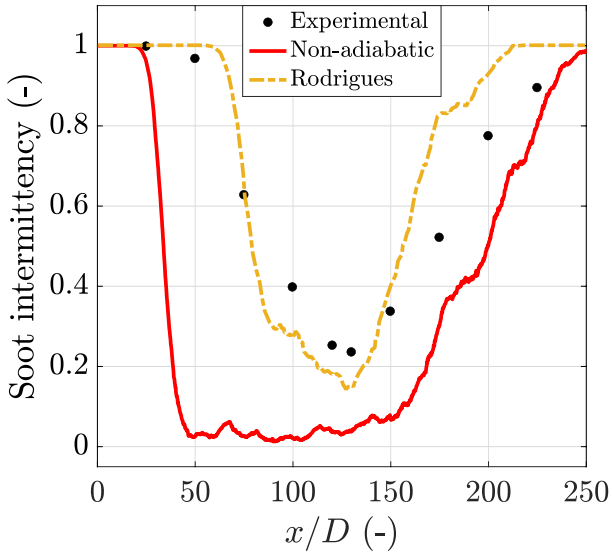

Figure 5.12: *Sandia burner: Soot intermittency profiles along the burner axis.*

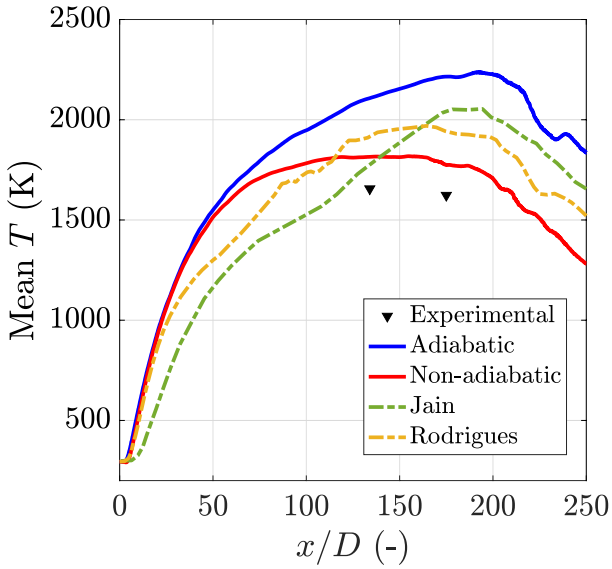

Figure 5.13: *Mean temperature profiles along the centerline. Numerical results of the adiabatic and non-adiabatic virtual models are compared to numerical results of other groups and also two experimental points from Fig. 5.8 are reported.*

5.6.2.7 *Damköhler number analysis*

Figure 5.16 shows the scatter plot of Da^M and Da^s in the radial direction, at four horizontal planes located at $x/D = 9.375$, 31.25, 93.75 and 187.5. The

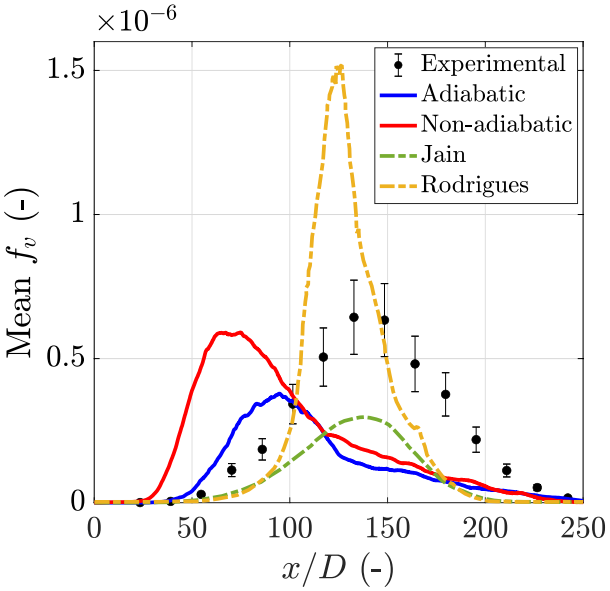

Figure 5.14: *Sandia burner: Mean soot volume fraction profile along the burner axis.*

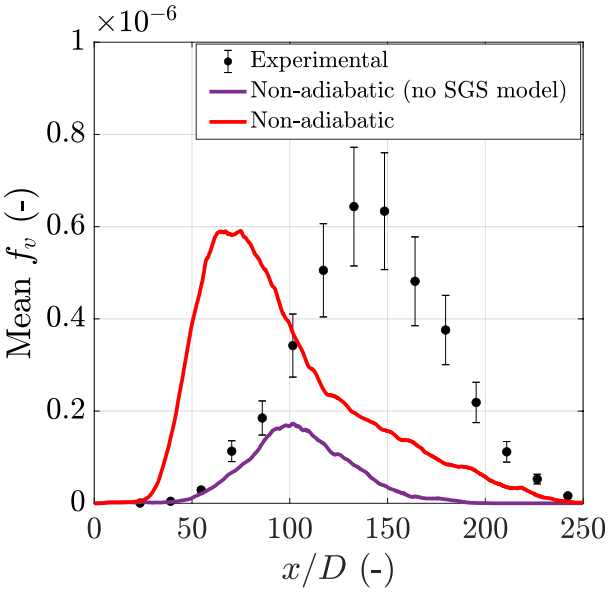

Figure 5.15: *Sandia burner: Mean soot volume fraction profile along the burner axis. Effect of the SGS model on soot formation*

flame front chemistry is already dominant at $x/D = 9.375$ while the soot chemistry starts further downstream, at about $x/D = 31.25$. Soot production activities continue far downstream in the post-flame region, at $x/D = 187.5$, where flame chemistry is completed. As anticipated in section 5.4.2, Da^M is much

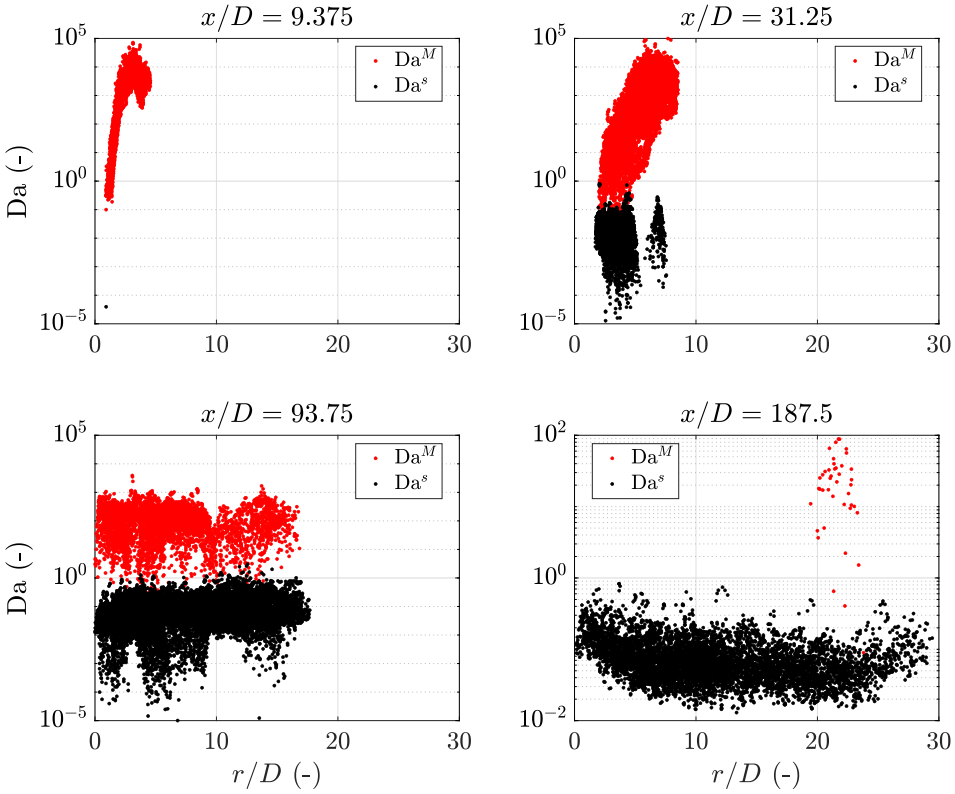

Figure 5.16: *Scatter plot of soot and flame Damköhler numbers in the radial direction at a horizontal section y-z for four vertical positions $x/D = 9.375$, 31.25, 93.75 and 187.5.*

larger than one, which validates the flamelet assumption hypothesis retained to close the filtered reactions rates involved in the main mechanism. Conversely, Da^s is much smaller than one for all the axial position. This observation validates *a posteriori* the PSR model selected to close the filtered reaction rates related to soot virtual chemistry.

5.7 Conclusions and discussion

In this chapter, the novel virtual chemistry and radiative models for sooting flames from Chapter 3 was selected to simulate turbulent sooting flames.
In order to identify the characteristic time scales addressed by the virtual mechanism, a preliminary study of laminar sooting flames using the virtual approach was performed. It is shown that the virtual soot sub-mechanism is associated with long characteristic time scales, corresponding to soot formation at the post-flame region, rather with the virtual main mechanism characteristic time.

Turbulent sooting flames were solved using the LES approach. To capture the flame structure, a TFLES model was chosen. Since this method is in principle dedicated to resolve the turbulent flame front, a new SGS model to capture soot formation in the post-flame region is proposed. The virtual main mechanism covers the thickened flame regime, while the virtual soot sub-mechanism deals with the post-flame PSR-type regime. Then, a new closure is proposed for the SGS soot reaction rates.

Three-dimensional LES of the Sandia flame is performed using the virtual chemistry, radiative and SGS models, giving good agreement with experimental measurements. The new virtual soot sub-mechanism captures well the soot physical phenomena and results are comparable to those of other groups obtained by using detailed models. Also, the new virtual radiative model well provides the heat losses. An analysis of the Damköler numbers is performed *a posteriori* validating the closure for the filtered reaction rates related to soot virtual chemistry. In overall, soot-turbulent-chemistry interactions in the Sandia flame are well retrieved by the non-adiabatic virtual approach.

The proposed virtual model has shown to be very cost-effective for turbulent flame simulations. The CPU cost is reduced by a factor of 3 in the Sandia flame simulation, compared to other state-of-the-art works.

To well recover the position of the soot formation region in the turbulent flame, the building-up process of the virtual chemistry should include additional flame archetypes, as stated in Chapter 3, since pure fuel diffuses into pure air.

A conditional treatment of the SGS model could also be implemented in order to reduce the overprediction of soot formation and oxidation at short characteristic time scales, as shown by Yang et al. (2019).

Conclusion

The main objective of this thesis has been the development of a reduced kinetic mechanism for soot formation prediction in laminar and turbulent combustion simulations at low CPU cost. This kinetic model is based on the virtual chemistry approach, introduced in Cailler (2018) PhD thesis. The principal challenge associated to this methodology was to build-up a unique reduced kinetic model able to accurately reproduce both the flame structure and soot formation. For this purpose, a sophisticated strategy is established to predict temperature and heat release rate together with soot volume fraction. This new virtual approach integrates for the first time both gaseous and solid phases in a virtual mechanism, by bypassing the gas-solid complex formalism without explicit mathematical distinction between both phases. Additionally, a new procedure to include radiative effects in sooting flames has been implemented within the virtual chemistry framework.

The virtual soot mechanism and radiative models in laminar flames are successfully validated in laminar flame simulations. In a first stage, 1-D laminar ethylene-air flames are studied. Adiabatic and non-adiabatic virtual models results exhibit very good agreement compared to detailed chemistry results in canonical premixed and non-premixed configurations. The virtual non-adiabatic model is also challenged in a 1-D burner-stabilized premixed flame configuration, giving good results compared to detailed chemistry computations and experimental measurements. The virtual model is able to predict soot formation in a configuration not initially included in the optimization process. In a second stage, 2-D laminar ethylene-air flames simulations are carried out using the virtual models: a premixed slot burner and a non-premixed coflow burner from the ISF workshop. Numerical results show very good agreement in both configurations. Also, the quality of the virtual model results are comparable to other numerical works in the literature. The computational costs are drastically reduced using the virtual model compared to detailed chemistry computations.

The virtual soot mechanism and radiative models are integrated in the LES framework to simulate a turbulent sooting jet flame. The main mechanism is combined with the Thickened Flame model for LES (TFLES). It has been shown that the virtual sub-mechanism covers a post-flame PSR-type regime, thus TFLES is not sufficient to resolve all source terms in it. A joint TFLES-

PSR closure for the subgrid-scale (SGS) reaction rates of the virtual soot submechanism species is then proposed. 3-D LES of the Sandia flame are performed using the virtual chemistry, radiative and SGS models, showing very good results compared to experimental measurements. Also, numerical results are comparable to those of other works found in the literature, with more detailed models. Here, an important computational cost reduction is observed.

Perspectives

To improve the accuracy of simulation results, the validity domain for the optimization of the virtual soot mechanism should be extended. Particularly, the developed virtual chemistry does not account for the effect of diluted conditions in the reference database. This is mainly observed in simulation results of the 2-D Santoro and 3-D Sandia flames, where at a certain point, soot production was underestimated. The introduction of 1-D non-premixed flames with fuel dilution could help to tackle this limitation. For this purpose, a new strategy in the optimization process may be needed. For instance, a first optimization step could be done by considering simultaneously 1-D premixed flames and 1-D counterflow flames with nitrogen dilution on the fuel side. This might be possible since soot formation in the second configuration takes place near the flame front region. The second optimization step would then be similar to the one made in this work, considering 1-D counterflow non-premixed flames.
In this work, the virtual model was limited to the prediction of soot volume fraction. A better description of soot phenomena would be possible by considering additional features, such as particle number density and/or the total soot surface. In the best scenario, two new virtual scalars would be transported in the virtual chemistry framework. Here, new models for the virtual source scalars would be needed and the optimization process would also change.
Another important aspect to improve is the generation of the architecture of a virtual mechanism. Indeed, the chemical structure of the virtual models is assembled heuristically. An automated process could ease the whole process and also find the most favorable option. Analysis of the chemical species characteristic time scales could be useful to lead the process. In this way, one can better identify the important chemical pathways to the pollutant species under study and find a link to the minimum degree of freedom needed in the combustion equation system. An initial stage of this new concept was developed during this PhD work, which will be resumed in the PhD thesis of Luu (2024).
The virtual radiative model could also be improved to account for more complex radiative effects. For this purpose, developments are in progress in the PhD thesis of Stella (2024).
In the context of LES of turbulent sooting flames, the new SGS model for turbulence-soot interactions could be improved. A conditional treatment to limit soot formation and oxidation at short characteristic time scales could be

implemented, as introduced in Yang et al. (2019). Eventually, the virtual soot mechanism could be validated in other turbulent configuration, such as the DLR confined sooting flame (Geigle et al. (2013)). An extension of the virtual model to operate in pressurized conditions could also be envisaged. To do this, the learning database must include flame elements at the same pressure condition. A "P-log" law for the Arrhenius constant calculation could be introduced in the virtual chemistry framework to account for variable pressure systems.

Appendix A

Virtual soot sub-mechanism considerations

A.1 Soot transport properties in virtual chemistry

Unlike gaseous chemical species, the diffusion effects in soot particles transport are very small and generally, in turbulent flames, the diffusion term in the soot transport equations is neglected due to the very large Schmidt number of soot (Bisetti et al. (2012); Mueller and Pitsch (2012b)). On the other hand, the virtual chemistry approach has been initially modeled using the unitary Lewis number assumption in the sub-mechanism (Cailler et al. (2020); Maio et al. (2020)). Therefore, some precautionary measures must be taken to avoid the excess of diffusive effects. Also other issues may eventually appear during soot formation in the optimization, especially when counterflow diffusion flames are treated.

The reference detailed mechanism accounts for the transport properties of soot BINs (Saggese et al. (2015)) and mixture-averaged transport properties can be calculated in the flame solver REGATH (Darabiha and Candel (1992)). In this case, the diffusion coefficient D_k^d of k^{th} species (with $k = \mathrm{BIN}_5, \ldots, \mathrm{BIN}_{20}$) and the thermal diffusion coefficient $D_T^d = \lambda^d/(\rho^d c_p^d)$ can be compared. Figure A.1 illustrates the variation of $\mathrm{Le}_k = D_T^d/D_k^d$, for $k = \mathrm{BIN}_{10}$, in a 1-D counterflow non-premixed ethylene-air flame, at atmospheric pressure conditions and strain rate $a = 10\ \mathrm{s}^{-1}$. Similar results are obtained when other soot BINs are considered as well as for different strain rates. The green line represents the average value $\overline{\mathrm{Le}}$ of all Le_k's for $k = \mathrm{BIN}_5$ through BIN_{20}. Therefore, in virtual mechanism simulations, for the soot species $\mathcal{S}$, we consider a Lewis number of $\mathrm{Le}_\mathcal{S} = 25$ and a molecular diffusion coefficient $D_\mathcal{S}^v = D^v/\mathrm{Le}_\mathcal{S}$, which is in about the same order of magnitude as $D^d/\overline{\mathrm{Le}}$ in Fig. A.1. For all other virtual species present in the virtual soot sub-mechanism, we will keep the unity Lewis number assumption as in the main mechanism (Cailler et al. (2017)).

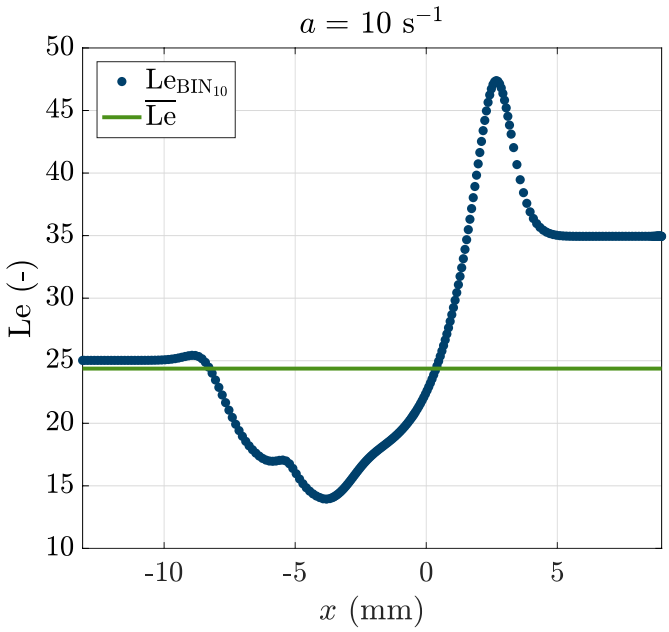

Figure A.1: *Lewis number profiles: comparison for soot transport properties assumptions.*

A.2 Virtual chemistry and radiative models: optimized parameters for ethylene-air flames

Optimized kinetic rates parameter of the virtual main mechanism, the virtual soot sub-mechanism and virtual radiative models are presented in this appendix.
Similar to Cailler et al. (2017), the reaction rate expressions of the main mechanism (virtual reactions R_1^M and R_2^M) are expressed as:

$$q_1^M = A_1^M(Z) \exp\left(\frac{-E_{a,1}^M}{RT}\right) [F]^{n_{F,1}^M} [Ox]^{n_{Ox,1}^M}, \tag{A.1}$$

$$q_2^M = A_2^M \exp\left(\frac{-E_{a,2}^M}{RT}\right) [I]^{n_{I,2}^M(Z)}. \tag{A.2}$$

The vector $\chi^M = (A_r^M, E_{a,r}^M, n_{k,r}^M)$, comprising the pre-exponential constants A_r^M, the activation energies $E_{a,r}^M$ and the reaction rates orders $n_{k,r}^M$ of all k^{th} species and r^{th} virtual reactions, together with the vector of Planck absorption coefficient parameters of Eq. 3.8, $\Gamma^M = (\gamma_0^M, \gamma_1^M, \dots \gamma_5^M)$, are optimized through the evolutionary algorithm proposed by Cailler et al. (2017). The dependence on the mixture fraction Z in the pre-exponential constant $A_r^M(Z)$

is addressed using a correction function defined as $f_r^M(Z) = A_r^M(Z)/A_r^M(Z_{ref})$, where $A_r^M(Z_{ref})$ is the reference pre-exponential factor at stoichiometry ($Z_{ref} = Z_{st} = 0.06350$).
Kinetic constants values of the virtual main mechanism of the reference mixture (Z_{st}) are given in Table A.1. The correction function $f_1^M(Z)$ and the reaction order $n_{I,2}^M(Z)$ are plotted in Fig. A.2, which are valid for both adiabatic (V-A) and radiative (V-R, V-Rs) cases. The Planck absorption coefficient parameters $\gamma_l^M(Z)$ of the virtual radiative model are plotted in Fig. A.3.

Reaction	A_r^M	$E_{a,r}^M$	$n_{k,r}^M$
R_1^M	3.75×10^{22}	3.61×10^4	$n_{1,F}^M = 1.71$ $n_{1,Ox}^M = 1.71$
R_2^M	2.01×10^{22}	1.75×10^4	$n_{1,I}^M = 4.18$

Table A.1: *Kinetic parameters of the virtual main mechanism at the reference mixture composition Z_{st} (Units: cm, s, cal, mol).*

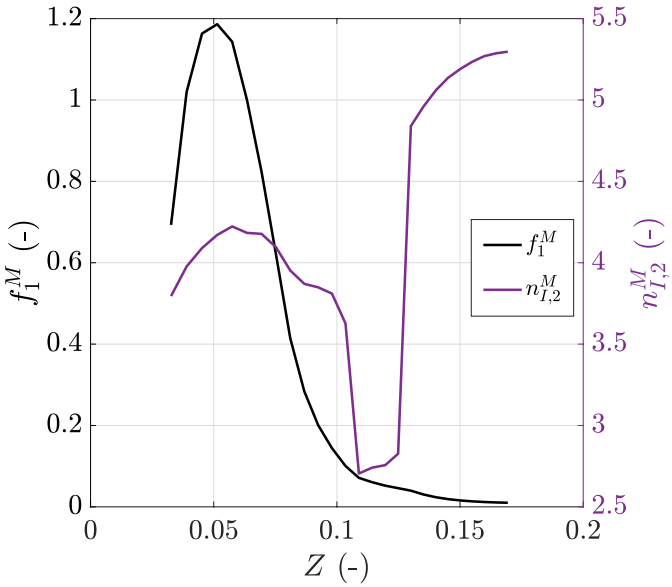

Figure A.2: *Kinetic parameters of the virtual main mechanism: dependence on mixture fraction Z.*

Finally, the kinetic constant elements of the vector χ^s of the virtual soot sub-mechanisms of virtual reactions R_1^s to R_4^s are summarized in the Table A.2. In this case, the reference mixture composition is considered at equivalence ratio of $\phi = 2.3$ ($Z_{\phi=2.3} = 0.13515$) and at adiabatic conditions. It should be noticed that the reaction rate parameters of reaction R_1^s are the same from the main mechanism (see Section 3.3). The correction function for the soot sub-

Reac.	A_r^s	β_r^s	$E_{a,r}^s$	$n_{k,r}^s$	$\alpha_{k,r}^s$
R_1^s	1.14×10^{21}	0	3.61×10^4	$n_{1,F}^s = 1.71$ $n_{1,Ox}^s = 1.71$	$\alpha_{V_1,1}^s = 0.1$ $\alpha_{V_3,1}^s = 0.9$
R_2^s	2.29×10^9	0	4.18×10^4	$n_{V_1,2}^s = 1.44$	$\alpha_{\mathcal{S},2}^s = 0.1$ $\alpha_{V_2,2}^s = 0.9$
R_3^s	3.74×10^{19}	0	1.20×10^4	$n_{\mathcal{S},3}^s = 0.81$ $n_{V_1,3}^s = 1.65$ $n_{V_2,3}^s = 1.11$	$\alpha_{\mathcal{S},3}^s = 1.675$ $\alpha_{V_3,3}^s = 1.325$
R_4^s	6.72×10^{17}	0.52	3.30×10^2	$n_{\mathcal{S},4}^s = 0.97$ $n_{Ox,4}^s = 1.86$ $n_{V_2,4}^s = 0.30$	$\alpha_{Ox,4}^s = 1$ $\alpha_{V_3,4}^s = 2$

Table A.2: *Kinetic rate parameters of the virtual soot sub-mechanism at the reference mixture composition $\phi = 2.3$ (Units: cm, s, cal, mol).*

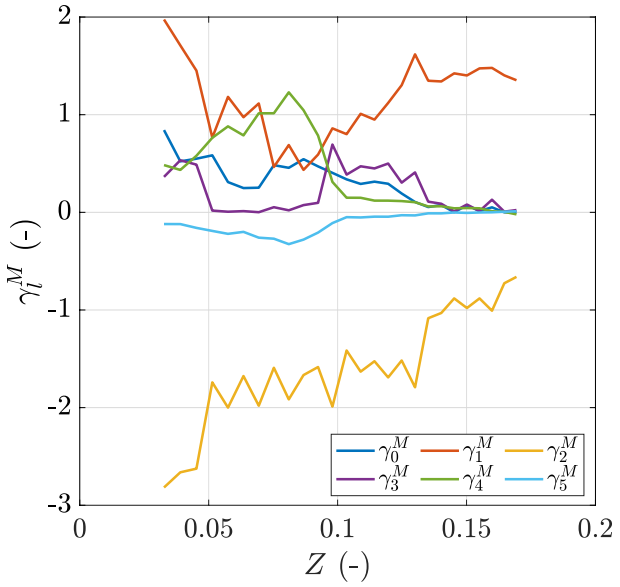

Figure A.3: *Planck absorption coefficient parameters γ_l^M of the gas phase: dependence on mixture fraction Z.*

mechanism is $f_r^s(Z) = A_r^s(Z)/A_r^s(Z_{ref})$, with $Z_{ref} = Z_{\phi=2.3}$. Figure A.4 shows the different kinetic parameters as a function of the mixture fraction Z: $f_r^s(Z)$, $n_{k,r}^s$ and $\alpha_{k,r}^s$, for the adiabatic (V-A) and the radiative (V-R, V-Rs) cases. f_1^s is not shown since is equal to f_1^M (*cf.* subsection 3.3.2), shown in Fig. A.2.

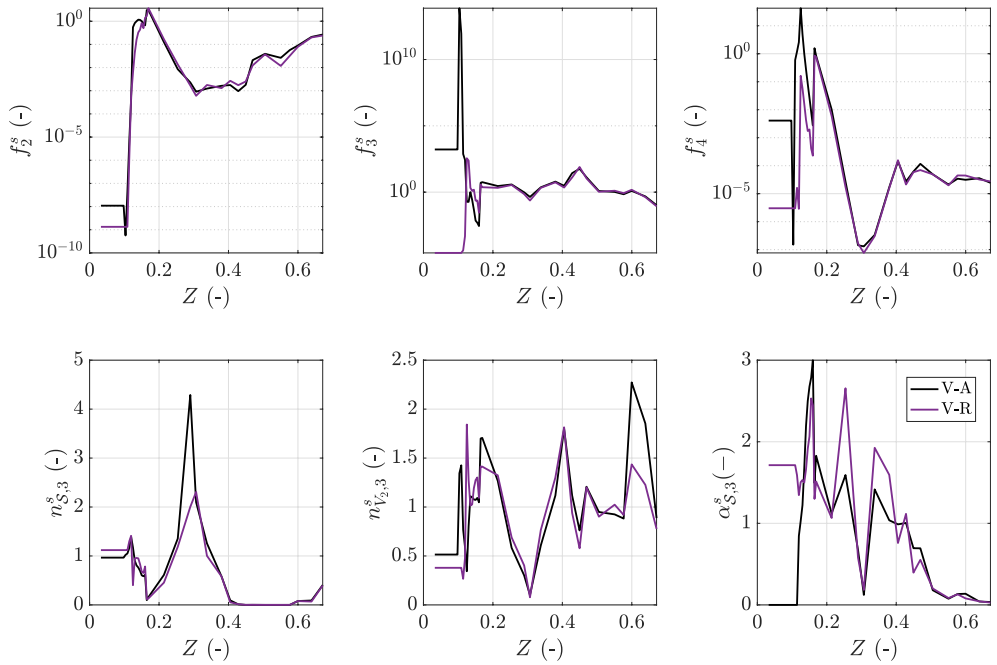

Figure A.4: *Kinetic parameters of the virtual soot sub-mechanism: dependence on mixture fraction Z.*

Appendix B

TFLES validation in virtual chemistry

B.1 Thickening flame model validation

Prior to turbulent calculations, the thickening flame model is validated when used together with the virtual chemistry for the sooting flames simulation. The YALES2 code is employed to realize the computations. Two 1-D premixed ethylene-air flames with equivalence ratio of $\phi = 2.5$ are computed using the adiabatic virtual chemistry, where the first one is fully-resolved and the other one is thickened. A uniform element size of $\Delta_x = 0.5$ mm is considered for the numerical grid of the thickened flame. The flame sensor determination through Eq. 5.7 does not need to consider the soot source term $\dot{\omega}_{\mathcal{S}}$, since soot is primarily formed in the post-flame region, as it was observed in Figure 5.1. The species associated thickening from Eq. 5.9 is performed in order to determine the global thickening factor F_T, which is applied in the flame region to diffusive and chemical source terms (see Eqs. 5.4, 5.5 and 5.14). No wrinkling compensation is needed in a laminar flame, thus Ξ_Δ is set to one. Results are plotted in Fig. B.1, where the temperature and soot volume fraction profiles of the thickened flame are compared to those of the fully-resolved flame. The flame front is well resolved and the final temperature level is achieved. The thickening operation does not change the laminar flame speed in this operating condition. The soot production is slightly delayed by the artificial thickening, but the soot volume fraction f_v level remains practically unaltered.

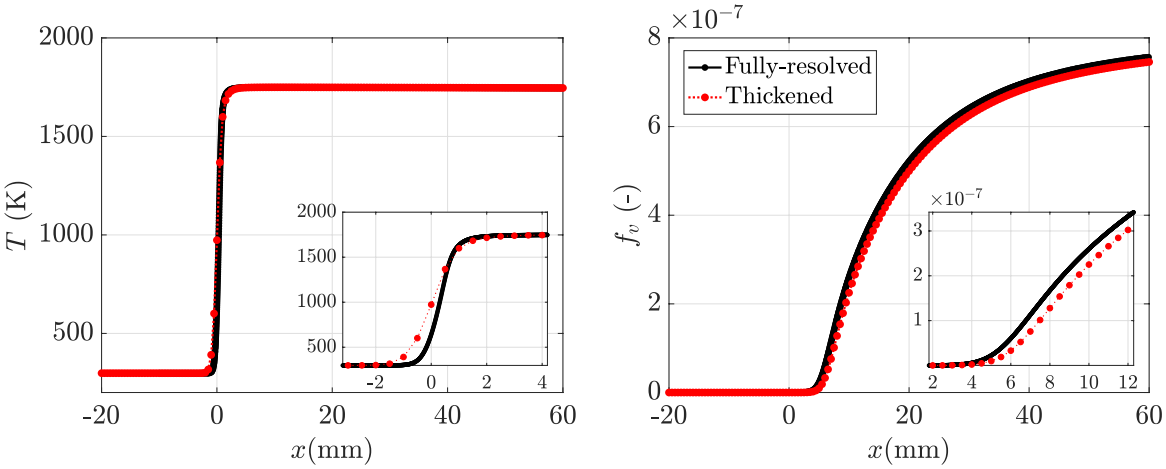

Figure B.1: *Temperature (left) and soot volume fraction (right) profiles of premixed ethylene-air flames with equivalence ratio $\phi = 2.5$: comparison of the fully-resolved and thickened flames. Each filled circle marker indicates a point in the numerical grid.*

Synthèse en Français

Introduction

Afin de réduire les émissions de polluants dans les applications pratiques de combustion, il faut développer des dispositifs de combustion plus efficaces. La formation des suies est l'un des sujets les plus difficiles dans ce domaine caractérisé par la complexité des phénomènes qui se produisent tout au long des processus de combustion. En fait, la production des suies est fortement couplée au mouvement de l'écoulement turbulent ainsi qu'aux réactions chimiques et à la température. Les simulations numériques de la combustion turbulente sont particulièrement exigeantes en termes de CPU pour les flammes suitées. Une solution typique pour réduire le temps de simulation est d'utiliser une cinétique chimique réduite et des modèles simplifiés pour les particules solides.
Le modèle de chimie virtuelle développé par Cailler (2018) est étendu ici pour combiner ces caractéristiques. Il consiste en un formalisme mathématique incluant des espèces virtuelles et des réactions virtuelles, dont les paramètres thermochimiques sont optimisés afin de décrire un système de combustion. Les propriétés thermochimiques sont entraînées par un algorithme génétique, en utilisant une base de données d'apprentissage constituée d'éléments de flamme de référence. Il est ainsi possible de reproduire de multiples régimes de combustion et conditions de fonctionnement.

Objetifs de la thèse

La formulation du modèle virtuel est basée sur les données chimiques fournies par un mécanisme détaillé fiable et précis. L'approche de la chimie virtuelle reste puissante et flexible : on peut développer un mécanisme simplifié *a priori*, sans avoir besoin d'effectuer un réglage *ad hoc* des paramètres en fonction des données expérimentales. Dans ce cadre, l'objectif de cette thèse est de développer un mécanisme virtuel réduit pour la prédiction de la formation des suies dans la combustion ethylène-air à faible coût CPU. Une hypothèse de modélisation sophistiquée est proposée pour limiter la propagation des erreurs dans la transition gaz-solide. De plus, une nouvelle procédure basée sur l'approche virtuelle est est développée pour prendre en compte les pertes thermiques radia-

tives. Les modèles résultants sont d'abord validés dans des flammes laminaires 1-D éthylène-air. Ils sont ensuite appliqués aux configurations de flammes laminaires 2-D. Enfin, un modèle pour les interactions turbulence-suies à l'échelle sous-maille est développé pour les Simulations aux Grandes Echelles (LES) des flammes turbulentes suitées.

Plan de la thèse

Le chapitre 2 introduit l'approche de la chimie virtuelle. La méthodologie de la chimie virtuelle est d'abord présentée. Ensuite, le mécanisme principal virtuel est présenté, qui couvre la prédiction de la structure de la flamme. L'état de l'art des sous-mécanismes virtuels pour la prédiction des polluants est présenté : des exemples de modèles virtuels de CO et de NOx dans des flammes laminaires sont montrés. Enfin, les équations de conservation de l'écoulement réactif dans le cadre de la chimie virtuelle sont décrites.
Dans le chapitre 3, le sous-mécanisme virtuel des suies est développé. Le principe de la chimie virtuelle est d'abord introduit pour les flammes laminaires. L'architecture du schéma virtuel pour les suies et la stratégie d'optimisation sont décrites. Ensuite, les modèles virtuels de rayonnement des gaz et des suies sont décrits. La configuration de l'optimisation est exposée : la base de données d'apprentissage utilisant les solutions chimiques détaillées et les cas de calcul sont montrés. Les nouveaux mécanismes et sous-mécanismes virtuels, ainsi que les modèles radiatifs virtuels sont validés sur des flammes laminaires éthylène-air 1D. Enfin, les modèles virtuels sont mis à l'épreuve dans deux configurations de flammes laminaires 2-D : un brûleur à fente prémélangé et un brûleur à co-courant non prémélangé.
Les bases de la modélisation de la combustion turbulente sont présentées dans le chapitre 4. Les différentes méthodes numériques de la combustion turbulente sont d'abord introduites. Ensuite, les équations gouvernant l'écoulement réactif dans le cadre de la LES sont présentées : une description du formalisme LES est faite, suivie de la dérivation des équations d'équilibre filtrées. Enfin, les modèles de combustion turbulente dans LES sont présentés, avec un accent particulier sur le modèle de Flamme Epaissie dans la LES (Thickened Flame model for LES en anglais, TFLES).
Le chapitre 5 est consacré à l'application des nouveaux modèles virtuels de suie aux flammes turbulentes de suie. L'étude commence par l'introduction du modèle de combustion laminaire et se poursuit par son couplage à la résolution des flammes turbulentes. Ensuite, des analyses d'échelle de temps et de longueur des flammes laminaires sont effectuées, ce qui permet d'identifier les régimes de combustion dans les flammes de turbulentes suitées. Un modèle à l'échelle sous-maille est ensuite proposé pour tenir compte des interactions turbulence-suies en utilisant le sous-mécanisme virtuel. Ensuite, une configuration de flamme turbulente suitée 3-D est introduite, où une description des

configurations expérimentales et numériques est rapportée. Enfin, les résultats numériques utilisant les nouveaux modèles virtuels sont validés dans le cas des écoulements froids et réactifs.

Conclusions gènèrales

Un mécanisme cinétique réduit a été développée pour la prédiction de la formation des suies dans des simulations de combustion laminaire et turbulente à faible coût CPU. Ce modèle cinétique est basé sur l'approche de la chimie virtuelle, introduite dans la thèse de doctorat de Cailler (2018). Le principal défi associé à cette méthodologie était de construire un modèle cinétique réduit capable de reproduire avec précision à la fois la structure de la flamme et la formation des suies. A cette fin, une stratégie sophistiquée est établie pour prédire la température et le taux de dégagement de chaleur ainsi que la fraction volumique des suies. Cette nouvelle approche virtuelle intègre pour la première fois les phases gazeuse et solide dans un mécanisme virtuel, en contournant le formalisme complexe gaz-solide sans distinction mathématique explicite entre les deux phases. En outre, une nouvelle procédure permettant d'inclure les effets radiatifs dans les flammes suitées a été mise en œuvre dans le cadre de la chimie virtuelle.
Le mécanisme virtuel des suies et les modèles radiatifs dans les flammes laminaires sont validés avec succès dans des simulations de flammes laminaires. Dans un premier temps, des flammes laminaires éthylène-air 1-D sont étudiées. Les résultats des modèles virtuels adiabatiques et non-adiabatiques montrent un très bon accord par rapport aux résultats de la chimie détaillée dans les configurations canoniques prémélangées et non-prémélangées. Le modèle virtuel non-adiabatique est également mis au défi dans une configuration de flamme prémélangée 1-D stabilisée par un brûleur, donnant de bons résultats comparés aux calculs de chimie détaillée et aux mesures expérimentales. Ainsi ce modèle virtuel est capable de prédire la formation des suies dans une configuration qui n'était pas initialement incluse dans le processus d'optimisation.
Dans un deuxième temps, des simulations de flammes laminaires 2-D éthylène-air sont effectuées en utilisant les modèles virtuels : un brûleur à fente prémélangé et un brûleur à co-courant non prémélangé de l'atelier ISF. Les résultats numériques montrent un très bon accord dans les deux configurations. De plus, la qualité des résultats du modèle virtuel est comparable à celle d'autres travaux numériques de la littérature. Les coûts de calcul sont considérablement réduits en utilisant le modèle virtuel par rapport aux calculs de chimie détaillée.
Le mécanisme virtuel des suies et le modèle radiatif sont intégrés dans le cadre du LES pour simuler une flamme jet turbulente suitée. Le mécanisme principal est combiné avec le modèle TFLES. Il a été démontré que le sous-mécanisme virtuel pour les suies couvre un régime de type PSR post-flamme, et que TFLES n'est donc pas suffisant pour résoudre tous les termes sources qu'il contient.

Une fermeture conjointe TFLES-PSR pour les taux de réaction à l'échelle de la sous-maille (SGS) des espèces du sous-mécanisme virtuel des suies est alors proposée. Des simulations LES 3D de la flamme Sandia sont réalisées en utilisant les modèles virtuels de chimie, radiatif et SGS, montrant de très bons résultats comparés aux mesures expérimentales. De plus, les résultats numériques sont comparables à ceux d'autres travaux trouvés dans la littérature, avec des modèles plus détaillés. Ici, une réduction importante du coût de calcul est observée.

References

Akridis, P. and S. Rigopoulos (2017). Modelling of soot formation in laminar diffusion flames using a comprehensive cfd-pbe model with detailed gas-phase chemistry. *Combustion Theory and Modelling 21*(1), 35–48. *(p. 38)*

Alam, M. K. (1987). The effect of van der waals and viscous forces on aerosol coagulation. *Aerosol Science and Technology 6*(1), 41–52. *(p. 27)*

Allouis, C., B. Apicella, R. Barbella, F. Beretta, A. Ciajolo, and A. Tregrossi (2003). Monitoring of fuel consumption and aromatics formation in a kerosene spray flame as characterized by fluorescence spectroscopy. *Chemosphere 51*(10), 1097–1102. *(p. 14)*

Angelberger, D., D. Veynante, F. Egolfopoulos, and T. Poinsot (1998). Large Eddy Simulations of combustion instabilities in premixed flames. In *Summer Program*, pp. 61–82. Citeseer. *(p. 89)*

Appel, J., H. Bockhorn, and M. Frenklach (2000, 4). Kinetic modeling of soot formation with detailed chemistry and physics: laminar premixed flames of c2 hydrocarbons. *Combustion and Flame 121*(1–2), 122–136. *(p. 78)*

Balthasar, M. and M. Kraft (2003). A stochastic approach to calculate the particle size distribution function of soot particles in laminar premixed flames. *Combustion and Flame 133*(3), 289 – 298. *(p. 29, 30)*

Barlow, R., A. Karpetis, J. Frank, and J.-Y. Chen (2001). Scalar profiles and no formation in laminar opposed-flow partially premixed methane/air flames. *Combustion and flame 127*(3), 2102–2118. *(p. 65, 67, 110)*

Bisetti, F., G. Blanquart, M. E. Mueller, and H. Pitsch (2012, 1). On the formation and early evolution of soot in turbulent nonpremixed flames. *Combust. Flame 159*(1), 317–335. *(p. 38, 121)*

Blacha, T., M. Di Domenico, P. Gerlinger, and M. Aigner (2012, 1). Soot predictions in premixed and non-premixed laminar flames using a sectional approach for pahs and soot. *Combustion and Flame 159*(1), 181–193. *(p. 7, 30, 39, 78)*

Blanquart, G., P. Pepiot-Desjardins, and H. Pitsch (2009). Chemical mechanism for high temperature combustion of engine relevant fuels with emphasis on soot precursors. *Combustion and Flame 156*(3), 588 – 607. *(p. 38)*

Blanquart, G. and H. Pitsch (2007). A joint volume-surface-hydrogen multivariate model for soot formation. In *Combustion Generated Fine Car-*

bonaceous Particles. Henning Bockhorn. *(p. 14, 33, 62)*

Blanquart, G. and H. Pitsch (2009). Analyzing the effects of temperature on soot formation with a joint volume-surface-hydrogen model. *Combustion and Flame 156*(8), 1614 – 1626. *(p. 26, 38, 110)*

Bodor, A. L., B. Franzelli, T. Faravelli, and A. Cuoci (2019). A post processing technique to predict primary particle size of sooting flames based on a chemical discrete sectional model: Application to diluted coflow flames. *Combustion and Flame 208*, 122 – 138. *(p. 33, 77)*

Boger, M. and D. Veynante (2000). Large eddy simulation of a turbulent premixed v-shaped flame. *Advances in Turbulence VIII*, 449–452. *(p. 89)*

Boger, M., D. Veynante, H. Boughanem, and A. Trouvé (1998). Direct numerical simulation analysis of flame surface density concept for large eddy simulation of turbulent premixed combustion. In *Symposium (International) on Combustion*, Volume 27, pp. 917–925. Elsevier. *(p. 89)*

Bouaniche, A., J. Yon, P. Domingo, and L. Vervisch (2020). Analysis of the soot particle size distribution in a laminar premixed flame: A hybrid stochastic/fixed-sectional approach. *Flow, Turbulence and Combustion 104*(2), 753–775. *(p. 30)*

Bradley, D., L. Kwa, A. Lau, M. Missaghi, and S. Chin (1988). Laminar flamelet modeling of recirculating premixed methane and propane-air combustion. *Combustion and Flame 71*(2), 109–122. *(p. 22)*

Brookes, S. J. and J. B. Moss (1999). Predictions of soot and thermal radiation properties in confined turbulent jet diffusion flames. *Combustion and Flame 116*(4), 486–503. *(p. 34)*

Brown, N. J., G. Li, and M. L. Koszykowski (1997). Mechanism reduction via principal component analysis. *International Journal of Chemical Kinetics 29*(6), 393–414. *(p. 20)*

Butler, T. and P. O'Rourke (1977). A numerical method for two dimensional unsteady reacting flows. In *Symposium (international) on combustion*, Volume 16, pp. 1503–1515. Elsevier. *(p. 88)*

Cailler, M. (2018). *Virtual chemical mechanisms optimized to capture pollutant formation in turbulent flames*. Ph. D. thesis, Ecole CentraleSupélec, Université Paris-Saclay. *(p. xiv, 8, 46, 47, 48, 52, 54, 58, 117, 129, 131)*

Cailler, M., N. Darabiha, and B. Fiorina (2020). Development of a virtual optimized chemistry method. Application to hydrocarbon/air combustion. *Combustion and Flame 211*, 281 – 302. *(p. xiv, 8, 46, 47, 51, 52, 60, 61, 64, 66, 93, 121)*

Cailler, M., N. Darabiha, D. Veynante, and B. Fiorina (2017). Building-up virtual optimized mechanism for flame modeling. *Proceedings of the Combustion Institute 36*(1), 1251 – 1258. *(p. 23, 46, 47, 49, 51, 60, 61, 65, 66, 93, 94, 121, 122)*

Cailler, M., R. Mercier, V. Moureau, N. Darabiha, and B. Fiorina. (2017). LES simulation of the Cambridge stratified flame using optimized virtual mechanisms. In *55th AIAA Aerospace Sciences Meeting Grapevine, Texas,*

USA, AIAA, Number AIAA paper 2017-1471. *(p. 8, 52, 88, 93, 97)*

Cain, J. P., P. L. Gassman, H. Wang, and A. Laskin (2010). Micro-ftir study of soot chemical compositionâ€"evidence of aliphatic hydrocarbons on nascent soot surfaces. *Physical Chemistry Chemical Physics 12*(20), 5206–5218. *(p. 14)*

Cavaliere, A., R. Barbella, A. Ciajolo, A. D'anna, and R. Ragucci (1994). Fuel and soot oxidation in diesel-like conditions. *Symposium (International) on Combustion 25*(1), 167 – 174. Twenty-Fifth Symposium (International) on Combustion. *(p. 16)*

Celnik, M., R. Patterson, M. Kraft, and W. Wagner (2007). Coupling a stochastic soot population balance to gas-phase chemistry using operator splitting. *Combustion and Flame 148*(3), 158 – 176. *(p. 7, 30)*

Chang, Y., M. Jia, B. Niu, Z. Xu, Z. Liu, Y. Li, and M. Xie (2018). Construction of a skeletal oxidation mechanism of n-pentanol by integrating decoupling methodology, genetic algorithm, and uncertainty quantification. *Combustion and Flame 194*, 15 – 27. *(p. 20)*

Charlette, F., C. Meneveau, and D. Veynante (2002a). A power-law flame wrinkling model for {LES} of premixed turbulent combustion part i: non-dynamic formulation and initial tests. *Combustion and Flame 131*(1–2), 159 – 180. *(p. 89)*

Charlette, F., C. Meneveau, and D. Veynante (2002b). A power-law flame wrinkling model for {LES} of premixed turbulent combustion part ii: dynamic formulation. *Combustion and Flame 131*(1–2), 181 – 197. *(p. 89, 103)*

Chatelier, A., T. Guiberti, R. Mercier, N. Bertier, B. Fiorina, and T. Schuller (2019). Experimental and numerical investigation of the response of a swirled flame to flow modulations in a non-adiabatic combustor. *Flow, Turbulence and Combustion 102*(4), 995–1023. *(p. 22, 23)*

Chen, J. (1997). Development of reduced mechanisms for numerical modelling of turbulent combustion. In *Workshop on Numerical Aspects of Reduction in Chemical Kinetics, CERMICS-ENPC, Cité Descartes, Champus sur Marne, France*. *(p. 20)*

Chernov, V., M. J. Thomson, S. B. Dworkin, N. A. Slavinskaya, and U. Riedel (2014). Soot formation with c1 and c2 fuels using an improved chemical mechanism for pah growth. *Combustion and Flame 161*(2), 592 – 601. *(p. 17, 18)*

Chong, S. T., M. Hassanaly, H. Koo, M. E. Mueller, V. Raman, and K.-P. Geigle (2018). Large eddy simulation of pressure and dilution-jet effects on soot formation in a model aircraft swirl combustor. *Combustion and Flame 192*, 452–472. *(p. 37)*

Chong, S. T., V. Raman, M. E. Mueller, P. Selvaraj, and H. G. Im (2019). Effect of soot model, moment method, and chemical kinetics on soot formation in a model aircraft combustor. *Proceedings of the Combustion Institute 37*(1), 1065–1074. *(p. xiv, 37, 39, 40, 92)*

Ciajolo, A., A. Tregrossi, R. Barbella, R. Ragucci, B. Apicella, and M. de Joannon (2001). The relation between ultraviolet-excited fluorescence spectroscopy and aromatic species formed in rich laminar ethylene flames. *Combustion and Flame 125*(4), 1225 – 1229. *(p. 14)*

Colin, O., F. Ducros, D. Veynante, and T. Poinsot (2000). A thickened flame model for large eddy simulations of turbulent premixed combustion. *Physics of Fluids (1994-present) 12*(7), 1843–1863. *(p. 88, 89, 93, 96)*

C.R. Shaddix, J. Zhang, R. S. J. D. J. O. S. K. L. P. H. W. (2010). Understanding and predicting soot generation in turbulent non-premixed jet flames. Technical Report SAND2010-7178, Sandia Report. *(p. 108)*

Cuoci, A., A. Frassoldati, T. Faravelli, and E. Ranzi (2013a). A computational tool for the detailed kinetic modeling of laminar flames: Application to c2h4/ch4 coflow flames. *Combustion and Flame 160*(5), 870–886. *(p. 75, 77)*

Cuoci, A., A. Frassoldati, T. Faravelli, and E. Ranzi (2013b). Numerical modeling of laminar flames with detailed kinetics based on the operator-splitting method. *Energy & fuels 27*(12), 7730–7753. *(p. 75, 77)*

Curran, H. J. (2019). Developing detailed chemical kinetic mechanisms for fuel combustion. *Proceedings of the Combustion Institute 37*(1), 57 – 81. *(p. xiii, 12, 16, 17, 18)*

D'Anna, A. (2007). Particle inception and growth: experimental evidences and a modelling attempt. In *Combustion Generated Fine Carbonaceous Particles*, pp. 289–320. Henning Bockhorn, Karlsruhe University Press, Karlsruhe. *(p. 14)*

D'Anna, A. and J. Kent (2008). A model of particulate and species formation applied to laminar, nonpremixed flames for three aliphatic-hydrocarbon fuels. *Combustion and Flame 152*(4), 573 – 587. *(p. 32)*

Darabiha, N. and S. Candel (1992, 2015/09/11). The influence of the temperature on extinction and ignition limits of strained hydrogen-air diffusion flames. *Combustion Science and Technology 86*(1-6), 67–85. *(p. 8, 66, 67, 121)*

Dellinger, N., N. Bertier, F. Dupoirieux, and G. Legros (2020). Hybrid eulerian-lagrangian method for soot modelling applied to ethylene-air premixed flames. *Energy 194*, 116858. *(p. 30)*

Dempsey, A. B., S. J. Curran, and R. M. Wagner (2016). A perspective on the range of gasoline compression ignition combustion strategies for high engine efficiency and low nox and soot emissions: Effects of in-cylinder fuel stratification. *International Journal of Engine Research 17*(8), 897–917. *(p. xiii, 5, 6)*

Derjaguin, B. V., A. I. Storozhilova, and Y. I. Rabinovich (1966, 1). Experimental verification of the theory of thermophoresis of aerosol particles. *J. Colloid Interface Sci. 21*(1), 35–58. *(p. 25)*

Di Domenico, M., P. Gerlinger, and M. Aigner (2010). Development and

validation of a new soot formation model for gas turbine combustor simulations. *Combustion and flame 157*(2), 246–258. *(p. 78)*

Dobbins, R. A. (2007). Hydrocarbon nanoparticles formed in flames and diesel engines. *Aerosol Science and Technology 41*(5), 485–496. *(p. 14)*

Eaves, N. A., Q. Zhang, F. Liu, H. Guo, S. B. Dworkin, and M. J. Thomson (2016). Coflame: A refined and validated numerical algorithm for modeling sooting laminar coflow diffusion flames. *Computer Physics Communications 207*, 464 – 477. *(p. 17)*

Eberle, C., P. Gerlinger, and M. Aigner (2017). A sectional pah model with reversible pah chemistry for cfd soot simulations. *Combustion and Flame 179*, 63–73. *(p. 7, 30, 31, 39)*

Egolfopoulos, F. N., N. Hansen, Y. Ju, K. Kohse-Höinghaus, C. K. Law, and F. Qi (2014). Advances and challenges in laminar flame experiments and implications for combustion chemistry. *Progress in Energy and Combustion Science 43*, 36–67. *(p. 17)*

El-Asrag, H., T. Lu, C. K. Law, and S. Menon (2007). Simulation of soot formation in turbulent premixed flames. *Combustion and Flame 150*(1), 108–126. *(p. 92)*

El-Leathy, A., F. Xu, and G. Faeth (2002, 2015/07/22). *Soot surface growth and oxidation in laminar unsaturated-hydrocarbon/air diffusion flames*. American Institute of Aeronautics and Astronautics. *(p. 28)*

Epstein, P. S. (1924, Jun). On the resistance experienced by spheres in their motion through gases. *Phys. Rev. 23*, 710–733. *(p. 25)*

Felden, A., L. Esclapez, E. Riber, B. Cuenot, and H. Wang (2018). Including real fuel chemistry in LES of turbulent spray combustion. *Combustion and Flame 193*, 397–416. *(p. 20, 21)*

Felden, A., E. Riber, and B. Cuenot (2018). Impact of direct integration of analytically reduced chemistry in LES of a sooting swirled non-premixed combustor. *Combustion and Flame 191*, 270–286. *(p. 7, 20, 21, 37)*

Fernandez-Tarrazo, E., A. L. Sánchez, A. Liñán, and F. A. Williams (2006). A simple one-step chemistry model for partially premixed hydrocarbon combustion. *Combustion and Flame 147*(1), 32–38. *(p. 23)*

Fiorina, B. (2019). Accounting for complex chemistry in the simulations of future turbulent combustion systems. In *AIAA Scitech 2019 Forum*, pp. 0995. *(p. xiii, 7, 19)*

Fiorina, B., O. Gicquel, L. Vervisch, S. Carpentier, and N. Darabiha (2005). Premixed turbulent combustion modeling using tabulated detailed chemistry and pdf. *Proceedings of the Combustion Institute 30*(1), 867–874. *(p. 22, 62)*

Fiorina, B., R. Mercier, G. Kuenne, A. Ketelheun, A. Avdić, J. Janicka, D. Geyer, A. Dreizler, E. Alenius, C. Duwig, et al. (2015). Challenging modeling strategies for les of non-adiabatic turbulent stratified combustion. *Combustion and Flame 162*(11), 4264–4282. *(p. 7, 22)*

Fiorina, B., D. Veynante, and S. Candel (2015). Modeling combustion chem-

istry in large eddy simulation of turbulent flames. *Flow, Turbulence and Combustion 94*(1), 3–42. *(p. 7, 19, 87, 99)*

Fiorina, B., R. Vicquelin, P. Auzillon, N. Darabiha, O. Gicquel, and D. Veynante (2010, 3). A filtered tabulated chemistry model for LES of premixed combustion. *Combustion and Flame 157*(3), 465–475. *(p. 88)*

Franzelli, B., B. Fiorina, and N. Darabiha (2013). A tabulated chemistry method for spray combustion. *Proceedings of the Combustion Institute 34*(1), 1659–1666. *(p. 22)*

Franzelli, B., E. Riber, and B. Cuenot (2013). Impact of the chemical description on a large eddy simulation of a lean partially premixed swirled flame. *Comptes Rendus Mécanique 341*(1-2), 247–256. *(p. 6, 23)*

Franzelli, B., E. Riber, B. Cuenot, and M. Ihme (2015). Numerical modeling of soot production in aero-engine combustors using large eddy simulations. *ASME Turbo Expo 2015*. *(p. 7, 24, 37, 50, 92)*

Franzelli, B., E. Riber, L. Y. Gicquel, and T. Poinsot (2012). Large Eddy Simulation of combustion instabilities in a lean partially premixed swirled flame. *Combustion and Flame 159*(2), 621–637. *(p. 24, 38)*

Franzelli, B., E. Riber, M. Sanjosé, and T. Poinsot (2010). A two-step chemical scheme for kerosene-air premixed flames. *Combustion and Flame 157*(7), 1364 – 1373. *(p. 7, 23, 50, 92)*

Franzelli, B., A. Vié, and N. Darabiha (2019). A three-equation model for the prediction of soot emissions in les of gas turbines. *Proceedings of the Combustion Institute 37*(4), 5411 – 5419. *(p. 6, 7, 35, 36, 37, 39, 81, 92)*

Frenklach, M. (2002a). Method of moments with interpolative closure. *Chemical Engineering Science 57*(12), 2229–2239. *(p. 33)*

Frenklach, M. (2002b). Reaction mechanism of soot formation in flames. *Phys. Chem. Chem. Phys. 4*, 2028–2037. *(p. 14, 32, 33)*

Frenklach, M. and S. J. Harris (1987). Aerosol dynamics modeling using the method of moments. *Journal of Colloid and Interface Science 118*(1), 252–261. *(p. 7, 33, 38)*

Frenklach, M. and H. Wang (1991). Detailed modeling of soot particle nucleation and growth. *Symposium (International) on Combustion 23*(1), 1559 – 1566. Twenty-Third Symposium (International) on Combustion. *(p. 14)*

Frenklach, M. and H. Wang (New York, 1994). Detailed mechanism and modeling of soot particle formation. *H. Bockhorn (Ed.), Soot Formation in Combustion: Mechanisms and Models*. *(p. xiii, 12, 13, 14, 28, 92)*

Frenklach, M., H. Wang, M. Goldenberg, G. Smith, and D. Golden (1995). Gri-mech: An optimized detailed chemical reaction mechanism for methane combustion. topical report, september 1992-august 1995. Technical report, SRI International, Menlo Park, CA (United States). *(p. 38)*

Frenklach, M., H. Wang, C.-L. Yu, M. Goldenberg, C. Bowman, R. Hanson, D. Davidson, E. Chang, G. Smith, D. Golden, W. Gardiner, and

V. Lissianski (1995). Gri-mech 1.2. *(p. 38)*

Gallen, L. (2020). *Prediction of soot particles in Gas Turbine Combustors using Large Eddy Simulation*. Ph. D. thesis, Université de Toulouse. *(p. 20, 21, 30, 37)*

Gallen, L., A. Felden, E. Riber, and B. Cuenot (2019). Lagrangian tracking of soot particles in LES of gas turbines. *Proceedings of the Combustion Institute 37*(4), 5429 – 5436. *(p. 6, 7, 21, 30)*

Geigle, K. P., R. Hadef, and W. Meier (2013, 10). Soot formation and flame characterization of an aero-engine model combustor burning ethylene at elevated pressure. *Journal of Engineering for Gas Turbines and Power 136*(2), 021505–021505. *(p. xi, 37, 119)*

Gelbard, F. and J. H. Seinfeld (1980). Simulation of multicomponent aerosol dynamics. *Journal of Colloid and Interface Science 78*(2), 485–501. *(p. 30)*

Germano, M., U. Piomelli, P. Moin, and W. H. Cabot (1991). A dynamic subgrid-scale eddy viscosity model. *Physics of Fluids A: Fluid Dynamics 3*(7), 1760–1765. *(p. 86)*

Gicquel, O., N. Darabiha, and D. Thévenin (2000). Laminar premixed hydrogen / air counterflow flame simulations using flame prolongation of ILDM with differential diffusion. *Proceedings of the Combustion Institute 28*(2), 1901–1908. *(p. 21, 92)*

Goussis, D. A. (2012). Quasi steady state and partial equilibrium approximations: their relation and their validity. *Combustion Theory and Modelling 16*(5), 869–926. *(p. 20)*

Goussis, D. A. and U. Maas (2011). Model reduction for combustion chemistry. In *Turbulent Combustion Modeling*, pp. 193–220. Springer. *(p. 20)*

Grader, M., C. Eberle, P. Gerlinger, and M. Aigner (2018). LES of a pressurized, sooting aero-engine model combustor at different equivalence ratios with a sectional approach for pahs and soot. In *Turbo Expo: Power for Land, Sea, and Air*, Volume 51050, pp. V04AT04A012. American Society of Mechanical Engineers. *(p. 37, 92)*

Han, W., V. Raman, M. E. Mueller, and Z. Chen (2019). Effects of combustion models on soot formation and evolution in turbulent nonpremixed flames. *Proceedings of the Combustion Institute 37*(1), 985–992. *(p. 37, 92)*

Hawkes, E. R. and R. Cant (2000). A flame surface density approach to large-eddy simulation of premixed turbulent combustion. *Proceedings of the Combustion Institute 28*(1), 51–58. *(p. 89)*

Haworth, D. C. (2010). Progress in probability density function methods for turbulent reacting flows. *Progress in Energy and Combustion Science 36*(2), 168–259. *(p. 88)*

Haynes, B. and H. G. Wagner (1982). The surface growth phenomenon in soot formation. *Zeitschrift für Physikalische Chemie 133*(2), 201–213. *(p. 15)*

Herdman, J. D. and J. H. Miller (2008). Intermolecular potential calculations

for polynuclear aromatic hydrocarbon clusters. *The Journal of Physical Chemistry A 112*(28), 6249–6256. *(p. 14)*

Homann, K.-H. (1998). Fullerenes and soot formation-new pathways to large particles in flames. *Angewandte Chemie International Edition 37*(18), 2434–2451. *(p. 14)*

Hussein, H. J., S. P. Capp, W. K. George, et al. (1994). Velocity measurements in a high-reynolds-number, momentum-conserving, axisymmetric, turbulent jet. *Journal of Fluid Mechanics 258*(1), 31–75. *(p. 105)*

IEA (2020a). International Energy Agency, https://www.iea.org/data-and-statistics. *(p. xiii, 1, 2)*

IEA (2020b). World Energy Outlook 2020, IEA, Paris, https://www.iea.org/reports/world-energy-outlook-2020. *(p. xiii, 2, 3)*

Ihme, M. and H. Pitsch (2008). Modeling of radiation and nitric oxide formation in turbulent nonpremixed flames using a flamelet/progress variable formulation. *Physics of Fluids 20*(5), 055110. *(p. 6, 22, 37, 87, 92)*

ISF5 (2021). International Sooting Flame Workshop, http://www.adelaide.edu.au/cet/isfworkshop/data-sets/. *(p. xvii, 9, 37, 72, 76, 77, 101, 107, 110, 111)*

Jain, A. and Y. Xuan (2019). Effects of large aromatic precursors on soot formation in turbulent non-premixed sooting jet flames. *Combustion Theory and Modelling 23*(3), 439–466. *(p. 37, 40, 92, 107, 109, 110, 111)*

Jaouen, N., L. Vervisch, P. Domingo, and G. Ribert (2017). Automatic reduction and optimisation of chemistry for turbulent combustion modelling: Impact of the canonical problem. *Combustion and Flame 175*, 60–79. *(p. 20)*

Jaravel, T., E. Riber, B. Cuenot, and G. Bulat (2017). Large eddy simulation of an industrial gas turbine combustor using reduced chemistry with accurate pollutant prediction. *Proceedings of the Combustion Institute 36*(3), 3817–3825. *(p. 6, 20, 21)*

Jaravel, T., E. Riber, B. Cuenot, and P. Pepiot (2018). Prediction of flame structure and pollutant formation of sandia flame d using large eddy simulation with direct integration of chemical kinetics. *Combustion and Flame 188*, 180–198. *(p. 6)*

Jones, W. and R. Lindstedt (1988). Global reaction schemes for hydrocarbon combustion. *Combustion and Flame 73*(3), 233–249. *(p. 23)*

Kazakov, A. and M. Frenklach (1998). Dynamic modeling of soot particle coagulation and aggregation: Implementation with the method of moments and application to high-pressure laminar premixed flames. *Combustion and flame 114*(3-4), 484–501. *(p. xiv, 27, 28)*

Kearney, S. P., D. R. Guildenbecher, C. Winters, P. A. Farias, T. W. Grasser, and J. C. Hewson (2015, Sep). *Temperature, Oxygen, and Soot-Volume-Fraction Measurements in a Turbulent C2H4-Fueled Jet Flame. (p. xvii, 107, 108, 109)*

Kennedy, I. M. (1987). The evolution of a soot aerosol in a counterflow dif-

fusion flame. *Combustion and flame 68*(1), 1–16. *(p. 15)*

Kennedy, I. M., W. Kollmann, and J. Y. Chen (1990). A model for soot formation in a laminar diffusion flame. *Combustion and Flame 81*(1), 73–85. *(p. 34)*

Kerstein, A. R., W. T. Ashurst, and F. A. Williams (1988). Field equation for interface propagation in an unsteady homogeneous flow field. *Physical Review A 37*(7), 2728. *(p. 88)*

Kitamura, T., T. Ito, J. Senda, and H. Fujimoto (2002). Mechanism of smokeless diesel combustion with oxygenated fuels based on the dependence of the equivalence ration and temperature on soot particle formation. *International Journal of Engine Research 3*(4), 223–248. *(p. 5)*

Knikker, R., D. Veynante, and C. Meneveau (2002). A priori testing of a similarity model for large eddysimulations of turbulent premixed combustion. *Proceedings of the combustion institute 29*(2), 2105–2111. *(p. 89)*

Knikker, R., D. Veynante, and C. Meneveau (2004). A dynamic flame surface density model for large eddy simulation of turbulent premixed combustion. *Physics of Fluids 16*(11), L91–L94. *(p. 89)*

Kollmann, W., I. M. Kennedy, M. Metternich, and J.-Y. Chen (1994). Application of a soot model to a turbulent ethylene diffusion flame. In *Soot Formation in Combustion*, pp. 503–526. Springer. *(p. 7)*

Lam, S. and D. Goussis (1994). The CSP method for simplifying kinetics. *International Journal of Chemical Kinetics 26*(4), 461–486. *(p. 20)*

Lamouroux, J., M. Ihme, B. Fiorina, and O. Gicquel (2014). Tabulated chemistry approach for diluted combustion regimes with internal recirculation and heat losses. *Combustion and Flame 161*(8), 2120–2136. *(p. 23)*

Lancien, T., K. Prieur, D. Durox, S. Candel, and R. Vicquelin (2017). Large-eddy simulation of light-round in an annular combustor with liquid spray injection and comparison with experiments. (50848), V04AT04A069–. *(p. 24)*

Lecocq, G., D. Poitou, I. Hernandez, F. Duchaine, E. Riber, and B. Cuenot (2014). LES model for sooting turbulent nonpremixed flames. *Flow, Turb. and Combustion 92*, 947–970. *(p. 24, 38)*

Lefebvre, A. H. and D. R. Ballal (2010). *Gas turbine combustion: alternative fuels and emissions*. CRC press. *(p. xiii, 4, 5)*

Legier, J.-P., T. Poinsot, and D. Veynante (2000). Dynamically thickened flame LES model for premixed and non-premixed turbulent combustion. In *Proceedings of the Summer Program*, Volume 2000, pp. 157–168. Center for Turbulence Research Stanford, CA. *(p. 89, 96)*

Lepage, V. (2000). *Elaboration d'une méthode de réduction de schémas cinétiques détaillés. Application aux mécanismes de combustion du gaz naturel et du n-décane*. Ph. D. thesis, Université d'Orléans. *(p. 20)*

Leung, K. M., R. P. Lindstedt, and W. P. Jones (1991). A simplified reaction mechanism for soot formation in nonpremixed flames. *Combustion and Flame 87*(3), 289–305. *(p. 7, 34, 35, 62)*

Lindstedt, P. R. (1994). *Simplified Soot Nucleation and Surface Growth Steps for Non-Premixed Flames*, pp. 417–441. Berlin, Heidelberg: Springer Berlin Heidelberg. *(p. 34)*

Lindstedt, R. and S. Louloudi (2005). Joint-scalar transported pdf modeling of soot formation and oxidation. *Proceedings of the Combustion Institute 30*(1), 775 – 783. *(p. 34, 38)*

Liu, F., H. Guo, and G. J. Smallwood (2004). Effects of radiation model on the modeling of a laminar coflow methane/air diffusion flame. *Combustion and Flame 138*(1-2), 136–154. *(p. 78)*

Lopez-Parra, F. and A. Turan (2007, 06). Computational study on the effects of non-periodic flow perturbations on the emissions of soot and nox in a turbulent methane/air diffusion flame. *Combustion Science and Technology 179*(7), 1361–1384. *(p. 34)*

Løvås, T., F. Mauss, C. Hasse, and N. Peters (2002). Development of adaptive kinetics for application in combustion systems. *Proceedings of the Combustion Institute 29*(1), 1403–1410. *(p. 20)*

Lu, T. and C. K. Law (2005). A directed relation graph method for mechanism reduction. *Proceedings of the Combustion Institute 30*(1), 1333–1341. *(p. 20)*

Lu, T. and C. K. Law (2006). Systematic approach to obtain analytic solutions of quasi steady state species in reduced mechanisms. *The Journal of Physical Chemistry A 110*(49), 13202–13208. *(p. 20)*

Lu, T. and C. K. Law (2008). A criterion based on computational singular perturbation for the identification of quasi steady state species: A reduced mechanism for methane oxidation with NO chemistry. *Combustion and Flame 154*(4), 761–774. *(p. 7, 20)*

Lu, T. and C. K. Law (2009). Toward accommodating realistic fuel chemistry in large-scale computations. *Progress in Energy and Combustion Science 35*(2), 192–215. *(p. 17)*

Lu, T., C. K. Law, C. S. Yoo, and J. H. Chen (2009). Dynamic stiffness removal for direct numerical simulations. *Combustion and Flame 156*(8), 1542–1551. *(p. 18)*

Luu, T. (2024). *Kinetic schemes reduction using the virtual chemistry method: application to solid propulsion (Under preparation)*. Ph. D. thesis, Ecole CentraleSupélec, Université Paris-Saclay. *(p. 118)*

Maas, U. and S. B. Pope (1992a). Implementation of simplified chemical kinetics based on intrinsic low-dimensional manifolds. *Proceedings of the Combustion Institute 24*(1), 103–112. *(p. 7, 21)*

Maas, U. and S. B. Pope (1992b). Simplifying chemical kinetics: intrinsic low-dimensional manifolds in composition space. *Combustion and Flame 88*(3), 239–264. *(p. 21)*

Madadi-Kandjani, E. and A. Passalacqua (2015). An extended quadrature-based moment method with log-normal kernel density functions. *Chemical Engineering Science 131*(0), 323 – 339. *(p. 33)*

Magnussen, B. (1989). Modeling of pollutant formation in gas turbine combustors based on the eddy dissipation concept. In *18th International Congress on Combustion Engines, Tianjin, China, June*, pp. 5–9. *(p. 34)*

Magnussen, B. F. and B. H. Hjertager (1977). On mathematical modeling of turbulent combustion with special emphasis on soot formation and combustion. *Symposium (International) on Combustion 16*(1), 719–729. *(p. 87)*

Mahmood, W. M. F. W., A. LaRocca, P. J. Shayler, F. Bonatesta, and I. Pegg (2012, 04). Predicted paths of soot particles in the cylinders of a direct injection diesel engine. In *SAE Technical Paper*. SAE International. *(p. 30)*

Maio, G. (2020). *Pollutant prediction in numerical simulations of laminar and turbulent flames using virtual chemistry*. Ph. D. thesis, Ecole CentraleSupélec, Université Paris-Saclay. *(p. xiv, 8, 46, 47, 49, 50, 52, 53, 54, 58)*

Maio, G., M. Cailler, A. Cuoci, and B. Fiorina (2020). A virtual chemical mechanism for prediction of NO emissions from flames. *Combustion Theory and Modelling 0*(0), 1–31. *(p. xiv, 8, 46, 52, 55, 56, 60, 61, 64, 66, 76, 121)*

Maio, G., M. Cailler, N. Darabiha, and B. Fiorina (2020). Capturing multi-regime combustion in turbulent flames with a virtual chemistry approach. *Proceedings of the Combustion Institute*. *(p. 8, 88, 93)*

Maio, G., M. Cailler, R. Mercier, and B. Fiorina (2019). Virtual chemistry for temperature and CO prediction in LES of non-adiabatic turbulent flames. *Proceedings of the Combustion Institute 37*(2), 2591 – 2599. *(p. 6, 8, 24, 48, 52, 54, 60, 88, 93)*

Marchal, C. (2008, December). *Soot formation and oxidation modelling in an automotive engine*. Theses, Université d'Orléans. *(p. 27)*

Marchisio, D. L. and R. O. Fox (2005). Solution of population balance equations using the direct quadrature method of moments. *Journal of Aerosol Science 36*(1), 43 – 73. *(p. 33)*

Masiol, M. and R. M. Harrison (2014). Aircraft engine exhaust emissions and other airport-related contributions to ambient air pollution: A review. *Atmospheric Environment 95*, 409–455. *(p. xiii, 3, 4)*

Mauss, F., K. Netzell, and H. Lehtiniemi (2006). Aspects of modeling soot formation in turbulent diffusion flames. *Combustion Science and Technology 178*(10-11), 1871–1885. *(p. 28)*

Mauss, F., T. Schäfer, and H. Bockhorn (1994). Inception and growth of soot particles in dependence on the surrounding gas phase. *Combustion and Flame 99*(3–4), 697 – 705. 25th Symposium (International) on Combustion Papers. *(p. 28)*

McBride, B., S. Gordon, M. Reno, U. S. N. Aeronautics, and S. Administration (1993). *Coefficients for Calculating Thermodynamic and Transport Properties of Individual Species*. NASA technical memorandum. NASA

Langley Research Center. *(p. 47)*

Mehl, M., W. J. Pitz, C. K. Westbrook, and H. J. Curran (2011). Kinetic modeling of gasoline surrogate components and mixtures under engine conditions. *Proceedings of the Combustion Institute 33*(1), 193 – 200. *(p. 16)*

Menon, A. V., S.-Y. Lee, M. J. Linevsky, T. A. Litzinger, and R. J. Santoro (2007). Addition of no2 to a laminar premixed ethylene–air flame: effect on soot formation. *Proceedings of the Combustion Institute 31*(1), 593–601. *(p. xv, 72, 74)*

Menon, S. and W. H. Calhoon Jr (1996). Subgrid mixing and molecular transport modeling in a reacting shear layer. In *Symposium (International) on Combustion*, Volume 26, pp. 59–66. Elsevier. *(p. 87)*

Mercier, R. (2015). *Turbulent combustion modeling for Large Eddy Simulation of non-adiabatic stratified flames*. Ph. D. thesis, Ecole Centrale Paris. *(p. xvi, 84, 85)*

Metcalfe, W. K., S. M. Burke, S. S. Ahmed, and H. J. Curran (2013). A hierarchical and comparative kinetic modeling study of c1- c2 hydrocarbon and oxygenated fuels. *International Journal of Chemical Kinetics 45*(10), 638–675. *(p. 39)*

Miller, J. H. (1991). The kinetics of polynuclear aromatic hydrocarbon agglomeration in flames. In *Symposium (International) on Combustion*, Volume 23, pp. 91–98. Elsevier. *(p. 14)*

Mitchell, P. and M. Frenklach (1998). Monte carlo simulation of soot aggregation with simultaneous surface growth-why primary particles appear spherical. *Symposium (International) on Combustion 27*(1), 1507 – 1514. Twenty-Seventh Sysposium (International) on Combustion Volume One. *(p. 30)*

Modest, M. F. (2013). *Radiative Heat Transfer (Third Edition)*. Boston: Academic Press. *(p. 65, 96)*

Moin, P., K. Squires, W. Cabot, and S. Lee (1991). A dynamic subgrid-scale model for compressible turbulence and scalar transport. *Physics of Fluids A: Fluid Dynamics 3*(11), 2746–2757. *(p. 86, 103)*

Montgomery, C. J., C. Yang, A. R. Parkinson, and J.-Y. Chen (2006). Selecting the optimum quasi-steady-state species for reduced chemical kinetic mechanisms using a genetic algorithm. *Combustion and Flame 144*(1), 37–52. *(p. 20)*

Moss, J. B., C. D. Stewart, and K. J. Syed (1989). Flowfield modelling of soot formation at elevated pressure. *Symposium (International) on Combustion 22*(1), 413–423. *(p. 7, 34)*

Moureau, V., P. Domingo, and L. Vervisch (2011). Design of a massively parallel cfd code for complex geometries. *Comptes Rendus Mécanique 339*(2-3), 141–148. *(p. 9, 103)*

Mueller, M., G. Blanquart, and H. Pitsch (2009a). Hybrid method of moments for modeling soot formation and growth. *Combust. Flame 156*(6),

1143 – 1155. *(p. 38)*

Mueller, M. E., G. Blanquart, and H. Pitsch (2009b). A joint volume-surface model of soot aggregation with the method of moments. *Proc. Combust. Inst. 32*(1), 785 – 792. *(p. 7, 14, 33, 34, 36, 62)*

Mueller, M. E., G. Blanquart, and H. Pitsch (2009c). A joint volume-surface model of soot aggregation with the method of moments. *Proc. Combust. Inst. 32*(1), 785 – 792. *(p. 110)*

Mueller, M. E. and H. Pitsch (2011). Large eddy simulation subfilter modeling of soot-turbulence interactions. *Physics of Fluids (1994-present) 23*(11), –. *(p. 92)*

Mueller, M. E. and H. Pitsch (2012a, 6). LES model for sooting turbulent nonpremixed flames. *Combustion and Flame 159*(6), 2166–2180. *(p. 6, 37)*

Mueller, M. E. and H. Pitsch (2012b). LES model for sooting turbulent nonpremixed flames. *Combustion and Flame 159*(6), 2166 – 2180. *(p. 7, 92, 108, 110, 121)*

Narayanaswamy, K., G. Blanquart, and H. Pitsch (2010). A consistent chemical mechanism for oxidation of substituted aromatic species. *Combustion and Flame 157*(10), 1879–1898. *(p. 38, 39, 109)*

Netzell, K., H. Lehtiniemi, and F. Mauss (2007, 1). Calculating the soot particle size distribution function in turbulent diffusion flames using a sectional method. *Proceedings of the Combustion Institute 31*(1), 667–674. *(p. 30)*

Nguyen, T. T., F. Laurent, R. O. Fox, and M. Massot (2016). Solution of population balance equations in applications with fine particles: Mathematical modeling and numerical schemes. *Journal of Computational Physics 325*, 129–156. *(p. 33)*

Nguyen-Van, C. (2021). *Modeling and simulation of two-phase combustion in aircraft engines: development of virtual chemistry for aerothermal and pollutant emissions predictions (Under preparation)*. Ph. D. thesis, Ecole CentraleSupélec, Université Paris-Saclay. *(p. 55)*

Nicoud, F. and F. Ducros (1999). Subgrid-scale stress modelling based on the square of the velocity gradient tensor. *62*(3), 183–200. *(p. 86)*

Nicoud, F., H. B. Toda, O. Cabrit, S. Bose, and J. Lee (2011). Using singular values to build a subgrid-scale model for large eddy simulations. *Physics of Fluids 23*(8). *(p. 86, 103)*

Ong, J. C., K. M. Pang, J. H. Walther, J.-H. Ho, and H. K. Ng (2018). Evaluation of a lagrangian soot tracking method for the prediction of primary soot particle size under engine-like conditions. *Journal of Aerosol Science 115*, 70–95. *(p. 30)*

Pailthorpe, B. and W. Russel (1982). The retarded van der waals interaction between spheres. *Journal of Colloid and Interface Science 89*(2), 563 – 566. *(p. 27)*

Panchapakesan, N. R. and J. L. Lumley (1993). Turbulence measurements

in axisymmetric jets of air and helium. part 1. air jet. *Journal of Fluid Mechanics 246*, 197–223. *(p. 104, 105)*

Pang, B., M.-Z. Xie, M. Jia, and Y.-D. Liu (2013). Development of a phenomenological soot model coupled with a skeletal pah mechanism for practical engine simulation. *Energy & fuels 27*(3), 1699–1711. *(p. 38)*

Pecquery, F., V. Moureau, G. Lartigue, L. Vervisch, and A. Roux (2014). Modelling nitrogen oxide emissions in turbulent flames with air dilution: Application to les of a non-premixed jet-flame. *Combustion and flame 161*(2), 496–509. *(p. 6)*

Peeters, T. W. J., P. P. J. Stroomer, J. E. de Vries, D. J. E. M. Roekaerts, and C. J. Hoogendoorn (1994). Comparative experimental and numerical investigation of a piloted turbulent natural-gas diffusion flame. *Symposium (International) on Combustion 25*(1), 1241–1248. *(p. xi, 37)*

Pejpichestakul, W. (2019). *Chemical and Physical Pathways of PAH and Soot Formation in Laminar Flames*. Ph. D. thesis, Université Libre de Bruxelles and Politecnico di Milano. *(p. 32)*

Pejpichestakul, W., A. Cuoci, A. Frassoldati, M. Pelucchi, A. Parente, and T. Faravelli (2019). Buoyancy effect in sooting laminar premixed ethylene flame. *Combustion and Flame 205*, 135 – 146. *(p. 32, 33, 43, 66)*

Pejpichestakul, W., E. Ranzi, M. Pelucchi, A. Frassoldati, A. Cuoci, A. Parente, and T. Faravelli (2019). Examination of a soot model in premixed laminar flames at fuel-rich conditions. *Proceedings of the Combustion Institute 37*(1), 1013 – 1021. *(p. 7, 32, 33, 43, 66)*

Pepiot, P. (2008). *Automatic strategies to model transportation fuel surrogates*. Ph. D. thesis, Stanford University. *(p. 7, 20, 38, 62, 92)*

Pepiot, P. and H. Pitsch (2005). Systematic reduction of large chemical mechanisms. In *4th Joint Meeting of the US Sections of the Combustion Institute*, Volume 2123, pp. 2005. Drexel University Pittsburgh, PA, USA. *(p. 20)*

Pepiot-Desjardins, P. and H. Pitsch (2008). An efficient error-propagation-based reduction method for large chemical kinetic mechanisms. *Combustion and Flame 154*(1), 67–81. *(p. 20)*

Peters, N. (1984). Laminar diffusion flamelet models in non-premixed turbulent combustion. *Progress in Energy and Combustion Science 10*(3), 319–339. *(p. 7, 22)*

Pierce, C. D. and P. Moin (2004). Progress-variable approach for large-eddy simulation of non-premixed turbulent combustion. *Journal of Fluid Mechanics 504*, 73–97. *(p. 22)*

Pitsch, H. and L. D. De Lageneste (2002). Large-eddy simulation of premixed turbulent combustion using a level-set approach. *Proceedings of the Combustion Institute 29*(2), 2001–2008. *(p. 89)*

Poinsot, T. and D. Veynante (2012). *Theoretical and numerical combustion*. Third Edition by T. Poinsot. *(p. 22, 84, 86, 87, 89, 101)*

Poitou, D., M. El Hafi, and B. Cuenot (2008). Diagnosis of turbulence ra-

diation interaction in turbulent flames and implications for modeling in large eddy simulation. *Turkish Journal of Engineering and Environmental Sciences 31*(6), 371–381. *(p. 87, 103)*

Polifke, W., W. Geng, and K. Döbeling (1998). Optimization of rate coefficients for simplified reaction mechanisms with genetic algorithms. *Combustion and Flame 113*(1-2), 119 – 134. *(p. 23)*

Pope, C. J. and J. B. Howard (1997). Simultaneous particle and molecule modeling (spamm): An approach for combining sectional aerosol equations and elementary gas-phase reactions. *Aerosol Science and Technology 27*(1), 73–94. *(p. 7, 31)*

Pope, S. B. (1985). Pdf methods for turbulent reactive flows. *Progress in energy and combustion science 11*(2), 119–192. *(p. 88)*

Pope, S. B. (1997). Computationally efficient implementation of combustion chemistry using in situ adaptive tabulation. *(p. 39)*

Pope, S. B. (2000). *Turbulent Flows* (1 ed.). Cambridge University Press. *(p. 84, 103, 104, 105)*

Raman, V. and R. O. Fox (2016). Modeling of fine-particle formation in turbulent flames. *Annual Review of Fluid Mechanics 48*, 159–190. *(p. 29)*

Ramkrishna, D. and M. R. Singh (2014). Population balance modeling: current status and future prospects. *Annual review of chemical and biomolecular engineering 5*, 123–146. *(p. 25)*

Richter, H., T. G. Benish, O. A. Mazyar, W. H. Green, and J. B. Howard (2000). Formation of polycyclic aromatic hydrocarbons and their radicals in a nearly sooting premixed benzene flame. *Proceedings of the Combustion Institute 28*(2), 2609–2618. *(p. 14)*

Richter, H., S. Granata, W. H. Green, and J. B. Howard (2005). Detailed modeling of PAH and soot formation in a laminar premixed benzene/oxygen/argon low-pressure flame. *Proceedings of the Combustion Institute 30*(1), 1397 – 1405. *(p. 32)*

Richter, H. and J. Howard (2000). Formation of polycyclic aromatic hydrocarbons and their growth to soot—a review of chemical reaction pathways. *Progress in Energy and Combustion Science 26*(4–6), 565 – 608. *(p. 17)*

Rodrigues, P. (2018). *Modélisation multiphysique de flammes turbulentes suitées avec la prise en compte des transferts radiatifs et des transferts de chaleur pariétaux*. Ph. D. thesis, Ecole CentraleSupélec, Université Paris-Saclay. *(p. xiii, 22, 37, 103, 105)*

Rodrigues, P., B. Franzelli, R. Vicquelin, O. Gicquel, and N. Darabiha (2018). Coupling an LES approach and a soot sectional model for the study of sooting turbulent non-premixed flames. *Combustion and Flame 190*, 477 – 499. *(p. 6, 7, 30, 31, 35, 36, 37, 62, 92, 102, 109)*

Rodrigues, P., O. Gicquel, B. Franzelli, N. Darabiha, and R. Vicquelin (2019). Analysis of radiative transfer in a turbulent sooting jet flame using a monte carlo method coupled to large eddy simulation. *Journal of Quan-*

titative Spectroscopy and Radiative Transfer 235, 187–203. *(p. 107, 108, 109, 110, 111)*

Saggese, C., A. Cuoci, A. Frassoldati, S. Ferrario, J. Camacho, H. Wang, and T. Faravelli (2016). Probe effects in soot sampling from a burner-stabilized stagnation flame. *Combustion and Flame 167*, 184–197. *(p. 17)*

Saggese, C., S. Ferrario, J. Camacho, A. Cuoci, A. Frassoldati, E. Ranzi, H. Wang, and T. Faravelli (2015, 9). Kinetic modeling of particle size distribution of soot in a premixed burner-stabilized stagnation ethylene flame. *Combustion and Flame 162*(9), 3356–3369. *(p. xiii, 7, 17, 18, 31, 32, 33, 43, 62, 66, 67, 98, 121)*

Saggese, C., A. Frassoldati, A. Cuoci, T. Faravelli, and E. Ranzi (2013). A wide range kinetic modeling study of pyrolysis and oxidation of benzene. *Combustion and flame 160*(7), 1168–1190. *(p. 17)*

Saggese, C., N. E. Sánchez, A. Frassoldati, A. Cuoci, T. Faravelli, M. U. Alzueta, and E. Ranzi (2014). Kinetic modeling study of polycyclic aromatic hydrocarbons and soot formation in acetylene pyrolysis. *Energy & fuels 28*(2), 1489–1501. *(p. 17)*

Said, R., A. Garo, and R. Borghi (1997). Soot formation modeling for turbulent flames. *Combustion and Flame 108*(1), 71–86. *(p. 7, 34)*

Salenbauch, S., A. Cuoci, A. Frassoldati, C. Saggese, T. Faravelli, and C. Hasse (2015). Modeling soot formation in premixed flames using an extended conditional quadrature method of moments. *Combust. Flame* (0), –. *(p. 33)*

Salenbauch, S., C. Hasse, M. Vanni, and D. L. Marchisio (2019). A numerically robust method of moments with number density function reconstruction and its application to soot formation, growth and oxidation. *Journal of Aerosol Science 128*, 34 – 49. *(p. 7, 33, 34)*

Santoro, R., T. Yeh, J. Horvath, and H. Semerjian (1987). The transport and growth of soot particles in laminar diffusion flames. *Combustion Science and Technology 53*(2-3), 89–115. *(p. 77)*

Santoro, R. J., H. G. Semerjian, and R. A. Dobbins (1983). Soot particle measurements in diffusion flames. *Combustion and Flame 51*, 203–218. *(p. 9, 60, 76)*

Schuetz, C. A. and M. Frenklach (2002). Nucleation of soot: Molecular dynamics simulations of pyrene dimerization. *Proceedings of the Combustion Institute 29*(2), 2307 – 2314. *(p. 14, 62)*

Selvaraj, P., P. G. Arias, B. J. Lee, H. G. Im, Y. Wang, Y. Gao, S. Park, S. M. Sarathy, T. Lu, and S. H. Chung (2016). A computational study of ethylene–air sooting flames: Effects of large polycyclic aromatic hydrocarbons. *Combustion and Flame 163*, 427–436. *(p. 33, 40, 62, 92)*

Sewerin, F. and S. Rigopoulos (2018). An les-pbe-pdf approach for predicting the soot particle size distribution in turbulent flames. *Combustion and Flame 189*, 62–76. *(p. 37, 110)*

Siegla, D., G. Smith, K. G. Neoh, J. B. Howard, and A. F. Sarofim (1981).

Soot Oxidation in Flames, pp. 261–282. Springer US. *(p. 28)*

Sikalo, N., O. Hasemann, C. Schulz, A. Kempf, and I. Wlokas (2014). A genetic algorithm-based method for the automatic reduction of reaction mechanisms. *International Journal of Chemical Kinetics 46*(1), 41–59. *(p. 20)*

Sirignano, M., J. Kent, and A. D'Anna (2010). Detailed modeling of size distribution functions and hydrogen content in combustion-formed particles. *Combustion and Flame 157*(6), 1211 – 1219. *(p. 32)*

Sirignano, M., J. Kent, and A. D'Anna (2013). Modeling formation and oxidation of soot in nonpremixed flames. *Energy & Fuels 27*(4), 2303–2315. *(p. 32, 33)*

Slavinskaya, N. and P. Frank (2009). A modelling study of aromatic soot precursors formation in laminar methane and ethene flames. *Combustion and Flame 156*(9), 1705 – 1722. *(p. 18, 39)*

Slavinskaya, N. A., U. Riedel, S. B. Dworkin, and M. J. Thomson (2012). Detailed numerical modeling of {PAH} formation and growth in non-premixed ethylene and ethane flames. *Combustion and Flame 159*(3), 979 – 995. *(p. 39)*

Smoluchowski, M. (1916). *Versuch einer mathematischen Theorie der Koagulationskinetik kolloider Lösungen. (p. 26)*

Smooke, M. D., C. S. McEnally, L. D. Pfefferle, R. J. Hall, and M. B. Colket (1999). Computational and experimental study of soot formation in a coflow, laminar diffusion flame. *Combustion and Flame 117*(1), 117–139. *(p. 7, 30)*

Soufiani, A. and J. Taine (1987). Application of statistical narrow-band model to coupled radiation and convection at high temperature. *International journal of heat and mass transfer 30*(3), 437–447. *(p. 66, 67)*

Stanmore, B. R., J.-F. Brilhac, and P. Gilot (2001). The oxidation of soot: a review of experiments, mechanisms and models. *Carbon 39*(15), 2247–2268. *(p. 16)*

Stella, E. (2024). *Numerical modeling and simulations of turbulent non-premixed combustion in industrial burners (Under preparation)*. Ph. D. thesis, Ecole CentraleSupélec, Université Paris-Saclay. *(p. 118)*

Sung, Y., V. Raman, H. Koo, M. Mehta, and R. O. Fox (2014). Large-eddy simulation modeling of turbulent flame synthesis of titania nanoparticles using a bivariate particle description. *AIChE Journal 60*(2), 459–472. *(p. 39)*

Tesner, P. A., T. D. Smegiriova, and V. G. Knorre (1971). Kinetics of dispersed carbon formation. *Combustion and Flame 17*(2), 253–260. *(p. 7, 34)*

Tomlin, A. S., M. J. Pilling, T. Turányi, J. H. Merkin, and J. Brindley (1992). Mechanism reduction for the oscillatory oxidation of hydrogen: sensitivity and quasi-steady-state analyses. *Combustion and Flame 91*(2), 107–130. *(p. 20)*

Turányi, T. (1990). Reduction of large reaction mechanisms. *New Journal of Chemistry 14*(11), 795–803. *(p. 19)*

Turányi, T. and T. Bérces (1990). Kinetics of reactions occurring in the unpolluted troposphere, II. sensitivity analysis. *Reaction Kinetics and Catalysis Letters 41*(1), 103–108. *(p. 20)*

Van Oijen, J., F. Lammers, and L. De Goey (2001). Modeling of complex premixed burner systems by using flamelet-generated manifolds. *Combustion and Flame 127*(3), 2124–2134. *(p. 21)*

Vander Wal, R. L., A. Yezerets, N. W. Currier, D. H. Kim, and C. M. Wang (2007). Hrtem study of diesel soot collected from diesel particulate filters. *Carbon 45*(1), 70 – 77. *(p. 12)*

Veynante, D. and V. Moureau (2015). Analysis of dynamic models for large eddy simulations of turbulent premixed combustion. *Combustion and Flame 162*(12), 4622–4642. *(p. 89)*

Violi, A., A. Kubota, T. Truong, W. Pitz, C. Westbrook, and A. Sarofim (2002). A fully integrated kinetic monte carlo/molecular dynamics approach for the simulation of soot precursor growth. *Proceedings of the Combustion Institute 29*(2), 2343–2349. *(p. 14)*

Violi, A., A. F. Sarofim, and G. A. Voth (2004). Kinetic monte carlo–molecular dynamics approach to model soot inception. *Combustion science and technology 176*(5-6), 991–1005. *(p. 14)*

Vlachos, D. (1996). Reduction of detailed kinetic mechanisms for ignition and extinction of premixed hydrogen/air flames. *Chemical Engineering Science 51*(16), 3979–3993. *(p. 20)*

Volpiani, P. S., T. Schmitt, and D. Veynante (2017). Large eddy simulation of a turbulent swirling premixed flame coupling the TFLES model with a dynamic wrinkling formulation. *Combustion and Flame 180*, 124–135. *(p. 24)*

Waldmann, L. and K. Schmitt (1966). Thermophoresis and diffusiophoresis of aerosols. *Aerosol science 137*. *(p. 25, 26)*

Wang, G., M. Boileau, and D. Veynante (2011). Implementation of a dynamic thickened flame model for large eddy simulations of turbulent premixed combustion. *Combustion and Flame 158*(11), 2199–2213. *(p. 89, 103)*

Wang, H. (2011). Formation of nascent soot and other condensed-phase materials in flames. *Proceedings of the Combustion Institute 33*(1), 41 – 67. *(p. 14, 16, 17)*

Wang, H., D. X. Du, C. J. Sung, and C. K. Law (1996). Experiments and numerical simulation on soot formation in opposed-jet ethylene diffusion flames. *Symposium (International) on Combustion 26*(2), 2359–2368. *(p. 28)*

Wang, Y. and S. H. Chung (2019). Soot formation in laminar counterflow flames. *Progress in Energy and Combustion Science 74*, 152 – 238. *(p. xiii, 12, 13, 15, 17, 18)*

Wang, Y., A. Raj, and S. H. Chung (2013). A pah growth mechanism and

synergistic effect on pah formation in counterflow diffusion flames. *Combust. Flame 160*(9), 1667 – 1676. *(p. 38, 109)*

Wang, Y., A. Raj, and S. H. Chung (2015). Soot modeling of counterflow diffusion flames of ethylene-based binary mixture fuels. *Combustion and Flame 162*(3), 586 – 596. *(p. 17)*

Weller, H., G. Tabor, A. Gosman, and C. Fureby (1998). Application of a flame-wrinkling les combustion model to a turbulent mixing layer. In *Symposium (International) on Combustion*, Volume 27, pp. 899–907. Elsevier. *(p. 89)*

Westbrook, C. K. and F. L. Dryer (1981). Simplified reaction mechanisms for the oxidation of hydrocarbon fuels in flames. *Combustion Science and Technology 27*(1-2), 31–43. *(p. 7, 23)*

Wick, A., F. Priesack, and H. Pitsch (2017). Large-eddy simulation and detailed modeling of soot evolution in a model aero engine combustor. (50848), V04AT04A020–. *(p. 37)*

Xu, F., A. M. El-Leathy, C. H. Kim, and G. M. Faeth (2003, 1). Soot surface oxidation in hydrocarbon/air diffusion flames at atmospheric pressure. *Combust. Flame 132*(1–2), 43–57. *(p. 28)*

Xu, F., P. B. Sunderland, and G. M. Faeth (1997, 3). Soot formation in laminar premixed ethylene/air flames at atmospheric pressure. *Combust. Flame 108*(4), 471–493. *(p. xv, 72, 74)*

Xuan, Y. and G. Blanquart (2015). Effects of aromatic chemistry-turbulence interactions on soot formation in a turbulent non-premixed flame. *Proc. Combust. Inst. 35*(2), 1911–1919. *(p. 37, 92)*

Yan, F., L. Xu, Y. Wang, S. Park, S. M. Sarathy, and S. H. Chung (2019). On the opposing effects of methanol and ethanol addition on pah and soot formation in ethylene counterflow diffusion flames. *Combustion and Flame 202*, 228 – 242. *(p. 30)*

Yang, S., J. K. Lew, and M. E. Mueller (2019). Large eddy simulation of soot evolution in turbulent reacting flows: Presumed subfilter PDF model for soot-turbulence-chemistry interactions. *Combustion and Flame 209*, 200 – 213. *(p. 37, 92, 115, 119)*

Yapp, E. K., D. Chen, J. Akroyd, S. Mosbach, M. Kraft, J. Camacho, and H. Wang (2015). Numerical simulation and parametric sensitivity study of particle size distributions in a burner-stabilised stagnation flame. *Combustion and Flame* (0), –. *(p. 26)*

Yuan, C. and R. O. Fox (2011). Conditional quadrature method of moments for kinetic equations. *Journal of Computational Physics 230*(22), 8216–8246. *(p. 39)*

Yuan, C., F. Laurent, and R. Fox (2012). An extended quadrature method of moments for population balance equations. *Journal of Aerosol Science 51*(0), 1 – 23. *(p. 33)*

Zhang, J., C. R. Shaddix, and R. W. Schefer (2011, Jul). Design of "model-friendly" turbulent non-premixed jet burners for c2+ hydrocarbon fuels.

Rev Sci Instrum 82(7), 074101. *(p. xi, xvii, 9, 37, 87, 101, 106, 107)*

Zhang, Q., H. Guo, F. Liu, G. Smallwood, and M. Thomson (2009). Modeling of soot aggregate formation and size distribution in a laminar ethylene/air coflow diffusion flame with detailed pah chemistry and an advanced sectional aerosol dynamics model. *Proceedings of the Combustion Institute 32*(1), 761–768. *(p. 78)*

Zhang, Q., M. Thomson, H. Guo, F. Liu, and G. Smallwood (2009). A numerical study of soot aggregate formation in a laminar coflow diffusion flame. *Combustion and Flame 156*(3), 697 – 705. *(p. 30)*

Zhubrin, S. V. (2009). Discrete reaction model for composition of sooting flames. *International Journal of Heat and Mass Transfer 52*(17), 4125–4133. *(p. 34)*

Zuber, M. A., W. M. F. W. Mahmood, Z. Harun, Z. Z. Abidin, A. L. Rocca, P. Shayler, and F. Bonatesta (2015, 04). Modeling of in-cylinder soot particle size evolution and distribution in a direct injection diesel engine. In *SAE Technical Paper*. SAE International. *(p. 30)*

université PARIS-SACLAY

ÉCOLE DOCTORALE
Sciences mécaniques et énergétiques, matériaux et géosciences (SMEMAG)

Titre: Modélisation de la formation de suies dans des flammes turbulentes par une approche de chimie virtuelle

Mots clés: Modélisation de la cinétique, Suies, Transferts radiatifs, Flammes laminaires et turbulentes

Résumé: La modélisation de la formation de particules de suies est une tâche très difficile en raison des interactions multiples de plusieurs phénomènes physiques complexes. Les simulations numériques des flammes turbulentes produisant des suies impliquent le développement de modèles de suies élaborés souvent trop exigeants en termes de calcul. D'autre part, les modèles simplifiés de suies sont limités à une petite gamme de conditions de fonctionnement d'intérêt. Une approche globale optimisée et innovante, appelée chimie virtuelle, est proposée ici. Elle consiste en un formalisme mathématique comprenant des espèces virtuelles et des réactions virtuelles, dont les paramètres thermochimiques sont optimisés par un algorithme génétique, en utilisant une base de données d'apprentissage constituée d'éléments de flammes de référence. Elle permet alors de reproduire la structure des flammes hydrocarbures-air, ainsi que la prédiction d'espèces polluantes spécifiques définies par l'utilisateur, ici la fraction volumique de suies, pour de multiples régimes de combustion et conditions de fonctionnement. La chimie réduite finale consiste en 12 espèces virtuelles et 6 réactions virtuelles, ce qui réduit considérablement le temps de calcul par rapport aux modèles chimiques détaillés. Comme les pertes de chaleur radiative sont importantes dans les flammes de suies, un nouveau modèle virtuel radiatif est également développé pour en tenir compte. Des simulations de flammes éthylène-air laminaires 1-D et 2-D sont réalisées pour évaluer les modèles virtuels de suies et radiatifs. La température, la fraction volumique de suies et les pertes thermiques radiatives sont en bon accord avec les données de référence. Ensuite, les modèles virtuels développés sont mis à l'épreuve dans les simulations à grands échelles d'air (LES) de flammes turbulentes. Les temps caractéristiques liés à la combustion turbulente étant très courts comparés ceux de la formation des particules de suies, un nouveau modèle à l'échelle de la sous-maille est proposé ici pour gérer les termes filtrés de la source de suies dans un cadre de chimie virtuelle. Les nouveaux modèles de chimie virtuelle, radiatif et de sous-maille sont mis à l'épreuve dans une flamme turbulente 3-D éthylène-air non prémélangée. Les résultats sont validés avec des données expérimentales et des calculs de chimie détaillée.

université PARIS-SACLAY

ÉCOLE DOCTORALE
Sciences mécaniques et énergétiques, matériaux et géosciences (SMEMAG)

Title: Modeling soot formation in turbulent flames using a virtual chemistry approach

Keywords: Kinetic Modeling, Soot, Radiative heat transfer, Laminar and Turbulent Flames

Abstract: Modeling soot particles formation is a very difficult task because of interactions of several complex physical phenomena. Numerical simulation of turbulent sooting flames implies development of elaborate soot models often too computationally demanding. Also, simplified soot models are limited to a small range of operating conditions of interest. Here, an innovative optimized global approach called virtual chemistry is proposed. It consists of a mathematical formalism including virtual species and virtual reactions, whose thermochemical parameters are optimized by a genetic algorithm using a learning database made of reference flame elements. This makes possible to reproduce the structure of hydrocarbon-air flames, as well as predicting specific user-defined pollutants, here soot volume fraction, for multiple combustion regimes and operating conditions. The final reduced chemistry consists of 12 virtual species and 6 virtual reactions, which considerably decreases the computational time compared to detailed chemistry models. As the radiative heat losses are important in sooting flames, a new radiative virtual model is also developed to account for them. Simulations of 1-D and 2-D laminar ethylene-air sooting flames are performed to evaluate the virtual soot and radiative models. Temperature, soot volume fraction and radiative heat losses are well predicted and are in good agreement with the reference data. Then, the developed virtual models are challenged in Large Eddy Simulations (LES) of turbulent sooting flames. As the turbulent combustion characteristic times are very small compared to those of soot particles production, a new subgrid-scale model is proposed here to manage the filtered soot source terms in a virtual chemistry framework. The new virtual chemistry, radiative and subgrid-scale models are challenged in a 3-D sooting turbulent non-premixed ethylene-air flame. Results are validated with experimental data and detailed chemistry computations.

Maison du doctorat de l'Université Paris-Saclay
2ème étage aile ouest, Ecole normale supérieure Paris-Saclay
4 avenue des Sciences,
91190 Gif-sur-Yvette, France